# Vertical Semiconductor Nanowires: Engineering Light at Nanoscale

by

Navneet Dhindsa

A thesis
presented to the University of Waterloo
in fulfillment of the
thesis requirement for the degree of
Doctor of Philosophy
in
Electrical and Computer Engineering(Nanotechnology)

Waterloo, Ontario, Canada, 2016

© Navneet Dhindsa 2016

I hereby declare that I am the sole author of this thesis. This is a true copy of the thesis, including any required final revisions, as accepted by my examiners.

I understand that my thesis may be made electronically available to the public.

## Abstract

Vertical semiconductor nanowires have gained considerable attention in the last decade for their attractive optical and electronic properties. Their high surface to volume ratio and their ability to confine charge carriers and photons in one dimension has enabled them to be a promising candidate for improved as well as novel devices in nanophotonics and optoelectronics. However, it is necessary to achieve high quality nanowires with controllable features to fully understand and fine-tune the optical properties of the nanowires to achieve desired applications.

In this study, various semiconductor materials like Gallium Arsenide (GaAs), Silicon and Amorphous Silicon (a-Si) were chosen to analyze and compare their optical properties using reflection measurements and finite difference time domain (FDTD) simulations. The nature of modal excitations in nanowires with the change in their diameter, pitch, shape and length are understood through simulation studies and verified using the measurements. Optical waveguiding, near field coupling, Fabry-Perot modes are comprehensively understood for the first time in the nanowire arrays.

The ordered nanowires arrays are fabricated using Inductively Coupled Plasma Reactive Ion Etching (ICP-RIE) and a good understanding of the etching chemistries of chosen materials is achieved to fabricate high aspect ratio (length to diameter ratio) nanowire arrays. For GaAs nanowires, the aspect ratio of up to 73 is achieved with the controlled diameters for the very first time. For a variety of hard masks, etching parameters have been developed to get a good control over the sidewalls, diameters, and shapes of the nanowires. The silicon nanowires etching parameters are modified to achieve different shapes in lateral and longitudinal directions. Lastly, Gallium Nitride (GaN) nanowires are fabricated using chlorine chemistry with nitrogen as a clean passivation gas and wide varieties of masks and their combinations have been tested to achieve vertical morphology.

Based on the understandings we achieved for the nanowires, a new platform is introduced for a-Si nanowires by etching them on a glass substrate and by integrating thin film with them to achieve the solar weighed absorptance 200-250 % higher than the thin film of the same thickness. Designs for broadband absorption in Gallium Arsenide nanowires are also considered and highest absorption achieved in those nanowires giving solar weighed absorption efficiency as high as 94%.

This thesis spans both design of nanowire arrays for various applications, and fabrication and experimental verifications of them. As the comprehensive studies were done on the optical properties of the nanowire, the thesis presents a complete picture of various optical modes and phenomena, which emanate in them due to their interaction with light. It will provide optoelectronics engineers design directions as nanowire devices are considered in the future of commercial applications.

## Acknowledgements

First of all, I would like to thank my supervisor, Prof. Simarjeet Saini for his continuous support throughout my Ph.D. studies. It is because of his knowledge, guidance, and patience that I am able to finish this thesis.

From Saini group, I would like to thank Jaspreet Walia for all those valuable discussions and insights for four years. I would also like to thank Mohammadreza Khorasaninejad for helping me to get familiar with the cleanroom processes and giving away his fabrication secrets on which I built my own fabrication techniques.

I would also like to extend my gratitude to our collaborator Dr. Ray LaPierre for his useful feedbacks, ideas, and the fabrication and characterization facilities he provided.

Lastly, I would like to thank the cleanroom staff at Mike and Ophelia Lazaridis Quantum Nano-Centre for their training and guidance throughout my Ph.D. work. I would like to thank Nathan Nelson-Fitzpatrick, Brian Goddard and Rodello Salandanan for training me on e-beam writing, etching processes, e-beam evaporation systems, thin-film growth and measurements, and for all the useful discussions and tips. I would also like to thank Vito Logiudice for being so kind through his guidance and support in the cleanroom.

# Table of Contents

**List of Tables** xi

**List of Figures** xii

**1 Introduction** 1

1.1 Vertical Nanowires Ensembles as Optical Waveguides . . . 3

1.2 Absorption in Nanowires . . . 4

1.3 Nanowires for Optoelectronics . . . 5

1.3.1 Photovoltaics . . . 6

1.3.2 Other Optoelectronics Applications . . . 8

1.3.3 Sensing . . . 8

1.4 Motivation and Thesis Outline . . . 9

**2 Theoretical Concepts** 13

2.1 Introduction . . . 13

2.2 Cylindrical Waveguide Modes . . . 14

2.3 Bloch Mode Coupling with Radial Modes in
Periodic Arrays . . . . . . . . . . 17
2.4 Fabry-Perot Microcavity Modes . . . . . . . . . . 20
2.5 Conclusion . . . . . . . . . . 23

**3 Simulation Studies of Semiconductor Nanowires 24**
3.1 Introduction . . . . . . . . . . 24
3.2 Resonant Optical Modes in Nanowires . . . . . . . . . . 25
3.2.1 Gallium Arsenide . . . . . . . . . . 26
3.2.2 Amorphous Silicon . . . . . . . . . . 29
3.2.3 Silicon . . . . . . . . . . 32
3.2.4 Comparison of Resonant Peaks for Different Materials . . . . . . . . 33
3.3 Near Field Coupling between the Nanowires . . . . . . . . . . 35
3.3.1 Effect of k on Waveguide Coupling . . . . . . . . . . 35
3.4 Longitudinal Modes in Nanowires . . . . . . . . . . 39
3.5 Length Analysis of Nanowires . . . . . . . . . . 40
3.6 Shape Effect in Nanowires . . . . . . . . . . 43
3.7 Conclusion . . . . . . . . . . 47

**4 Nanowires Fabrication 49**
4.1 Bottom-Up Approach . . . . . . . . . . 50
4.1.1 Silicon Nanowires . . . . . . . . . . 50
4.1.2 Gallium Arsenide Nanowires . . . . . . . . . . 52

4.1.3 Gallium Nitride Nanowires . . . . . . . . . . . . . . . . . . . . . . . 52
4.2 Drawbacks of Bottoms-up Approach . . . . . . . . . . . . . . . . . . . . . 53
4.3 Top-Down Approach . . . . . . . . . . . . . . . . . . . . . . . . . . . . . 54
4.3.1 Catalytic Chemical Etching . . . . . . . . . . . . . . . . . . . . . . . 54
4.3.2 Reactive Ion Etching . . . . . . . . . . . . . . . . . . . . . . . . . . 54
4.3.3 Crystalline Silicon Nanowires . . . . . . . . . . . . . . . . . . . . . 56
4.3.4 Amorphous Silicon Nanowires . . . . . . . . . . . . . . . . . . . . . 62
4.3.5 Gallium Arsenide Nanowires . . . . . . . . . . . . . . . . . . . . . . 64
4.3.6 Gallium Nitride Nanowires . . . . . . . . . . . . . . . . . . . . . . . 71
4.3.7 Diameter Distribution of Nanowires . . . . . . . . . . . . . . . . . . 75
4.4 Conclusion . . . . . . . . . . . . . . . . . . . . . . . . . . . . . . . . . . 76

**5 Optical Measurements and Experimental Studies** **77**

5.1 Introduction . . . . . . . . . . . . . . . . . . . . . . . . . . . . . . . . . 77
5.1.1 Reflection and Transmission Measurements setups . . . . . . . . . . 78
5.1.2 Analysis of a Reflection Spectrum . . . . . . . . . . . . . . . . . . . 79
5.1.3 Structural Colors . . . . . . . . . . . . . . . . . . . . . . . . . . . . 81
5.2 Modal Excitations in Nanowires . . . . . . . . . . . . . . . . . . . . . . . 82
5.2.1 Gallium Arsenide Nanowires . . . . . . . . . . . . . . . . . . . . . . 82
5.2.2 Amorphous Silicon Nanowires . . . . . . . . . . . . . . . . . . . . . 88
5.2.3 Structural Colors . . . . . . . . . . . . . . . . . . . . . . . . . . . . 93
5.3 Near Field Coupling: Comparison of Silicon, aSi and GaAs Nanowires . . . 97

5.4 Silicon Nanowires - The Comparison Between Ordered and Disordered Nanowires 100

5.4.1 Reflection for Ordered vs Disordered Nanowires . . . . . . . . . . . 102

5.5 Length Analysis of Nanowires . . . . . . . . . . . . . . . . . . . . . . . . 105

5.6 Tapering of the Nanowires . . . . . . . . . . . . . . . . . . . . . . . . . 107

5.7 Effect of Mask on Absorption of the Nanowires . . . . . . . . . . . . . . . . 110

5.7.1 Measured Reflectance . . . . . . . . . . . . . . . . . . . . . . . . 111

5.7.2 Simulated Reflectance and Absorptance . . . . . . . . . . . . . . . . 112

5.7.3 Simulations after Removing Substrate . . . . . . . . . . . . . . . . 115

5.7.4 Effect of Length . . . . . . . . . . . . . . . . . . . . . . . . . . . 117

5.7.5 Mask Thickness . . . . . . . . . . . . . . . . . . . . . . . . . . . 118

5.8 Design Rules for Nanowires . . . . . . . . . . . . . . . . . . . . . . . . 119

5.9 Conclusion . . . . . . . . . . . . . . . . . . . . . . . . . . . . . . . . . 120

**6 Absorption Optimization for Applications** **122**

6.1 Substrate Free GaAs Nanowires for Photodetectors . . . . . . . . . . . . . 123

6.1.1 MBE growth of GaAS/InGaP wafer . . . . . . . . . . . . . . . . . . 124

6.1.2 Nanowires and Device Fabrication . . . . . . . . . . . . . . . . . . . 124

6.1.3 Wet Etching of GaAs Substrate . . . . . . . . . . . . . . . . . . . . 125

6.1.4 Absorption Calculations . . . . . . . . . . . . . . . . . . . . . . . . 126

6.2 Nanowires Integration with Thin Films for Enhanced Absorption and Colorful Solar Cells . . . . . . . . . . . . . . . . . . . . . . . . . . . . . . . 129

6.2.1 Sample A - Nanowires on Glass Substrate . . . . . . . . . . . . . . . 130

6.2.2 Sample B - 500 nm Long Nanowires with 35 nm Thick Thin Film . 131
6.2.3 Sample C - 400 nm Long Nanowires with 135 nm Thick Thin Film 134
6.2.4 Structural Colors . . . . . . . . . . . . . . . . . . . . . . . . . . 136
6.2.5 Solar Weighed Absorptance . . . . . . . . . . . . . . . . . . . . . 137
6.3 Conclusion . . . . . . . . . . . . . . . . . . . . . . . . . . . . . . . . . 142

**7 Summary and Future Work 143**

7.1 Summary . . . . . . . . . . . . . . . . . . . . . . . . . . . . . . . . . 143

**References 146**

**Appendices 160**

**A 161**

# List of Tables

3.1 The resonance wavelengths and their corresponding refractive indices for GaAS, a-Si and Silicon nanowires indicating whether the nanowires are coupling depending on the value of their k. . . . . . . . . . . . . . . . . . . . . 39

4.1 Pseudo Bosch etching parameters for Silicon Nanowires . . . . . . . . . . . 57

4.2 Etching parameters to achieve tapered profiles for Silicon Nanowires . . . . 60

4.3 Etching parameters to achieve GaAS Nanowires of 1$\mu$m length . . . . . . . 67

4.4 Etching parameters for different tests to fabricate GaN Nanowires . . . . . 72

4.5 Parameters for SiN thin film deposition on GaN wafer . . . . . . . . . . . . 73

4.6 Etching parameters for SiN thin film deposited on GaN wafer . . . . . . . 73

4.7 Parameters for $SiO_2$ thin film deposition on GaN wafer . . . . . . . . . . . 73

4.8 Etching parameters for $SiO_2$ thin film deposited on GaN wafer . . . . . . . 74

6.1 Solar weighed absorption efficiencies for GaAs nanowire arrays . . . . . . . 128

# List of Figures

1.1 Schematics of the 4 × 4 cell of nanowire arrays on a substrate showing the conventions used for nanowire dimensions. . . . . . . . . . . . . . . . . . . . 12

2.1 Ray diagram indicating the Reflected and Transmitted waves in a Fabry-Perot cavity . . . . . . . . . . . . . . . . . . . . . . . . . . . . . . . . . 21

3.1 Schematics of the 2 × 2 cell of the semi-infinite nanowires for FDTD simulations with periodic boundary conditions in x and y-direction and PML boundary in z-direction. . . . . . . . . . . . . . . . . . . . . . . . . . . 25

3.2 FDTD calculations of absorptance of semi-infinite nanowire for different diameters indicating $HE_{11}$ and $HE_{12}$ modes with power monitor placed at 450 nm into the nanowires. . . . . . . . . . . . . . . . . . . . . . . . . . 27

3.3 FDTD calculated six mode components $E_x$, $E_y$, $E_z$, $H_x$, $H_y$, and $H_z$ of EM field in semi-infinite nanowire for 100 nm diameter . . . . . . . . . . . . . . 28

3.4 Excitation of $HE_{11}$ and $HE_{12}$ modes in GaAs nanowires as a function of wavelength and diameter. . . . . . . . . . . . . . . . . . . . . . . . . . . 29

3.5 (a)FDTD simulations for semi-infinite aSi nanowires for diameters 100-250 nm. Peaks P1 to P4 corresponding to the dominant resonant wavelengths for each diameter are shown in the table below (b)-(e) The radial mode shape for the resonant peaks and the 2-D mode profiles at y=0. . . . . . . 30

3.6 The excitation of $HE_{11}$ and $HE_{12}$ modes of a-Si nanowires as the function of diameter. . . . . . . . . . . . . . . . . . . . . . . . . . . . . . . . . 31

3.7 (a) Simulated absorption spectra for semi-infinite silicon nanowires for different diameter, showing the mode profiles at for wavelengths (P1-P4) (b) D vs $\lambda$ trends for the excitation of $HE_{11}$ and $HE_{12}$ modes. . . . . . . . . . 33

3.8 Resonant absorption peak vs refractive index for different semiconducting materials showing a linear relation between the n and resonant wavelengths. 34

3.9 The absorption in a-Si nanowires with different values of k and pitches. . . 36

3.10 The absorption peaks calculated in semi-infinite (a) GaAs (b) a-Si (c) Silicon nanowires with different pitches and 100 nm diameter. . . . . . . . . . . 37

3.11 Simulated absorption aSi nanowires with substrate at the bottom. The length of nanowires is 500 nm. . . . . . . . . . . . . . . . . . . . . . . . . 40

3.12 (a) Transmission of power through semi-infinite silicon nanowires calculated using FDTD till the length of 500 nm. (b) Logarithm value of the transmitted power plotted with the length of the nanowire along which the power transmits. . . . . . . . . . . . . . . . . . . . . . . . . . . . . . . . . . . 41

3.13 (a) Transmission of power through GaAs nanowires for diameter 100 nm calculated using FDTD simulations (b) Comparison of logarithmic value of power as a function of nanowire length along which the power transfers . . 43

3.14 Calculated electric field distributions for semi-infinite nanowires for (a) Square (b) Circular cross-sections having 100 nm diameter(c) Field distribution for circular cross-section having 113 nm diameter, thus having the same area of cross section as the square with 100 nm side. . . . . . . . . . . . . . . . . . 45

3.15 Calculated absorption contour plots for nanowires for (a) Square (b) Circular cross-section . The length is 1 $\mu$m for all the nanowires. . . . . . . . . . . 46

3.16 Calculated electric field distributions for semi-infinite nanowires for (a) Square having 200 nm side and (b) Circular cross-sections having 226 nm diameter. Both cross-sections represent almost the same area. . . . . . . . . . . . . . 47

4.1 Vapour Liquid Solid bottom-up approach to grow a single nanowire . . . . 50

4.2 Schematic of a nanowire fabrication process by dry etching . . . . . . . . . 55

4.3 Top-view SEM images of silicon nanowires at different pitches. . . . . . . . 59

4.4 Top-view and side-view SEM images of silicon nanowires with (a),(b)square and (c),(d)triangular cross-sections. The scale is 1$\mu$m for all figures. . . . . 61

4.5 Side-view SEM images of silicon nanowires with (a) Ordered (b) Disordered arrangement and (c) Tapered longitudinal profile. The scale bars are 1 $\mu$m for all figures. . . . . . . . . . . . . . . . . . . . . . . . . . . . . . . . 62

4.6 Side-view SEM images of a-Si nanowires fro four diameters (a) 100 nm (b) 150 nm (c) 200 nm and (d) 250 nm. The scale is 1$\mu$m for all figures. . . . . 63

4.7 (a)Top-view SEM of chrome masks after lift-off, (b) Side-view SEM of GaAS nanowires after etching of (a). (c)Top-view SEM of Al/Cr mask after lift-off, (d) Side-view SEM of GaAS nanowires after the etching of (c). The scale is 1$\mu$m for (a) and (b) and 1$\mu$m for (c) and (d). . . . . . . . . . . . . . . . . . 66

4.8 Side-view SEM images of GaAS nanowires for different diameters and pitches. The details for each figure are shown in the sub-captions. The scale is 1 $\mu$m for figures (a)-(e) and 2 $\mu$m for (f) . . . . . . . . . . . . . . . . . . . . . . . 69

4.9 TEM image of the GaAs nanowire with 135 nm dimeter. . . . . . . . . . . 70

4.10 Side-view SEM images of GaAs tapered nanowires with (a) 2.2 $\mu$m (b) 1.6 $\mu$m lengths. The scale is 1 $\mu$m for both figures. . . . . . . . . . . . . . . . . 71

4.11 Side-view SEM image of GaN nanowires for three diameters (a) 100 nm (b) 200 nm (c) 260 nm. The scale bar is 1 $\mu$m. . . . . . . . . . . . . . . . . . 74

4.12 The diameter distribution of silicon nanowires with 85 nm diameter and pitches ranging from 400 nm to 800 nm. The distribution for disordered nanowires is also plotted. . . . . . . . . . . . . . . . . . . . . . . . . . . . 75

5.1 Home made optical setups to measure (a) reflections and (b)transmissions from the nanowire samples . . . . . . . . . . . . . . . . . . . . . . . . . . 80

5.2 Reflectance spectra from 1 $\mu$m long GaAs nanowires spaced 400 nm from each other (a) 3-D contour plot of reflections for all the diameters (b) 2-D plot of reflections from 30 nm to 140 nm diameters (c) Reflections from 140 nm to 260 nm diameters (d) FDTD simulations matching the reflection spectrum of nanowires of 230 nm diameters. . . . . . . . . . . . . . . . . . 85

5.3 Reflectance spectra from 2.2$\mu$m long GaAs nanowires spaced 400 nm from each other (a) 3-D contour plot of reflections for all the diameters (b) 2-D plot of reflections from 40 nm to 135 nm diameters (c) Reflections from 145 nm to 205 nm diameters. . . . . . . . . . . . . . . . . . . . . . . . . . . . 86

5.4 Absorptance contour plot for (a) 1 $\mu$m long GaAs nanowires and (b) 2.2 $\mu$m long nanowires spaced 400 nm. . . . . . . . . . . . . . . . . . . . . . . . 88

5.5 Schematic of the aSi nanowires on glass . . . . . . . . . . . . . . . . . . . . 89

5.6 Reflection and transmission spectra of a-Si nanowires for four diameters 100 nm, 150 nm, 200 nm and 250 nm measured using the home made optical setup. . . . . . . . . . . . . . . . . . . . . . . . . . . . . . . . . . . . . 91

5.7 The absorption spectra of a-Si nanowires for four given diameters,. Also, the simulated spectra for semi-infinite and nanowires on glass setup are also shown for each diameter. . . . . . . . . . . . . . . . . . . . . . . . . . . . 94

5.8 Absorptance in bare nanowires for diameters (a) 150 nm (b) 200 nm and (c) 250 nm showing there is no absorption beyond the band gap in the absence of mask. Also, the peak intensities and F-P positions change due to the absence of mask. . . . . . . . . . . . . . . . . . . . . . . . . . . . . . 95

5.9 Reflection Colors of GaAs, Silicon and a-Si nanowires for different diameters 96

5.10 Experimental reflection measurements of 115 nm diameter nanowires with three different pitches and 1.6 $\mu$m length. FDTD simulations of reflectance of the same three pitches is also shown in dotted lines of same color. . . . . 98

5.11 (a)Reflection measurements of silicon nanowires of 85 nm diameters and 700 nm length at different pitches given in the figure.(b) Simulated reflectance spectra of silicon nanowires with substrate at the bottom and dimensions same as used for experimental study (c) The comparison of shift in resonant modes with the change in pitch for experiment and simulation results. . . . 99

5.12 Reflected colors from (a) GaAS (b) Silicon and (c) a-Si nanowires for different pitches . . . . . . . . . . . . . . . . . . . . . . . . . . . . . . . . . . 100

5.13 (a) Sideview (45°-tilt) SEM image of disordered silicon nanowires (b) the diameter distribution of disordered nanowires and ordered nanowires at different pitches . . . . . 102

5.14 Reflection measurements of ordered (green) and disordered (red) nanowires. The reflection from bulk silicon is also plotted for comparison. . . . . . . . 103

5.15 Side-view SEM image of GaN nanowires for three diameters (a) 100 nm (b) 200 nm (c) 260 nm . . . . . 105

5.16 (a) Reflection of nanowire arrays at different etch depths at 700 nm pitch and 85 nm diameter (b) Simulated reflections from the nanowires with the same diameter and pitch at similar etch depths. . . . . . 107

5.17 Tapered profiles of GaAs using different dry etching parameters and hard masks. . . . . . 108

5.18 Absorption spectra of tapered GaAs Nanowires for 100 nm base diameter and different pitches. . . . . . 109

5.19 (a)SEM image of the tapered silicon nanowires. (b) Comparison of reflectance from the cylindrical and tapered nanowires. . . . . . 110

5.20 Schematic 3-D representation of (a) Bare (b) Masked nanowires. . . . . . . 111

5.21 (a)SEM image of the tapered silicon nanowires. (b) Comparison of reflectance from the cylindrical and tapered nanowires. . . . . . 113

5.22 (a)SEM image of the tapered silicon nanowires. (c) Comparison of reflectance from the cylindrical and tapered nanowires. . . . . . 114

5.23 The FDTD simulation of absorption in the mask by putting power monitor just below it. The absorption spectra for bare and masked nanowires are also plotted. The diameter is 100 nm for this nanowire. . . . . . 115

5.24 (a)SEM image of the tapered silicon nanowires. (c) Comparison of reflectance from the cylindrical and tapered nanowires. . . . . . . . . . . . . 116

5.25 Electric field distributions in semi-infinite nanowires at 100 nm diameter for four different wavelengths. . . . . . . . . . . . . . . . . . . . . . . . . . . 117

5.26 Absorption spectra of nanowires at 100 nm diameter, 400 nm pitch at different lengths.The mask thickness is 30 nm. . . . . . . . . . . . . . . . . . . 118

5.27 Absorption spectra of nanowires of 100 nm diameter, 400 nm pitch and 1 $\mu$m length at different mask thicknesses. . . . . . . . . . . . . . . . . . . . . 119

6.1 (a) The schematic of GaAS nanowires etched on the top of GaAS/InGaP substrate (b) The schematic of nanowires after making the top contacts and removing the GaAs substrate. . . . . . . . . . . . . . . . . . . . . . . . . 125

6.2 (a) Reflection of nanowire arrays at different etch depths at 700 nm pitch and 85 nm diameter (b) Simulated reflections from the nanowires with the same diameter and pitch at similar etch depths. . . . . . . . . . . . . . . . . 127

6.3 Schematic of the a-Si nanowire/thin film platform on glass. . . . . . . . . . 130

6.4 Absorption spectra of a-Si nanowires with different diameters and thin film thicknesses. . . . . . . . . . . . . . . . . . . . . . . . . . . . . . . . . . . 132

6.5 The reflection and transmission spectra of a-Si nanowires having 100 nm diameter with three different thin film thicknesses (a) 0 nm (b) 55 nm (c) 145 nm (d) Absorption spectra of thin films for different thicknesses. . . . . 135

6.6 Reflection and Transmission colors of the platform having nanowire arrays with diameters and thin film thicknesses. . . . . . . . . . . . . . . . . . . . 138

6.7 Solar weighed absorptance for the platform having nanowire arrays with different diameters and thin film thicknesses (solid lines). The simulated calculations are also plotted (dashed lines). . . . . . . . . . . . . . . . . . . . 141

A.1 Extracted n and k of a-Si from a thin film of known thickness. . . . . . . . . 161

# Chapter 1

# Introduction

Understanding the interaction of photons with semiconductor nanostructures has inspired the optoelectronics industry to explore new empirical and conceptual realms in nanophotonics. This exploration has enabled the advances in digital camera technologies, photovoltaics, biosensors, lenses, displays, lasers, and batteries, increasing their throughput and efficiencies. Most of these ideas are pioneered by the people who were inspired by the naturally observed phenomenon occurring in nature such as photosynthesis on the surface of a leaf, the functioning of a moth eye or colorful wings of a butterfly. As these phenomena were inspected, it was realized that ordered nanostructures play a crucial role. This lead to a desire to engineer ordered nanostructures and use light interaction to improve the performance of the devices.

Semiconductor materials like Silicon, Germanium or III-V semiconductors have transformed the modern society in the past 60+ years by enabling the devices like transistors [1], lasers [2], light emitting diodes(LEDs) [3], photodetectors [4], solar cells [5] etc to lay the foundation of optoelectronic devices and research instruments, assisting humanity in many aspects of life. Semiconductor photonics still intrigues us in many ways from the application and conceptual point of views, especially when going down the size scale. In last

two decades, the microelectronics industry has revolutionized the modern electronics and optoelectronics industry by confining the millions of functions in a single chip conforming to Moore′s law [6]. However, eventually, the Moore′s law will no longer be applicable as the device size is approaching its physical limits [5]. The next challenge will be to increase the complexity in functionality, and increase the speed and lower the losses in already established designs e.g. optical networks, filters, photodetectors, data communication, lasers etc by using the nanoscale engineering [5]. Also, the optoelectronics community needs to look into the other directions to advance the parallel technologies such as quantum computing [7], bio-sensing [8], ultra-thin lenses [9], prosthetic devices [10] etc. The efforts to fabricate and optically understand the semiconductor devices at the nanoscale have been going on since 90s [11]. There has been a significant success in achieving certain morphology such as the 1-D, 2-D and 3-D nanostructures by various growth and etching techniques. The significant reduction in size has been proven to enhance certain properties like absorption, colors, Raman scattering, sensitivity, response time etc when compared to bulk materials.

Silicon has been the favorite material not only for having a high refractive index with low absorption coefficient but also for it′s low cost and abundance in availability. The efforts to increase absorption and consequently the efficiency are not only restricted to silicon but many other materials like amorphous silicon(a-Si) [12], direct band gap II-VI [13] and III-V [14] semiconductors. Going one step ahead, multi-junction materials have been developed and tested, utilizing sub-cell band gaps over the broad electromagnetic spectrum to achieve high efficiencies in sensing and photo-conversion applications [15].

The semiconductors at nano-scale show significantly different physical properties than bulk by confining the light in 2-dimensions(Thin films), 1-dimensions (Nanowires) or 0-dimensions(nanoparticles). Several new phenomena have been explored and applications are being developed based on those confinements. Nanowires among them have attracted a

great deal of attention in the past decade for their high surface to volume ratio. Nanowire morphologies have the dimensions of 2-250 nm in the radial direction and several microns in the longitudinal direction, which allows an entirely new physical regime of light-matter interaction.

## 1.1 Vertical Nanowires Ensembles as Optical Waveguides

Vertical semiconductor nanowires are one-dimensional optical waveguides with nanoscale radial dimensions. Being miniaturized waveguides they are potential candidates to be used in integrated photonic circuits as photodetectors, switches, filters etc. To be able to fulfill these functionalities, they need to effectively capture and deliver the optical signals to the next components in an optoelectronic circuit. Until recently, the nanowires had been known for their anti-reflective properties attributing the suppressed reflectivity to scattering and diffuse reflections [16–18] . However, not long ago some researchers including our group have started focusing on the waveguiding aspects of the nanowires and tried to understand them in terms of their optical confinement and transmission properties as a function of their diameter and lattice spacing [19–23]. The physical understanding of the interaction of light with sub-wavelength vertical waveguide arrays can be pictured by the comprehensive understanding of the cylindrically symmetric hybrid modes [24] and resonant coupling between the waveguides [25]. Having the sub-wavelength cross-section, the resonant modes in nanowires are essentially leaky and interact with surrounding medium as well. This is an appropriate design for sensing the change in refractive index of the surrounding medium [26]. At phase matching wavelength, the confinement is significantly higher than other wavelengths and creates sharp absorption peaks as observed in the anal-

ysis of silicon nanowires arrays. All these attributes make semiconducting nanowires as a nominee for known and unknown possibilities in nanophotonics and optoelectronics applications. Despite attracting a lot of attention from the leading researchers, the optical response of the nanowires was not very well understood at the beginning of this study.

## 1.2 Absorption in Nanowires

Anticipating the possible advantages of nanowire geometry, the absorption characteristics in nanowires have been studied exhaustively by many research groups. The effect of sub-wavelength ensembles on the reflection of light was first studied in the late 1960s when Bernhard demonstrated the anti-reflective properties of an array of sub-wavelength structures [27]. He figured that a periodic array of conical perturbations on the corneal lens of a moth-eye significantly lowers optical reflection. Then, Clapham *et al* [28] patterned photoresist on glass to create artificial moth-eye structures. They showed that the integrated specular reflection of white light was reduced to 0.2%. Gittleman *et al* extended this work for silicon nanopillars in 1979 [29], where they showed the reduction of specular reflection to $10^{-3}$ or less for wavelengths below 1 $\mu$m. Craighead *et al* also reported the reduced reflection in thin film a-Si to nearly zero over the visible spectrum [30]. Since then a lot of groups are studying the anti-reflective studies on semiconductor nanowires for different materials. In recent studies, a strong broadband absorption was observed for silicon nanowires on glass substrates, which was found to be higher than the thin film of equal thickness but the origins were not understood [31]. Convertino *et al* [32] studied the reflection properties of disorder silicon nanowires for wide range diameters (from 30 nm to 250nm) with different filling factors and observed that they can be tuned as an antireflective coating to a highly reflecting ensemble depending on the fill factor. Another group showed a broadband and omnidirectional antireflection properties for GaP nanowires [33].

Zhu *et al* [34] showed that hydrogenated amorphous silicon (a-SI:H) nanocone arrays on the top of indium tin oxide(ITO) and a-Si substrate absorb more than 90% of the incident light for incident angles up to 60°. For nanowire array, the absorption was 70%, which was still higher than thin films (45%). There have been these experimental demonstrations but no fundamental understandings of the origins. This makes optimization of the structures difficult.

## 1.3 Nanowires for Optoelectronics

The anisotropic geometry and the high surface to volume ratio of the nanowires allow them to confine the carriers and photons to one dimension, which enables longer diffusion length for electrons and larger optical path length for photons compared to thin films and bulk [35]. Also, the one-dimensional morphology of nanowires has better light trapping ability than thin film and bulk due to the waveguiding properties mentioned in the section 1.1. Compared to the organic and metallic nanostructures, the semiconducting properties of nanowires enables them to tune their electronic properties more conveniently. This geometry while affording the directional flow of carriers in a preferential direction, also contributes in reducing dark current, increasing photoconductive gain [36] and operational speed [37]. This makes nanowires a good candidate for optoelectronic applications. Thus, nanowires offer a good design for the materials having optical absorption length much longer than the carrier diffusion length as they can be utilized to collect photocurrent in both radial and longitudinal directions.

### 1.3.1 Photovoltaics

Generally, in solar cell design, the major issue is the trade-off between device performance (efficiency) and cost. The minimum limit for the thickness required for a cell is where it absorbs more than 90% of the incident light. Impurities in a material can increase the effective absorptance, however, they put constraints on the efficiency of the cell due to short carrier lifetimes. One way to tackle this problem is orthogonalization of the direction of photon absorption and collection of charge carrier. Nanowires can provide a longitudinal dimension for light absorption and a radial direction for the collection of carriers. Many groups have attempted to create p-n junction nanowires in radial and axial direction. That way low-grade materials can be utilized to reduce the manufacturing cost. In 1992, an axial p-n structure was realized for GaAs nanowires for the first time [38], which laid the foundation of p-n nanowire structures for application in photovoltaics. Kayes *et al* [39] also proposed a nanowire structure of p-type core and n-type shell to minimize the diffusion length of photogenerated carriers.

Among reported studies on semiconductor nanowire solar cells so far, different materials have been used depending upon the advantages possessed by each of them. Silicon has the advantage of being abundantly available and less costly. Moreover, it also possesses the disadvantage of having low absorption coefficient due to indirect band gap. Garnet and Yang have reported the core-shell p-n junction solar cells with single crystalline silicon core and polycrystalline silicon shell achieving 0.5% efficiency [35]. In another study, coaxial p-n Si nanowire array grown on stainless steel substrate showed the efficiency of 0.1% [40]. Si nanowires fabricated on glass substrate by wet electrolytic etching yielded efficiency of 4.4% and is the highest reported efficiency on Silicon nanowire arrays [31]. There are other studies on Si nanowires but nothing has surpassed the 4.4% mark yet [35, 41–43]. In order to overcome the limitations of silicon-based solar cells, the research community had

resorted to direct band gap materials for the higher absorption and consequently higher conversion efficiencies. Along with planar solar cells, this shift was also seen in nanowire solar cells designs too. There is a study demonstrating dye-sensitized solar cells using ZnO nanowires and getting efficiencies of 0.5% to 1.5% [44]. Goto *et al* reported p/n core/shell photovoltaic design for InP nanowires [45]. Mehta and Kruis showed the band gap tuning in the tapered nanowire of different semiconducting materials (from II-VI to III-V) by varying the diameter along the length [46]. Ray LaPierre *et al* pioneered the work on GaAs nanowire array solar cells for core/shell radial junction and reported the PCE of 0.83%. Afterward many groups attempted to increase the PCE in the radial p-i-n junction in GaAs nanowire solar cells [47, 48]. Tegude *et al* successfully achieved it up to 4.7% using single GaAs/InGaP/GaAs radial p-i-n junction nanowire [49]. Including the ones mentioned above, there are recent advancements demonstrating efficiencies above 5% for nanowire geometry, for example very recently Yao *et al* [50] proposed axial p-i-n solar cell with optimized array geometry to achieve high absorption. They further optimized the junction depth and nanowire diameter to achieve efficiency up to 7.58%, highest reported efficiency for GaAs nanowire solar cells so far. The exact same design parameters influence the InP nanowire array solar cell to achieve the efficiency up to 13.8%, reported by Wallentin *et al* [51]. The low junction depth and highly absorbing diameter provided efficiencies never achieved before in solar cell design for GaAs and InP nanowires. In past few years, the paradigm shift is towards multijunction solar cells. Multijunction solar cells use multiple band gaps of different materials to trap the broad solar spectrum at different wavelength ranges. The added advantage is that the asymmetrical energy barrier in such devices renders the charge diffusion and recombination more difficult. King *et al* [15] reported the GaInP/GaInAs/Ge multijunction solar cell to achieve 40% efficiency in planar configuration. Tang *et al* [52] grew p-type GaN nanowires on n-type Silicon substrate and achieved 2.73% power conversion efficiency. There is still a lot of work

needed in multijunction and single nanowire solar cells to achieve higher efficiencies. To achieve this, one needs to have the comprehensive understanding of the optical properties of semiconductor nanowires.

### 1.3.2 Other Optoelectronics Applications

Based on their novel optical and electrical properties, semiconductor nanowires have been seen as a potential candidate for advanced optoelectronic applications. In one simulations study, the silicon-based photonic crystals were proposed as the reflective color filters inspired from butterfly wings [53]. In another study, Park *et al* experimentally demonstrated the filter free image sensors using p-i-n doped vertical silicon nanowires [54]. The same group also experimentally demonstrated nanowires based photodetector integrated with bulk semiconductor photodetector making it more efficiently absorbing than conventional photodetectors [55]. GaAs/AlGaAs core-shell photodetector was demonstrated by Dai *et al* with photoresponsivity in 300- 890 nm wavelength range [56]. Yang *et al* presented the optical gating phenomena with ZnO nanowires by changing the conductivity of nanowires using ultraviolet exposure demonstrating the phenomena of optical switching and UV photodetection using nanowires [57]. The excellent waveguiding properties of semiconductor nanowires has also led the researchers to explore their lasing properties. Simulated emission of nanowires has been proposed and demonstrated for various large band-gap materials such as GaAs [58, 59], GaN [60–62], ZnO [63] and CdS [62, 64] for a wide range of wavelengths.

### 1.3.3 Sensing

The small size and large surface to volume ratio of nanowires make them an attractive candidate for the sensing of biological systems. Patolsky *et al* showed the electrical detection

of single viruses using nanowire-based field effect transistors(FETs) [65]. The electrophysiological measurements of single neurons have been demonstrated by interfacing them with silicon nanowires [66]. The label-free detection of DNA [67] and cancer markers [68] is also demonstrated using silicon nanowire arrays. The refractive index sensing using the waveguiding [26] and diffraction [69] properties of vertical silicon nanowire arrays was demonstrated in achieving the refractive index resolutions of $5e-5$ and $10e-6$ respectively.

## 1.4 Motivation and Thesis Outline

Most of the semiconductor nanowires based solar cells are fabricated using various growth techniques on the top of silicon, glass, metal or other semiconductor substrates. One advantage of these methods is that lattice mismatch of nanowire and substrate is accommodated in the small radially dimensioned nanowires due to the elastic relaxation at the surfaces. However, there are certain factors in the nanowire growth that need to be improved, such as the reproducibility of the identical structures, control over shape, position, length, doping concentrations and crystal orientation of the nanostructures. These parameters have to be consistent and reproducible especially when the conversion efficiencies directly or indirectly depends on all these features. In order to achieve consistency, the top down dry etching is the more suitable method. Silicon nanowires with controlled diameter, length and lattice spacing using dry etching have already been achieved and reported [70]. But there is a dire need to achieve that in a-Si and III-V semiconducting nanowires for the added advantage they have in solar absorption. On the top of it, the dry etching provides the surface passivation polymer on the sidewalls, which can be helpful in reducing surface recombination of photogenerated carriers.

In this thesis, the fabrication and optical properties of Silicon, a-Si, GaAs, and GaN nanowires are discussed in detail and their potential applications in photovoltaics and pho-

todetectors are explored by engineering their optical response. Silicon being the abundant and low-cost material is widely used in the modern microelectronics industry. However, a-Si and III-V semiconducting materials have an advantage over silicon in absorption efficiencies due to their direct band gaps. GaAs and GaN are known for their high mobility and direct band gap and used in wide range of optoelectronics applications. Due to the small variation in diameters and excellent reproducibility, waveguiding properties of nanowires have been experimentally demonstrated showing different physical phenomena. In chapter 2, the mathematical formulations for the interaction for cylindrical waveguides with electromagnetic waves are presented. The confined, leaky, photonic crystal and longitudinal modes have been discussed with relevant equations. These form the basis to understand the waveguiding nature of the nanowires. However, as seen later, they don't provide a complete picture and sometimes give cumbersome results. In chapter 3 the Finite Difference Time Domain(FDTD) simulations are used to visualize the results expected from chapter 2 and various physical phenomena are discussed using 2-D plots and mode visualizations. To experimentally verify these theories, the high-quality periodic nanowire ensembles were fabricated using inductively coupled plasma reactive ion etching (ICP-RIE). The etching recipes to fabricate nanowires were developed during the research. The details of the processes and results are discussed in chapter 4. The semiconducting materials we chose to etch are abundantly used for optoelectronics applications i.e. silicon, a-Si, GaAs, and GaN. Etching of their variants has already been demonstrated at micro-scale for state of the art devices. We, however, etched them to the nanoscale and demonstrated good control over their dimensions and sidewall smoothness. GaAs is etched $Cl_2/N_2$ etching recipes using different hard masks to achieve vertical,and smooth sidewalls. Furthermore, the control over its taperedness is also tested using different combinations of the masks. Shape control was also achieved for silicon nanowires by changing passivation in the etch process. GaN being the hard material was tested with different metal and dielectric hard masks.

In chapter 5, the optical measurements of the nanowires have been discussed to confirm the results that are discussed in chapter 3. The analysis is further extended to see the effect of disordered arrangements, tapered profiles, aluminum mask to manipulate the absorptance behavior of the nanowires. The experimental analysis of the excitation of leaky waveguide modes, waveguide coupling and F-P cavity modes in nanowires are discussed in this chapter. The nanowires typically have a diameter of 100 nm and pitch 400 nm to discuss most of these properties as the diffraction behavior is suppressed at this scale for the visible range. In chapter 6, the GaAs and a-Si nanowires have been explored for the potential application by removing the effect of the substrate from them. The detailed optical analysis and along with the solar weighed absorptance of these nanowires are discussed to create the optical designs for photovoltaics, photodetectors, and filters. This thesis provides complete understanding optical properties of the nanowires by comparing results across different semiconductors. The thesis also demonstrates novel platforms for various applications using semiconducting nanowires.

Figure 1.1 shows the schematic of the nanowire arrays and the various terms used in the thesis are summarized here. The dimensions of the nanowires are defined by the diameter and the length. For this study, the nanowires were arranged in a square lattice and the spacing between the nanowires is defined by the pitch. The nanowires/air interface represents the top of the nanowires and the nanowires/substrate interface is at the bottom. The arrays were typically made in 100 $\mu$m $\times$ 100 $\mu$m squares and contained $\sim$62500 nanowires approximately at 400 nm pitch. We found that at this size, long range order still existed while multiple arrays could be placed on the same sample for comprehensive studies.

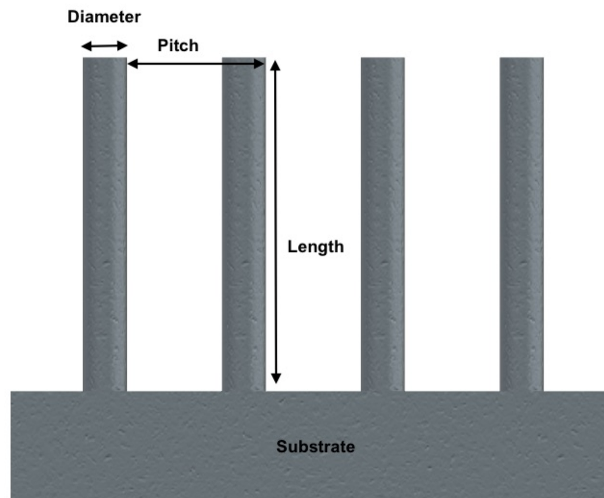


Figure 1.1: Schematics of the 4 × 4 cell of nanowire arrays on a substrate showing the conventions used for nanowire dimensions.

# Chapter 2

# Theoretical Concepts

## 2.1 Introduction

Semiconductor nanowires are the cylindrical waveguides that confine light in wavelengths comparable to their diameters. The confinement of light in nanowires could lead to either the bound modes or the leaky modes depending on the cut-off conditions of the normalized frequency and the $V$ parameter of the individual nanowire [71]. The periodic ensembles of the nanowires make their interaction with light more complex when confined photons in individual nanowire interact with neighboring nanowires due to the near-field coupling. Moreover, while moving towards larger diameters, the nanowires could also act as F-P cavities at low absorbing wavelengths because of light bouncing back and forth. Various optical modes and coupling make it hard to predict how the nanowires would behave at different wavelengths. The understanding of all these phenomena requires a mathematical treatment based on Maxwell Equations to get intuitive feelings.

In this chapter, we will discuss a mathematical model for the modal analysis in cylindrical waveguides, the waveguide coupling, and F-P cavities.

## 2.2 Cylindrical Waveguide Modes

The modal excitation in cylindrical waveguides is dominated by the total internal reflections of light along the periphery of the cylinder following the helical path. Due to this reason the z component of the electric and magnetic fields cannot be entirely eliminated in cylindrical waveguides, hence the radial modes are named hybrid HE and EH modes. This is especially true for semiconductor nanowires as the refractive index difference is quite large. Due to their small size of the nanowires, the resonant modes in nanowires become leaky and interact more effectively with the outside world, and could get coupled to each other.

To solve the modes, we need to use the cylindrical coordinates $E_r$, $E_\phi$, $E_z$, $H_r$, $H_\phi$, $H_z$ for more intuitive and convenient formulations. The Helmholtz's wave equations for z components of Electric and Magnetic field are given as:

$$(\nabla^2 + k^2)E_z = 0 \qquad (2.1)$$

$$(\nabla^2 + k^2)H_z = 0 \qquad (2.2)$$

where $k = \omega n/c$ is called the propagation constant in the absence of waveguiding. n is the refractive index of the material The $r$ and $\phi$ components of the electric and magnetic fields propagating in $z$ direction an be represented as the functions of $z$ and $t$

$$E(r,t) = E(r,\phi)e^{j(\omega t - \beta z)} \qquad (2.3)$$

$$H(r,t) = H(r,\phi)e^{j(\omega t - \beta z)} \qquad (2.4)$$

Thus, the $r$ and $\phi$ components can be derived from the $z$ components using Maxwell's equations.

Expanding laplacian operator in equations (2.1) and (2.2) gives

$$\left(\frac{\partial^2}{\partial r^2} + \frac{1}{r}\frac{\partial}{\partial dr} + \frac{1}{r^2}\frac{\partial^2}{\partial \phi^2} + (k^2 - \beta^2)\right)E_z = 0 \qquad (2.5)$$

$$\left(\frac{\partial^2}{\partial r^2} + \frac{1}{r}\frac{\partial}{\partial r} + \frac{1}{r^2}\frac{\partial^2}{\partial \phi^2} + (k^2 - \beta^2)\right)H_z = 0 \quad (2.6)$$

and solution to these equations is:

$$E_z = e(r)e^{\pm jp\phi} \quad (2.7a)$$

$$H_z = e(r)e^{\pm jp\phi} \quad (2.7b)$$

where p = 0,1,2,...., thus making the equations (2.5) and (2.6) as:

$$\frac{\partial^2 E_z}{\partial r^2} + \frac{1}{r}\frac{\partial E_z}{\partial dr} + \left((k^2 - \beta^2 - \frac{p^2}{r^2})\right)E_z = 0 \quad (2.8)$$

$$\frac{\partial^2 H_z}{\partial r^2} + \frac{1}{r}\frac{\partial H_z}{\partial dr} + \left((k^2 - \beta^2 - \frac{p^2}{r^2})\right)H_z = 0 \quad (2.9)$$

If $k^2 - \beta^2 < 0$, the solutions to the equations are the Bessel functions of first($J_p$)and second($Y_p$) kind and given by:

$$E_z(r) = a_1 J_p(lr) + a_2 Y_p(lr) \quad (2.10)$$

$$H_z(r) = a_1 J_p(lr) + a_2 Y_p(lr) \quad (2.11)$$

where $a_1$ and $a_2$ are constants and $l^2 = \beta^2 - k^2$

and if $k^2 - \beta^2 > 0$, the solutions to the equations are the modified Bessel functions of first($I_p$)and second($K_p$) kind and given by:

$$E_z(r) = a_1 I_p(mr) + a_2 K_p(mr) \quad (2.12)$$

$$H_z(r) = a_1 I_p(mr) + a_2 K_p(mr) \quad (2.13)$$

where $m^2 = k^2 - \beta^2$

Physically, equations (2.10) - (2.13) represent the radial dependence of electric and magnetic fields in cylindrical waveguides. To ensure the evanescent decay of the field outside

the nanowires, $\beta$ must be larger than the $k(i.e.k_\circ n_2)$ and the modified Bessel function of second kind ($K_p$) physically describes the guided modes outside the nanowires. On the other hand, Hankel function (${H^1}_p$) physically describes the leaky modes. Thus the expression for the electric field outside the cylinders for guided and leaky modes are respectively:

$$E_z(r,t) = C_{air} K_p(lr) e^{j(\omega t + q\phi - \beta z)} \tag{2.14}$$

$$E_z(r,t) = C_{air} H_p(lr) e^{j(\omega t + q\phi - \beta z)} \tag{2.15}$$

where $H_p^1 = J_p(x) + jY_p(x)$ and $C_1$ is a constant. The solutions could similarly be derived for magnetic field. For fields inside the nanowires, the tangential components of electric and magnetic field need to be matched at the waveguide-air interface and fields need to be finite in the center of the nanowires, which can be only be satisfied using $J_p$ and hence $a_2$ needs to be set to zero in equation (2.10) and (2.11) resulting in:

$$E_z(r,t) = C_{core} K_p(mr) e^{j(\omega t + q\phi - \beta z)} \tag{2.16}$$

where $C_{core}$ is a constant and $m^2 = n_{core}^2 k_\circ^2 - \beta^2$

Again, the solution for magnetic field can also be generated using similar conditions having its own constants corresponding to $C_{air}$ and $C_{core}$. Moreover, all the other field components can be calculated for electric and magnetic fields and the constants can be eliminated by equating the fields at the boundaries generating the mode equation to be

$$\left(\frac{J_p'(ma)}{maJ_p(ma)} + \frac{K_p'(la)}{laK_p(la)}\right)\left(\frac{n_{core}^2 J_p'(ma)}{maJ_p(ma)} + \frac{n_{air}^2 K_p'(la)}{laK_p(la)}\right) = q^2\left[\left(\frac{1}{la}\right)^2 + \left(\frac{1}{ma}\right)^2\right]^2 \left(\frac{\beta}{k_\circ}\right)^2 \tag{2.17}$$

for confined modes, where $l^2 = \beta^2 - k_\circ^2$ and

$$\left(\frac{J_p'(ma)}{maJ_p(ma)} - \frac{H_p'(l_1a)}{l_1aH_p(l_1a)}\right)\left(\frac{n_{core}^2 J_p'(ma)}{maJ_p(ma)} - \frac{n_{air}^2 H_p'(l_1a)}{l_1aH_p(l_1a)}\right) = q^2\left[\left(\frac{1}{l_1a}\right)^2 - \left(\frac{1}{ma}\right)^2\right]^2 \left(\frac{\beta}{k_\circ}\right)^2 \tag{2.18}$$

for leaky modes, where $l_1^2 = k_\circ^2 - \beta^2$

The above equations are quadratic in $\frac{J_p'(ma)}{maJ_p(ma)}$ with the possibility of having two solutions, each corresponding to EH and HE modes. Solving for $\frac{J_p'(ma)}{maJ_p(ma)}$ obtains:

$$\frac{J_{p+1}(ma)}{maJ_p(ma)} = \left(\frac{n_{core}^2 + n_{air}^2}{2n_{core}^2}\right)\frac{K_p'(la)}{laK_p(la)} + \left[\left(\frac{1}{(la)^2}\right) - \left(\left(\frac{n_{core}^2 - n_{air}^2}{2n_{core}^2}\right)^2\left(\frac{K_p'}{laK_p}\right) + \frac{p^2}{n_{core}^2}\left(\frac{\beta}{k_\circ}\right)^2\left(\frac{1}{l^2a^2} + \frac{1}{m^2a^2}\right)^2\right)^{\frac{1}{2}}\right] \tag{2.19}$$

for EH modes and

$$\frac{J_{p-1}(ma)}{maJ_p(ma)} = -\left(\frac{n_{core}^2 + n_{air}^2}{2n_{core}^2}\right)\frac{K_p'(ma)}{maK_p(ma)} + \left[\left(\frac{1}{(ma)^2}\right) - \left(\left(\frac{n_{core}^2 - n_{air}^2}{2n_{core}^2}\right)^2\left(\frac{K_p'}{maK_p}\right) + \frac{p^2}{n_{core}^2}\left(\frac{\beta}{k_\circ}\right)^2\left(\frac{1}{l^2a^2} + \frac{1}{m^2a^2}\right)^2\right)^{\frac{1}{2}}\right] \tag{2.20}$$

for HE modes.

The subscript q in the modes ($HE_{qp}$, $EH_{qp}$) represent azimuthal components ($\phi$ dependence) of the field (q) and p represents the eigenvalues of $\beta$. The cutoff conditions for the modes are represented as:

$$\left(\frac{1}{\lambda}\right)_{qp} = \frac{\psi_{qp}}{2\pi(n_{core}^2 - n_{air}^2)^{\frac{1}{2}}}$$

where $\psi_{qp}$ is the pth root of $J_p(x)$. These equations suggest hat the incident field is funneled into optical modes and if the conditions are right,a resonant excitation of the guided modes will happen.

## 2.3 Bloch Mode Coupling with Radial Modes in Periodic Arrays

Since the nanowires are arranged in long range order, their absorption characteristics can change due to the presence of photonic crystals modes. The modes exist due to the excita-

tion of Bloch mode because of periodic symmetry of the nanowires and can be considered analogous to the perturbation of energy levels of atoms in a crystal compared to an individual atom. In one simulation study for silicon nanowire arrays [72], it was observed that the $E_z$ component of the resonant modes were dominated by Bloch modes and showed dipolar distribution. Mathematically, being dipolar in nature, the first order modal excitations in nanowire arrays should be showing the behavior of the first order Bessel function outside the nanowires as well. Hence, using the cylindrical coordinates the wave equations are:

$$E_{z(in)} = C_\circ J_p^1(mr)e^{j\phi} \qquad (2.21)$$

for inside the nanowires and

$$E_{z(out)} = C_1 J_p^1(l_1 r)e^{j\phi} + C_2 H_p^1(l_1 r)e^{j\phi} \qquad (2.22)$$

for outside the nanowires

where p = 1 for all the first order terms

The first order perturbation due to the neighbouring nanowires in the infinite lattice is shown using the Rayleigh identity:

$$C_1 = \zeta_\circ C_2 \qquad (2.23)$$

for the first order dipole fields

At the boundary conditions of the nanowire circumference, the constants are eliminated by equating equations (2.21) and (2.22), which gives us the fields inside and outside the nanowires as:

$$E_{z(in)} = \frac{1}{J_p(ma)}\left[H_p^1(l_1 a) + \zeta_\circ J_p(l_1 a)\right] J_p(lr) C_2 e^{j\phi} \qquad (2.24)$$

$$E_{z(out)} = \left[H_p^1(l_1 a) + \zeta_\circ J_p(l_1 a)\right] C_2 e^{j\phi} \qquad (2.25)$$

and similarly the expressions can be derived for the magnetic field ($H_z$). Using Maxwell's equations the $\phi$ components of the electric and magnetic fields can be derived from the $z$ components as:

$$E_\phi = \frac{j}{k}\left[\frac{\beta_z}{r}\frac{\partial E_z}{\partial \phi} - \omega\mu_\circ\mu_{core}\frac{\partial H_z}{\partial r}\right] \qquad (2.26)$$

$$H_\phi = \frac{j}{k}\left[\frac{\beta_z}{r}\frac{\partial H_z}{\partial \phi} - \omega\epsilon_\circ\epsilon_{core}\frac{\partial HEz}{\partial r}\right] \qquad (2.27)$$

Matching the fields at the cylindrical boundary of the nanowires gives the expression as :

$$\left(\frac{J_p'(ma)}{maJ_p(ma)} - \frac{H_p'(l_1a) + \zeta_\circ J_p^{1'}(l_1a)}{l_1aH_p(l_1a) + \zeta_\circ J_p^1(l_1a)}\right)\left(\frac{n_{core}^2 J_p'(ma)}{maJ_p(ma)} - \frac{n_{air}^2 H_p'(l_1a) + \zeta_\circ J_p^{1'}(l_1a)}{maH_p(ma) - \zeta_\circ J_p^1(l_1a)}\right)$$
$$= q^2\left[\left(\frac{1}{l_1a}\right)^2 + \left(\frac{1}{ma}\right)^2\right]^2\left(\frac{\beta}{k_\circ}\right)^2 \qquad (2.28)$$

If the nanowires are very far apart from each other, the fields do not overlap with each other, which makes $\zeta_\circ = 0$ in equation (2.28) giving:

$$\left(\frac{J_p'(ma)}{maJ_p(ma)} - \frac{H_p'(l_1a)}{l_1aH_p(l_1a)}\right)\left(\frac{n_{core}^2 J_p'(ma)}{maJ_p(ma)} - \frac{n_{air}^2 H_p'(l_1a)}{l_1aH_p(l_1a)}\right)$$
$$= q^2\left[\left(\frac{1}{l_1a}\right)^2 - \left(\frac{1}{ma}\right)^2\right]^2\left(\frac{\beta}{k_\circ}\right)^2 \qquad (2.29)$$

which is the same expression for the leaky modes for individual nanowires in equation (2.18).

In the previous work [22], while studying the photonic crystal bands for nanowires arrays at two different spacings 150 nm and 250 nm, it was suggested that the photonic modes of nanowire arrays started matching the leaky modes of single nanowires at an inter-nanowire spacing of 250 nm. These simulation studies suggest that the nanowires start to decouple

at this pitch and can be considered as individual waveguides. However, in our study, as will be seen in the future chapters, the photonic modes remain in the arrays at inter-nanowires spacings much larger than 250 nm, showing that long-range order exists and to accurately represent nanowires arrays, one has to use higher order Rayleigh coefficients. This becomes cumbersome and it is easier to first simulate arrays to understand the properties. We will consider the simulations in the next chapter.

## 2.4 Fabry-Perot Microcavity Modes

Fabry-Perot cavities are the parallel plate optical resonators having the parallel partially reflecting mirrors at its both ends as shown in figure 2.1. Let the distance between two parallel plates be L, the refractive index of the medium be n, and wavelength of incoming wave at angle $\theta$ be $\lambda$. The phase shift between the two successive reflections is:

$$\sigma = \frac{4\pi nL\cos\theta}{\lambda}$$

Thus, if the complex amplitude of the incoming wave is A, then the reflection amplitudes can be calculated as:

$$R_1 = rA, R_2 = tt_1r_1Ae^{-j\sigma}, R_3 = tt_1r_1^3Ae^{-2j\sigma}.... \tag{2.30}$$

where $r, r_1, t, t_1$ are the reflection and transmission coefficients for waves travelling from $n_1$ to $n$ and from $n$ to $n_1$ respectively as shown in the figure 2.1. The resultant amplitude of all the reflected waves is

$$R_{tot} = R_1 + R_2 + R_3..... + R_n \tag{2.31}$$

$$R_{tot} = [r + tt_1r_1e^{-j\sigma}(1 + r_1^2e^{-j\sigma} + r_1^4e^{-2j\sigma}...)]A \tag{2.32}$$

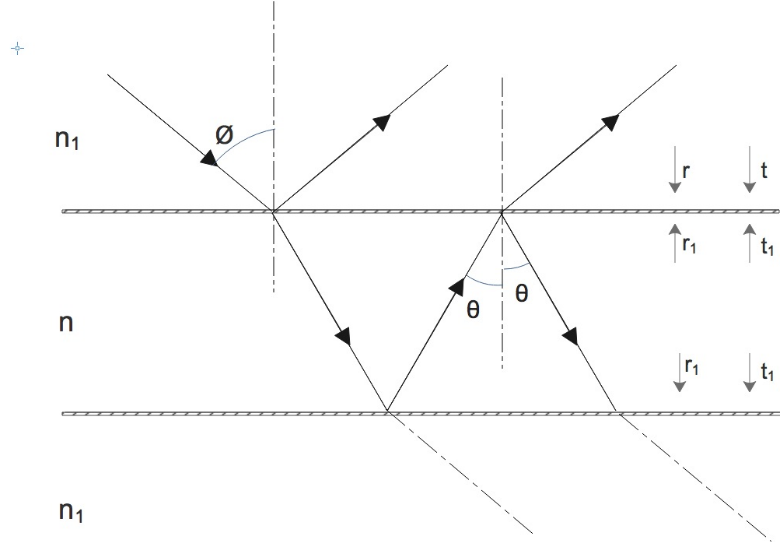


Figure 2.1: Ray diagram indicating the Reflected and Transmitted waves in a Fabry-Perot cavity

adding the infinite series, we get:

$$R_{tot} = \frac{1 - e^{-j\sigma}\rho}{1 - \rho e^{-j\sigma}} \tag{2.33}$$

where $\rho = r^2, r_1^2$, the fraction of energy reflected from a surface, also referred as reflectance. and the fraction of energy that is reflected can be written as:

$$\frac{I_r}{I_i} = \frac{R_{tot}R_{tot}^{\star}}{AA^{\star}} = \frac{4\rho sin^2(\sigma/2)}{(1-\rho)^2 + 4\rho sin^2(\sigma/2)} \tag{2.34}$$

For the lossy mediums, the absorption coefficient $\alpha$ is introduced to the medium properties. The transmission intensity becomes:

$$\frac{I_t}{I_i} = \frac{T_{tot}T_{tot}^{\star}}{AA^{\star}} = \frac{(1-\rho)^2 e^{-\alpha L}}{(1 - e^{-\alpha L}\rho)^2 + 4e^{-\alpha L}\rho sin^2(\sigma/2)} \tag{2.35}$$

The amplitude of transmitted waves are:

$$T_1 = tt_1 Ae^{-j\sigma/2}, T_2 = tt_1 r_1^2 e^{-j\sigma} Ae^{-j\sigma/2}, T_3 = tt_1 r_1^4 e^{-j2\sigma} Ae^{-j\sigma/2} \tag{2.36}$$

adding up all the terms:

$$T_{tot} = T_i t t_1 (1 + r_1^2 e^{-j\sigma} + r_1^4 e^{-j2\sigma} + ..) e^{-j\sigma/2} \tag{2.37}$$

adding the infinite series, we get:

$$T_{tot} = \frac{\tau e^{-j\sigma} r_1^2}{1 - \rho e^{-j\sigma}} \tag{2.38}$$

where $\tau = tt_1$, the fraction of energy transmitted from a surface, also referred as transmittance. The fraction of energy that is transmitted can be written as:

$$\frac{I_t}{I_i} = \frac{T_{tot} T_{tot}^{\star}}{AA^{\star}} = \frac{(1-\rho)^2}{(1-\rho)^2 + 4\rho sin^2(\sigma/2)} \tag{2.39}$$

For the lossy mediums, the absorption coefficient $\alpha$ is introduced to the medium properties. The transmission intensity becomes:

$$\frac{I_t}{I_i} = \frac{T_{tot} T_{tot}^{\star}}{AA^{\star}} = \frac{(1-\rho)^2 e^{-\alpha L}}{(1 - e^{-\alpha L}\rho)^2 + 4 e^{-\alpha L} \rho sin^2(\sigma/2)} \tag{2.40}$$

Equation (2.40) provides us with significant physical understanding. As the phase is changed due to change in wavelength, $sin^2(\sigma/2)$ will vary from 1 to 0 and $I_t$ will go from maxima to minima. Thus, an oscillatory response will be observed if we measure transmission and reflection with wavelengths. Further, if $\alpha$ is large, then the effect of changing value of $sin^2(\sigma/2)$ becomes small. So when the absorption is large, the ratio maxima of $I_1$ to minima $I_\circ$ will become small and weak oscillatory behavior would be seen. On the other hand, for small $\alpha$ large oscillatory response is achieved. Since the nanowires have reflections at nanowire/air interface and nanowire/substrate interface, F-P modes will exist. By studying the depth of the fringes, a lot can be known about the loss. We will later demonstrate some surprising results for nanowire arrays by studying F-P fringes. We were the first ones to point out that these fringes tell a lot about the absorption values. In the presence of absorption coefficient $\alpha$, the exponential decay of the power inside the cavity due to material absorption will reduce the transmitted power. The one-way passage loss in the cavity due to $\alpha$ can be defined as 1-A, where A $= e^{(-\alpha L)}$ for a cavity of length L.

## 2.5 Conclusion

In this chapter, we have discussed the mathematical formulations of physical phenomena occurring within nanowires arrays when they interact with visible light. The cylindrical waveguide modes excited in nanowires as a function of diameter are discussed in cylindrical coordinates. The analytical explanations for the hybrid modes are discussed. Later, the Bloch modes excitation in the period array of nanowires and their effect on nanowire absorption with the change in periodicity are mathematically explained. Lastly, the general formulation of F-P cavity with dielectric interfaces on the both sides of the cavity are explained, which will play important role in explaining spectral features in longer wavelengths. Thus, the good physical understanding of these modes has been demonstrated. However, these mathematical formulations do not provide the complete picture. The picture is completed by the FDTD models described in the next chapter.

# Chapter 3

# Simulation Studies of Semiconductor Nanowires

## 3.1 Introduction

As we discussed in the last chapter, the interaction of electromagnetic waves with the cylindrical waveguides can be formulated mathematically using the Maxwell′s equations but still need to be solved numerically. To analyze different geometries, it is imperative to find the numerical solutions for a given set of parameters using computer simulations. Finite Difference Time Domain(FDTD) is the simple and accurate full-wave technique to solve a wide range of problems involving electromagnetism. The nature of FDTD simulations is to use finite differences to approximate the spatial and time derivatives of Maxwell′s equations. We used RSoft CAD environment to run the FDTD simulations for our designs. FDTD works especially well for the domains that are somewhere on the order of the wavelength in size. Therefore, this method works perfectly well for our designs where nanowires are ∼50-250 nm diameters in the range corresponding to electromagnetic wave excitations in the visible and near-IR region. To obtain a reasonable approximation to the differential

equations, the grid size (based on Yee′s mesh) should be sufficiently small to give accurate results. In our simulations, we used 4 nm grid size and have periodic boundary conditions in x and y directions making a unit cell consisting of 2 × 2 array.

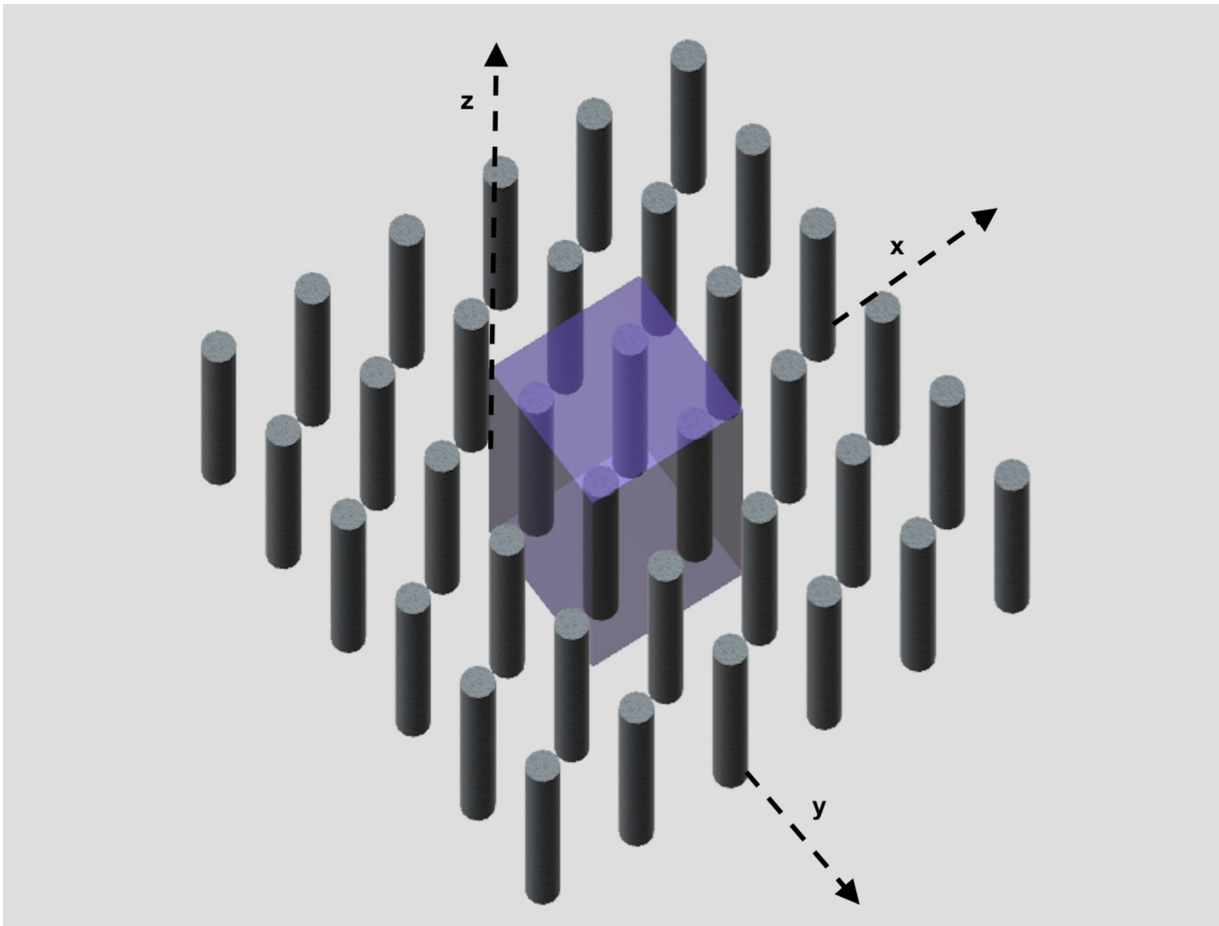


Figure 3.1: Schematics of the 2 × 2 cell of the semi-infinite nanowires for FDTD simulations with periodic boundary conditions in x and y-direction and PML boundary in z-direction.

## 3.2 Resonant Optical Modes in Nanowires

It was seen in the last chapter that the resonant leaky waveguide modes in cylindrical waveguides are dependent on nanowire diameter only. It is understandably required to

decouple longitudinal resonances from the vertical nanowires arrays standing on a substrate. The presence of longitudinal modes complicates understanding of the nanowires and it was used in most of the cases presented in the studies earlier to this work. BY decoupling the effect, we are able to attribute every absorption peak to a physical phenomenon. To remove the effect of F-P resonances from the waveguiding properties of the nanowires, FDTD simulations were first performed on semi-infinitely long nanowires. 1 $\mu$m long nanowires with the perfect matching layer (PML) at the bottom of the nanowires were simulated. Transmittance was determined after 500 nm length to reduce any effects of spurious reflections that may occur even on a PML boundary.

### 3.2.1 Gallium Arsenide

The above-mentioned simulation analysis was done on GaAs semi-infinite nanowires to understand the nature of their modes. The real and imaginary part of the refractive index (n and k) of GaAs were extracted from Aspnes *et al* [73]. Figure 3.2 plots the absorptance spectra as the diameter is increased. For a specific diameter, it can be seen that an absorption peak is observed at resonant wavelength due to the excitation of $\mathrm{HE}_{11}$ modes. This absorption approaches unity at this wavelength and it shifts to longer wavelengths with the increase in diameter. For diameters of 150 nm and larger, a second peak appears at shorter wavelengths. At these diameters, the nanowires are multi-mode waveguides. This was confirmed by studying the electric field distributions indicating that the longer wavelength absorption peak corresponds to the excitation of the $HE_{11}$ mode and the second peak at lower wavelengths corresponds to the $HE_{12}$ mode. Some electric field distributions within the nanowires are shown in figure 3.2 for both resonance and off-resonance wavelengths (P1-P3). Clear excitation of $HE_{11}$ (P2) and $HE_{12}$ (P1) peaks are observed. At P3, the leaky modes exist with the little field within the nanowires. It

is resonant excitation of guided modes which leads to enhanced absorption within the nanowires. Further, as can be seen from the figures, fundamental $HE_{11}$ mode has a higher absorption than the higher order $HE_{12}$ mode.

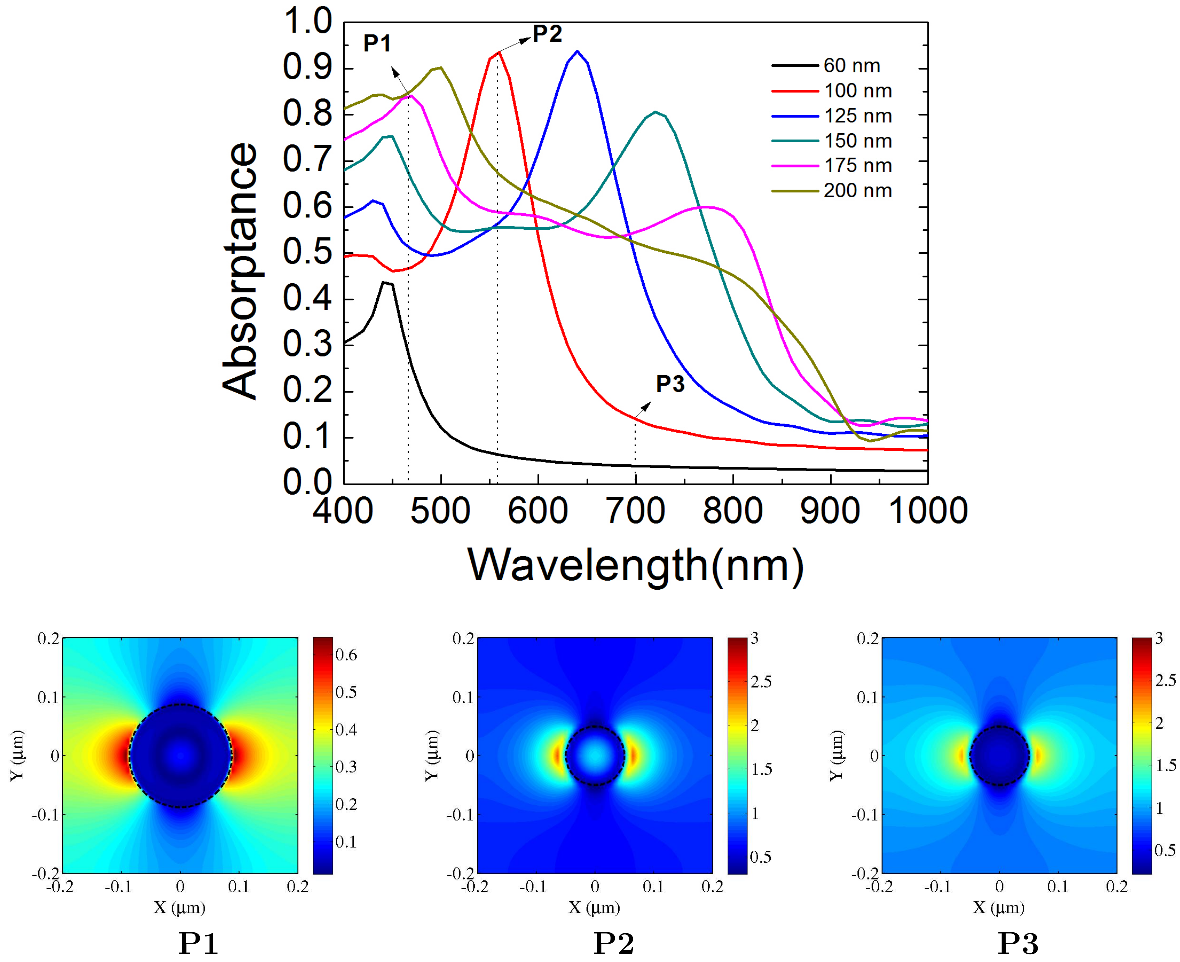


Figure 3.2: FDTD calculations of absorptance of semi-infinite nanowire for different diameters indicating $HE_{11}$ and $HE_{12}$ modes with power monitor placed at 450 nm into the nanowires.

For these simulations, the input electric field was polarized along the x-direction. The amplitudes for the distributions are normalized to the input. It was also confirmed that all six components ($E_x$, $E_y$, $E_z$, $H_x$, $H_y$, and $H_z$) of the electromagnetic field exist within

the nanowires showing that these are indeed hybrid modes of a cylindrical waveguide as shown in figure 3.3 and not transverse electric( TE) and transverse magnetic (TM) modes as was suggested previously [134].

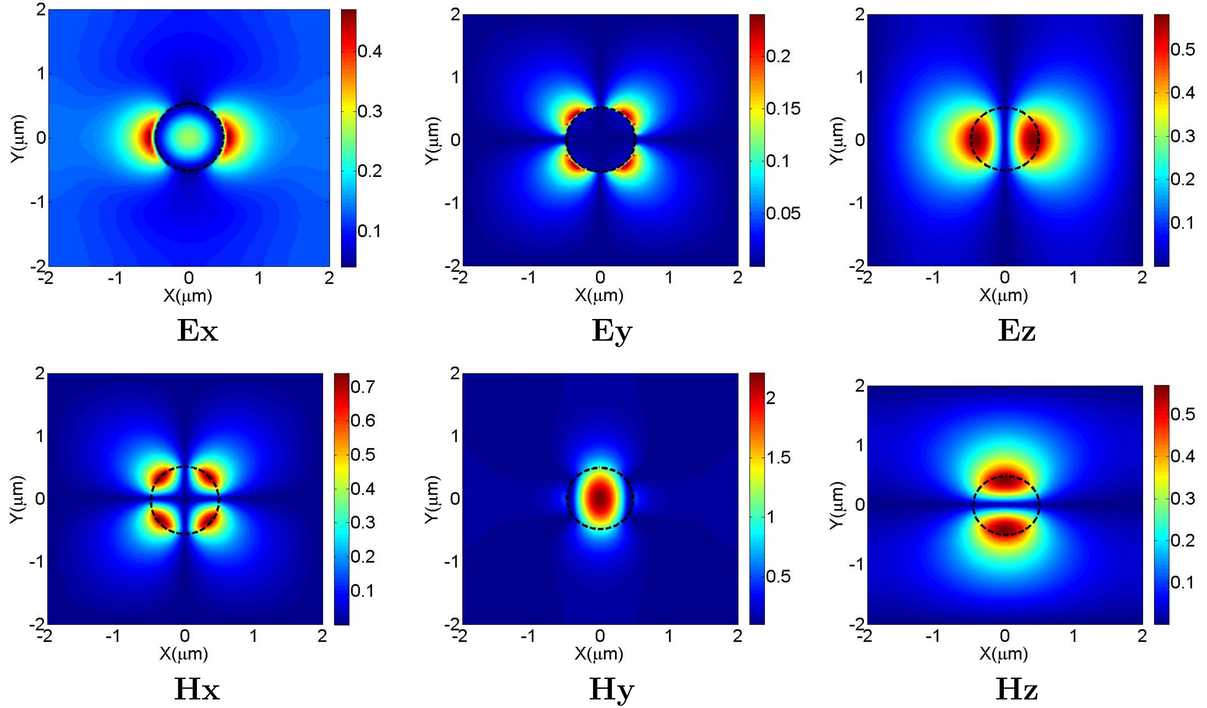


Figure 3.3: FDTD calculated six mode components $E_x$, $E_y$, $E_z$, $H_x$, $H_y$, and $H_z$ of EM field in semi-infinite nanowire for 100 nm diameter

For the 100 nm diameter nanowires, at the resonance wavelength of 560 nm, the peak intensity of the $H_y$ and $E_x$ fields increases by a factor of 9 and 2.4, respectively. In terms of the power density, the peak power density in the center of the nanowire increased by a factor of 1.6 as compared to the input intensities. Nanowires funnel the incident field at the resonant wavelength, thereby increasing absorption. The distributions clearly demonstrate that the input light is being coupled into either the $HE_{11}$ or $HE_{12}$ mode resonantly in the diameters studied. This increases the light interaction with the nanowire resulting in enhanced absorption for a wavelength band. As the nanowire diameter is

increased, the cylindrical waveguide can now support higher order modes. For the larger diameters, resonance excitation of the higher order $HE_{12}$ mode occurs resulting in a shorter wavelength resonance peak. The $HE_{11}$ peak has higher overall absorption as compared to the $HE_{12}$ mode due to higher mode confinement of the fundamental mode. The $HE_{11}$ peak is not observed for the 200 nm diameter as it has moved into the transparent region for the GaAs material resulting in lower overall absorption for the nanowires. This results in reduced absorption for this diameter and was confirmed experimentally as will be discussed in chapter 5. Figure 3.4 plots the resonance wavelength (absorption peak) as a function of diameter for the two different modes. The resonance wavelength shifts linearly with increase in diameter. For the fundamental $HE_{11}$ mode, the shift is ∼3.5 nm per 1 nm change in diameter while for the $HE_{12}$ mode, it is ∼1 nm per 1 nm change in diameter.

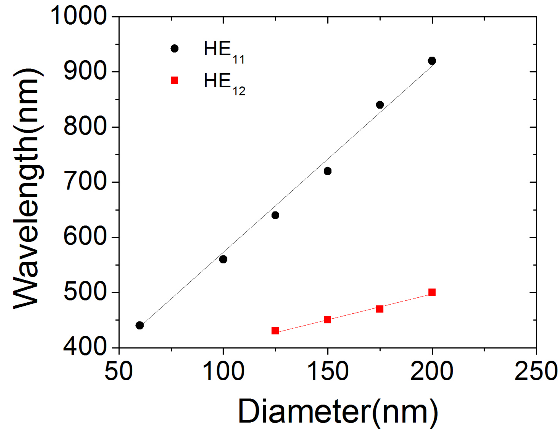


Figure 3.4: Excitation of $HE_{11}$ and $HE_{12}$ modes in GaAs nanowires as a function of wavelength and diameter.

### 3.2.2 Amorphous Silicon

Amorphous silicon is also a direct band gap and highly absorbing material. Its refractive is slightly different than GaAS though and thus we should expect that the phase

matching conditions for guided modes to be different than GaAs. Similar simulations were used to calculate resonance modes for semi-infinite a-Si nanowires. The n and k for a-Si were extracted experimentally for a thin film of known thickness using F-50 Filmetrics profilometer (Appendix A). It is due to the reason that the lab-grown a-Si was used to fabricate nanowires for measurements performed in Chapters 5 and 6. The absorptance spectra and resonant modes calculated using FDTD simulations are shown in figure 3.5. Similar behavior to GaAs is observed but larger diameters have more spectral features.

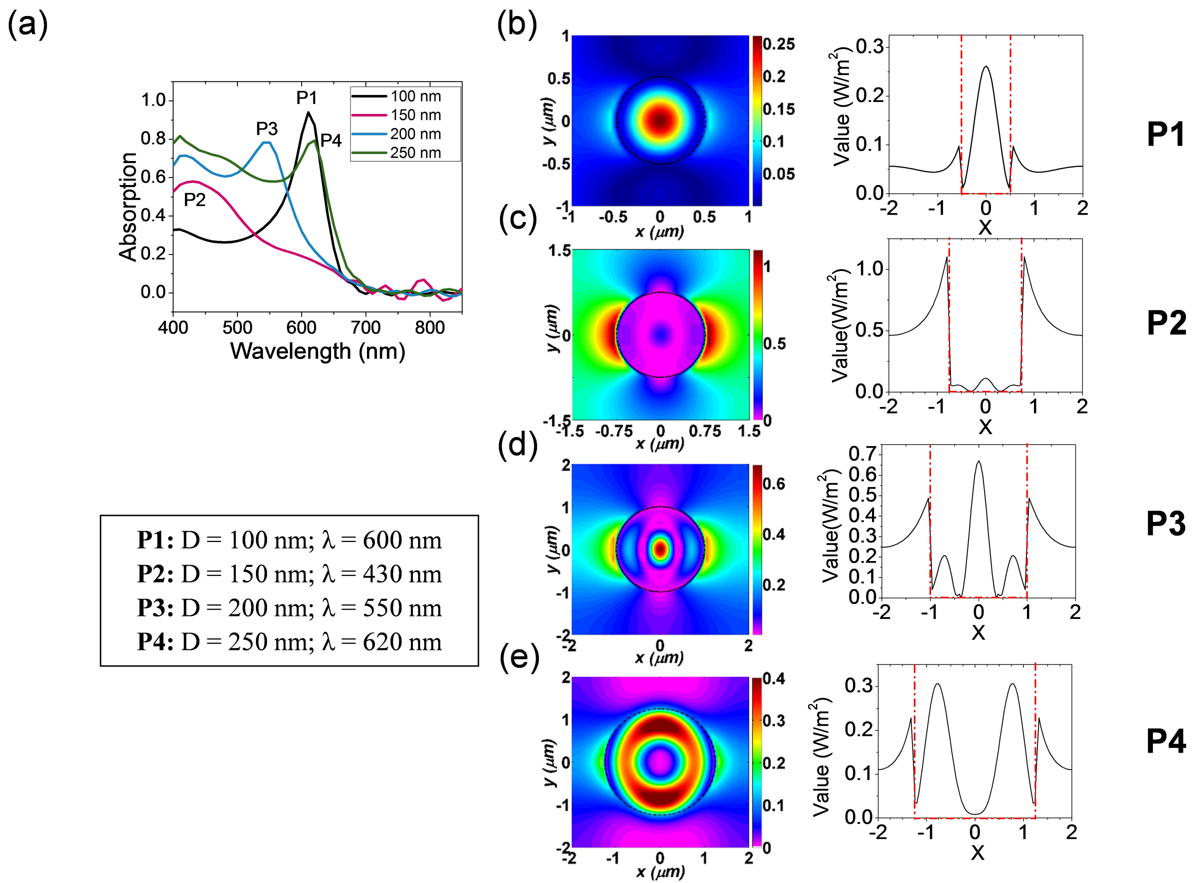


Figure 3.5: (a)FDTD simulations for semi-infinite aSi nanowires for diameters 100-250 nm. Peaks P1 to P4 corresponding to the dominant resonant wavelengths for each diameter are shown in the table below (b)-(e) The radial mode shape for the resonant peaks and the 2-D mode profiles at y=0.

For the four given diameters, the four wavelengths are chosen to be the investigated for radial mode profiles as we have discussed in the previous section. As shown in figure 3.5a, these four wavelengths are indicated as P1, P2, P3 and P4 and represent prominent absorption peaks for diameter from 100 nm to 250 nm. The wavelength of each peak and its corresponding diameters are also mentioned in the table shown in the figure. The 3-D irradiance profile and the corresponding 2-D plot of the modes along the x-axis and at y=0 are shown in Figure 3.5b-e. The irradiance plots clearly demonstrate resonant excitation of

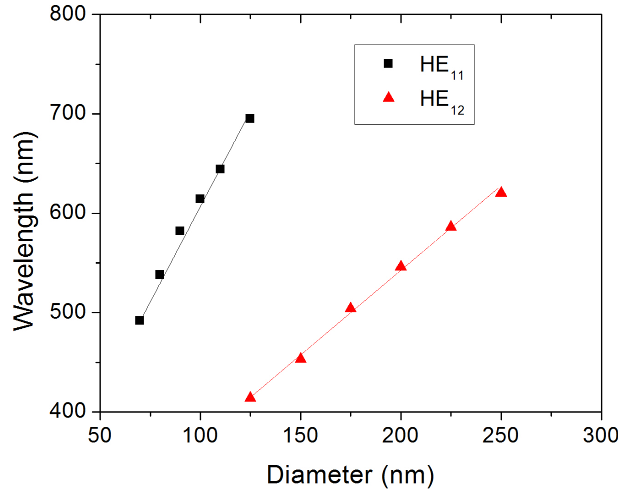


Figure 3.6: The excitation of $HE_{11}$ and $HE_{12}$ modes of a-Si nanowires as the function of diameter.

higher order modes at larger diameters. At smaller diameters, the lower order fundamental modes are being excited. Such as for 100 nm diameter, strongly excited $HE_{11}$ modes can be seen at 600 nm wavelength. For GaAs, it was excited at 560 nm. Interestingly, in this wavelength range the real part of the refractive index for a-Si is higher than GaAs. For 150 nm diameter, weakly excited $HE_{12}$ mode is getting excited at 430 nm (P2). Since at this wavelength the n and k are high for a-Si, it is expected that the higher order modes are also getting excited at this wavelength explaining the high absorption in this region

despite weak excitation of the mode. For 200 nm diameter, a strongly guided $HE_{12}$ mode is excited at P3. At a larger diameter 250 nm diameter, a higher order complex mode is excited at P4. As the diameter is increased, higher order modes are excited and even they red shift with the increase in diameter. The $HE_{11}$ modes shift to longer wavelengths at a rate of $\sim$ 4 nm per 1 nm change in diameter. When the $HE_{11}$ mode is excited it has very strong absorption. Once this resonance wavelength moves above the band gap, it stops playing a role in the absorption profile. As the diameter is increased, higher order modes are excited and even they red shift with the increase in diameter. The $HE_{12}$ mode shifts $\sim$ 1.7 nm per 1 nm change in diameter. The higher order modes have a lower absorption as compared to the fundamental mode at resonance.

### 3.2.3 Silicon

The absorption profile for semi-infinite silicon nanowires was also calculated using FDTD calculations. In figure 3.7 (b)and (c) the mode profiles for the nanowires are shown at four different wavelengths ranging from 400 nm to 752 nm marked as P1 to P4. The four different diameters were chosen from 60 nm to 200 nm to show the excitation of radial modes. As shown in other materials, the smaller diameters show the $HE_{11}$ modes only and with the increase in diameter the resonant modes shifts to higher wavelengths. P2 shows the $HE_{11}$ mode for 80 nm diameter (black) whereas P3 shown for 120 nm (red). Simultaneously, the higher order modes start to appear below 400 nm wavelengths fro 120 nm diameter (red). For 160 nm diameter, the intensity of $HE_{11}$ mode reduces drastically at P4 (blue), whereas the highly absorbing $HE_{12}$ mode appears at P1. For 200 nm diameter, the $HE_{12}$ mode appears at P2 (green), exactly where $HE_{11}$ mode appears for 80 nm but as seen from the mode profiles, the nature of modes are completely different. The mode profiles are clearly distinct from each other for each wavelength. The $HE_{11}$ and $HE_{12}$ modes

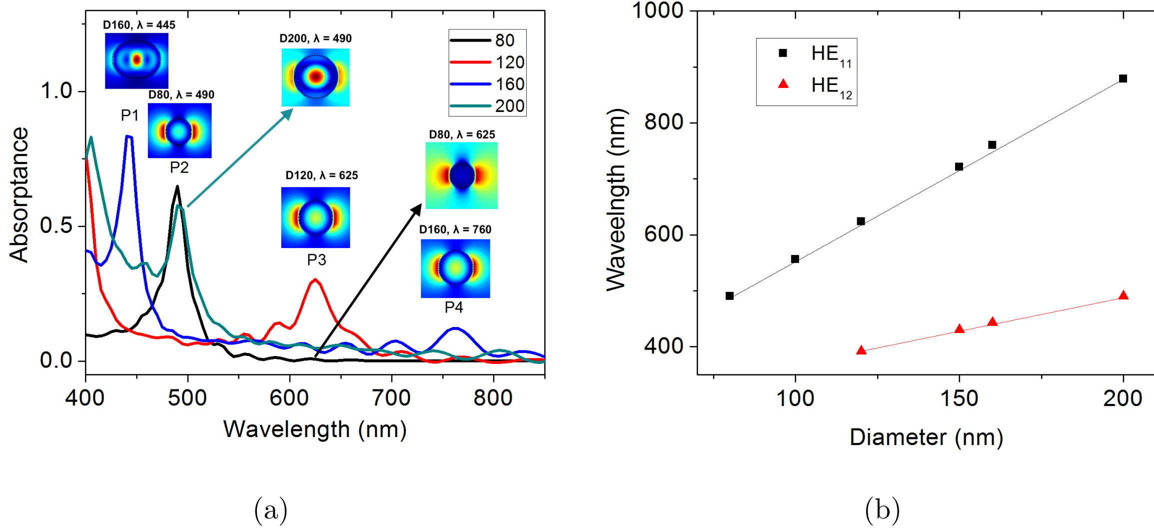


(a)

(b)

Figure 3.7: (a) Simulated absorption spectra for semi-infinite silicon nanowires for different diameter, showing the mode profiles at for wavelengths (P1-P4) (b) D vs $\lambda$ trends for the excitation of $HE_{11}$ and $HE_{12}$ modes.

calculated in figure 3.7a were plotted with the wavelength they are excited at to see the trends for the modes of both kinds and are shown in figure 3.7b. The rate of change in $HE_{11}$ mode per 1 nm change in diameter is $\sim$ 3 nm , whereas for $HE_{12}$ it is 1.2 nm.

### 3.2.4 Comparison of Resonant Peaks for Different Materials

The peak absorption wavelength for 100 nm diameter is 610 nm in a-Si while it was ~562 nm in GaAs nanowires. In silicon nanowires, the peak absorption wavelength for 100 nm diameter was previously demonstrated at ~570 nm too. This surprisingly correlates well to the real part of the refractive index of the materials used for these nanowires. The real part of the refractive index for GaAs and Si is 4.0187 and 4.0246 respectively while for a-Si is 4.2529 at their resonant peak wavelength. The peak absorption wavelength are similar for GaAs and Si which have similar real part of the refractive index while it is higher for

a-Si nanowires. The peak absorption wavelength seems to co-relate with the real part of the refractive index. Simulations show that the peak wavelength for 100 nm diameter InP nanowires, will be 528 nm. The real part of the refractive index for InP is 3.57 at 600 nm wavelength and lower than the semiconductors mentioned before. From another group′s work on InAs nanowires [21], the peak absorption wavelength was 580 nm and the real part of the refractive index is 3.7131 at its resonant peak wavelength. The variation in peak absorption wavelength for all these different materials is shown in Figure 3.8 and a decent linear fit is observed showing that the peak position in wavelength is highly co-related to the real part of the refractive index over different materials. Excitation of multiple higher order modes in a-Si nanowires is also due to the higher real part of the refractive index.

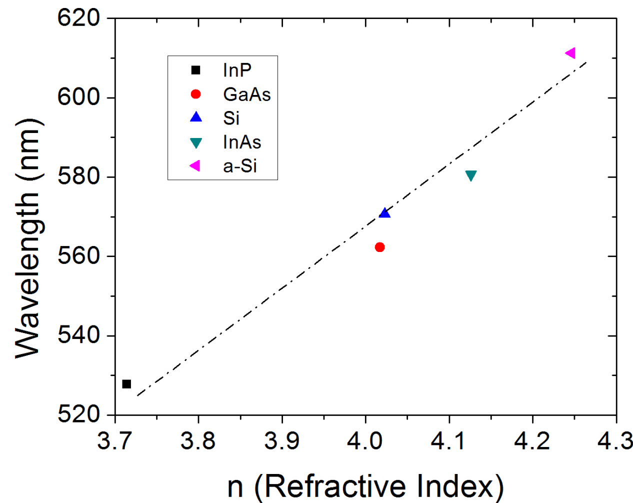


Figure 3.8: Resonant absorption peak vs refractive index for different semiconducting materials showing a linear relation between the n and resonant wavelengths.

## 3.3 Near Field Coupling between the Nanowires

### 3.3.1 Effect of k on Waveguide Coupling

It was discussed in the last section that the modal excitations in the nanowires are dependent on the real part of the refractive index and the diameter of the nanowire. However, as mentioned in the last chapter, near-field coupling affects the resonant conditions of the adjacent waveguides. The negative or positive values of Rayleigh Identity($\zeta_\circ$) correspond to the destructive or constructive interference between the fields for the adjacent nanowires respectively. This leads to the blue or red shift in the resonant mode to increase or decrease the mode confinement. These conditions are needed to be verified for nanowires to have a better understanding of their optical properties. Fountain *et al* [22] verified it for silicon nanowires in a simulation study where they showed that the mode confinement increases and the resonant wavelength blue shifts as the pitch in the arrays are decreased for 250 nm to 150 nm. Above 250 nm pitch, nanowires act like individual waveguides.

This phenomenon, however, needs to be extended to a broad range of materials as well as pitches to establish the comprehensive picture of nanowires coupling. It is well known that the complex refractive index of a material is defined as n - jk, where n indicates the phase velocity and k indicate the extinction coefficient of the material. The simulation studies of nanowires involve real (n) and imaginary (k) part of the refractive index along the with material dimensions to replicate the measured spectra of the nanowires. This has been established in the previous studies and will be shown in the next chapters as well. As we have seen in the previous section that waveguiding conditions mainly result out of n of the nanowires and k is responsible for the absorption in the nanowires. As a mode gets excited at a certain n, that specific confinement wavelength is absorbed within the material due to the presence of k. If the k is small, then the under the right F-P conditions

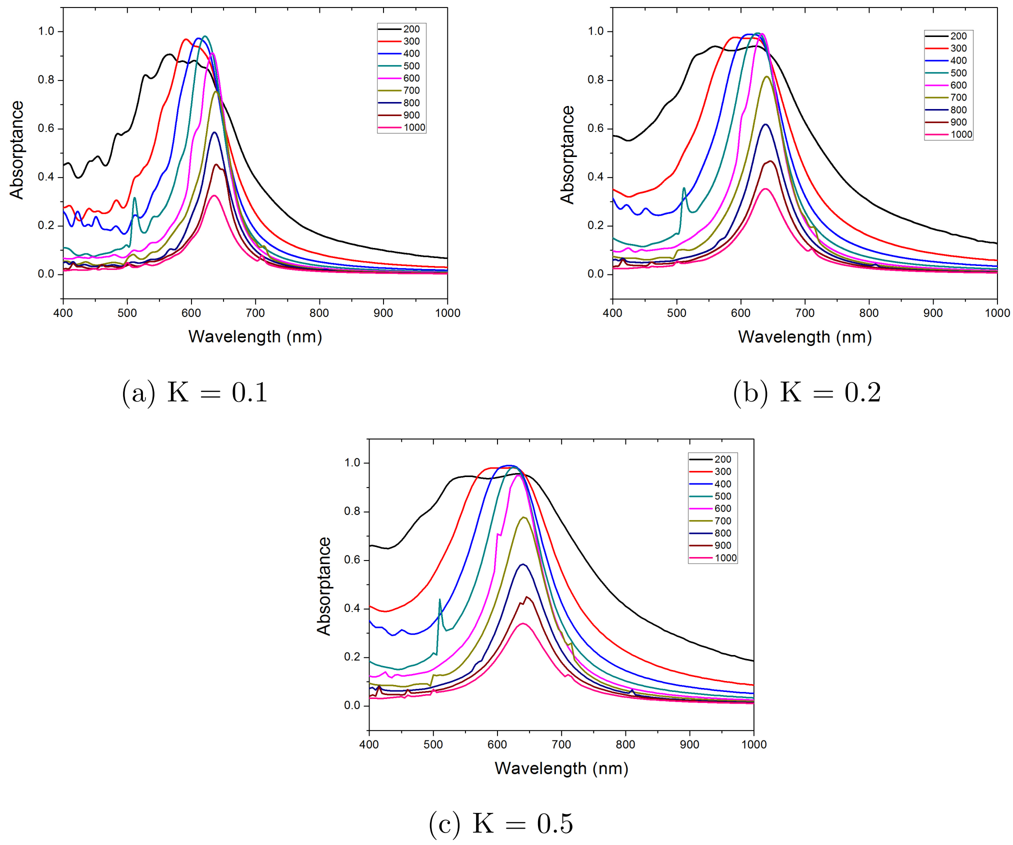


(a) K = 0.1

(b) K = 0.2

(c) K = 0.5

Figure 3.9: The absorption in a-Si nanowires with different values of k and pitches.

the light bounces back and forth inside the nanowires before it gets fully absorbed. and may get coupled across different nanowires.

To test this hypothesis, we performed FDTD simulations on nanowires with constant n and changing k. The purpose of these calculations was to see whether k played a role in changing the coupling conditions of the nanowires. Figure 3.9 shows the absorption peaks in the nanowires for different values of k for hypothetical nanowires which use the values of n for a-Si across the wavelength region. The diameter chosen for these simulations is 100 nm, which shows a strong resonant peak in the measured wavelength region. As shown

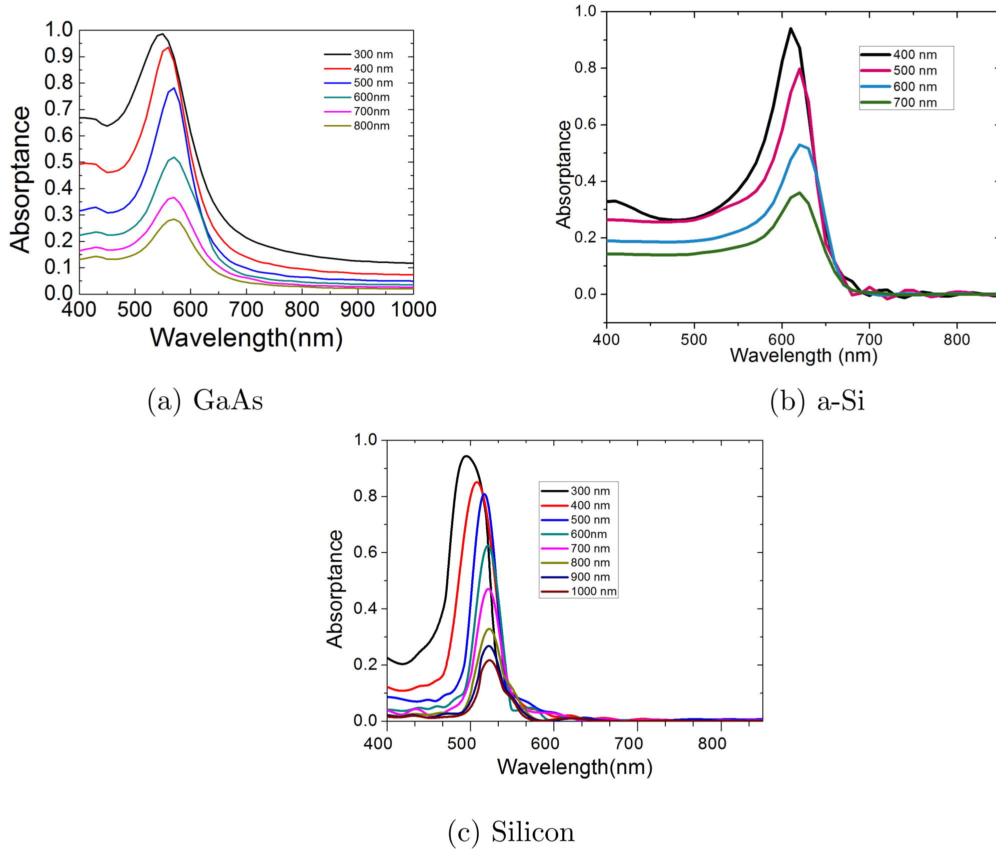


(a) GaAs

(b) a-Si

(c) Silicon

Figure 3.10: The absorption peaks calculated in semi-infinite (a) GaAs (b) a-Si (c) Silicon nanowires with different pitches and 100 nm diameter.

in figure 3.9a, the resonant peak shifts visibly for K = 0.1 for the pitches up to 600 nm

and then there is no noticeable shift for the larger pitches. For K = 0.2 in figure 3.9b, the shift in insignificant except for initial two pitches. The peaks at resonant wavelength are almost coinciding for pitches from 400 nm to 1000 nm. For K=0.3, the effect completely vanishes as shown in figure 3.9c. Thus, the simulations predict that when the k is low, the nanowires get coupled and the resonant wavelengths shifts to the blue side, showing destructive interference ($\zeta_{\circ} < 0$)and a further increase in absorption. When k increases the coupling between nanowires doesn't happen and they act almost like individual waveguides. For larger pitches, the discontinuities at off-resonance wavelength are due to the diffraction orders of the nanowire gratings [23].

Extending this theory to real materials i.e. Silicon, a-Si and GaAs have different k values and thus will present different behavior. We performed FDTD simulations for semi-infinite nanowires for the three materials as shown in figure 3.10. As we would expect, for the same diameter (100 nm), the three different materials are exciting resonant modes at three different diameters. Also, GaAs and a-Si nanowires are showing negligible near field coupling as opposed to Silicon nanowires where the resonance shift is quite significant for pitches 300-500 nm. This could be explained by looking at the k of these materials in this range. For GaAs, the resonant mode is exciting roughly at 575 nm and at this wavelength its k is 0.26069, which would mean there would be no or negligible coupling between the nanowires at this wavelength. For a-Si, the resonant wavelength is $\sim$ 600 nm for 100 nm diameter and the value of k is 0.124. Whereas, the value of k for silicon is 0.05 around resonant wavelengths and one expects the coupling between the nanowires at this value of k.

| Material | $\lambda_{res}$ | k($\lambda_{res}$) | Coupling |
|---|---|---|---|
| GaAs | 575 | 0.2609 | No |
| a-Si | 620 | 0.124 | No |
| Si | 490-525 | 0.078279 - 0.055520 | Yes |

Table 3.1: The resonance wavelengths and their corresponding refractive indices for GaAS, a-Si and Silicon nanowires indicating whether the nanowires are coupling depending on the value of their k.

## 3.4 Longitudinal Modes in Nanowires

The F-P resonance mode discussions in chapter 2 show that to excite the longitudinal modes in nanowires we require reflecting interfaces at both their ends and k small enough to let the light bounce back and forth before it is complete absorbed. Vertical nanowire arrays naturally provide reflecting interfaces at the top and bottom interface due to the impedance mismatch between air-nanowire and nanowire-substrate interfaces. Additionally, for distinct F-P features, we also require the wavelength regions where the diameter dependent leaky modes do not interfere with them. In the following simulations, the substrate is added at the bottom interface of the nanowires to observe the F-P resonances inside them. Figure 3.11 shows simulated absorptions for a-Si nanowires of different diameters with the substrate at the bottom. Comparing them with the semi-infinite nanowires in figures 3.2 and 3.5, the radial modal locations remain at the same position even after keeping the substrate at the bottom. This is because the nanowires are highly absorbing at this wavelength and most of the incident light is absorbed within the first pass. However, there are additional absorption peaks at the longer wavelengths excited periodically every $\sim$40 nm. These peaks arise due to the reflections at the top and bottom interface of the nanowires in the region where the k is low for both the materials.

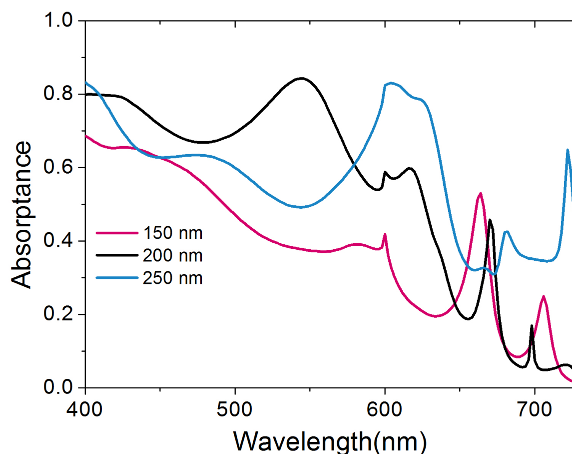


(a) a-Si

Figure 3.11: Simulated absorption aSi nanowires with substrate at the bottom. The length of nanowires is 500 nm.

## 3.5 Length Analysis of Nanowires

Due to the high refractive index contrast between the semiconductor and the surrounding air in an array, one would expect the scattering of light to be also present and in fact, earlier studies assumed that the high absorption observed was due to the recapture of the scattered light by the nanowires [74]. It is interesting to understand at what length the nanowires behave strongly as optical waveguides where the optical mode properties dominate the scattering. To our knowledge, no such study has been done though highly enhanced Raman scattering was observed in silicon nanowires only 230 nm tall due to radial and longitudinal modes [75]. In this section, a systematic simulation study by comparing nanowires of different lengths is conducted. Again, to understand the role that the radial optical mode plays in absorption characteristics of the nanowires for different lengths, the nanowires were first considered to be semi-infinitely long and transmission through different lengths of nanowires simulated. By considering the nanowires to be

semi-infinitely long, the effect of reflections at the nanowire-substrate boundary is removed and thus, no longitudinal modes exist. Transmission spectrum was calculated at different lengths for wavelengths from 400 nm to 800 nm and is plotted in figure 3.12. The resonance wavelength for the $HE_{11}$ mode is seen as a minimum in the transmission spectra as the absorption increases at this wavelength. As can be seen in the figure, the absorption peak is even present at a length of 5 nm and the strength of the minima increases with length. Thus, optical modes are excited right at the air-nanowire interface. Also, it is observed that the peak slightly shifts in wavelength to the shorter wavelengths as the length is increased and then stabilizes after a certain length once the optical mode dominates.

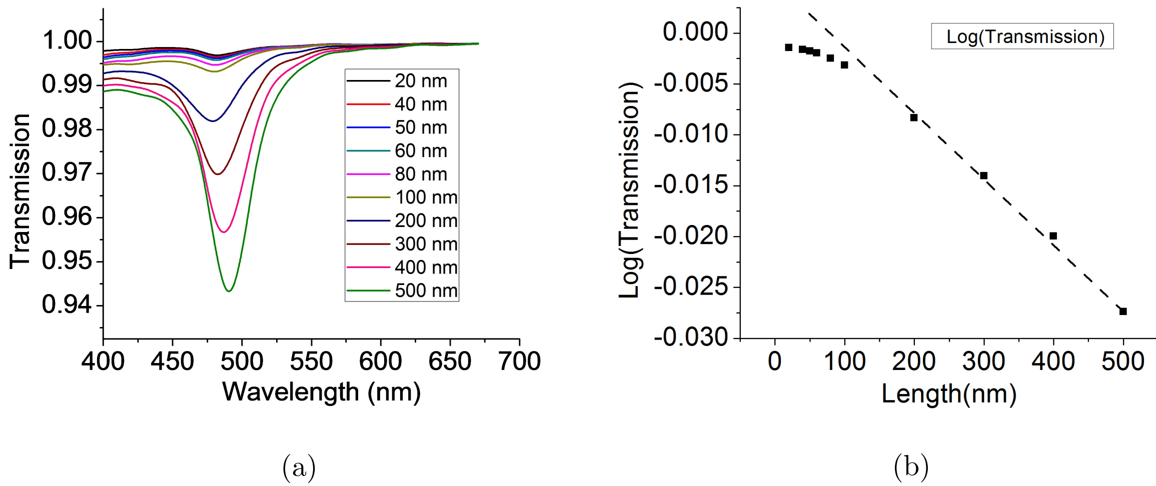


Figure 3.12: (a) Transmission of power through semi-infinite silicon nanowires calculated using FDTD till the length of 500 nm. (b) Logarithm value of the transmitted power plotted with the length of the nanowire along which the power transmits.

In order to understand where the optical mode starts to dominate, the transmission values at the resonant wavelength of 500 nm are plotted on a logarithmic scale with respect to the length of the nanowire in figure 3.13b. When the mode excitation dominates the optical characteristics of the nanowires, then the log(Transmission) should vary linearly

with the length according to Beer-Lambert law (T= $e^{-\tau}$). As can be seen from the figure, above 150 nm length, the transmission is a linear function of length on the logarithmic scale (exponential in the real scale). However, for lengths smaller than 100 nm, a roll-off is observed. This suggests that scattered light, i.e. light, which is not coupled into the nanowires, is a dominant component for lengths smaller than 100 nm and the resonant radial modes are not yet fully developed within the nanowires. The value of the scattered light should be smaller than 2%. Contrary to popular thinking by many researchers, vertical nanowires do not scatter light appreciably. Even for nanowires 150 nm long, the modal absorption dominates the scattered light and the nanowires can be treated as optical waveguides, which are being resonantly excited. To further establish these results, the same simulations were performed on GaAs nanowires as well as shown in figure 3.13. The transmission values in figure 3.13a show the absorption in the nanowires much higher than the silicon nanowires shown in figure 3.13a. The transmission value of GaAs nanowires was plotted on a logarithmic scale along with silicon nanowires in figure 3.12b. Even for GaAs nanowires, somewhere below 150 nm length the transmission is a linear function of length on the logarithmic scale. Being highly absorbing, the GaAs nanowires show much higher slope for the transmitted mode at the logarithmic scale ($\sim 50\times$) but it does not affect the length where the nanowires start to strongly guide the mode. These studies were experimentally verified for silicon nanowires as well, which will be discussed in the next chapter.

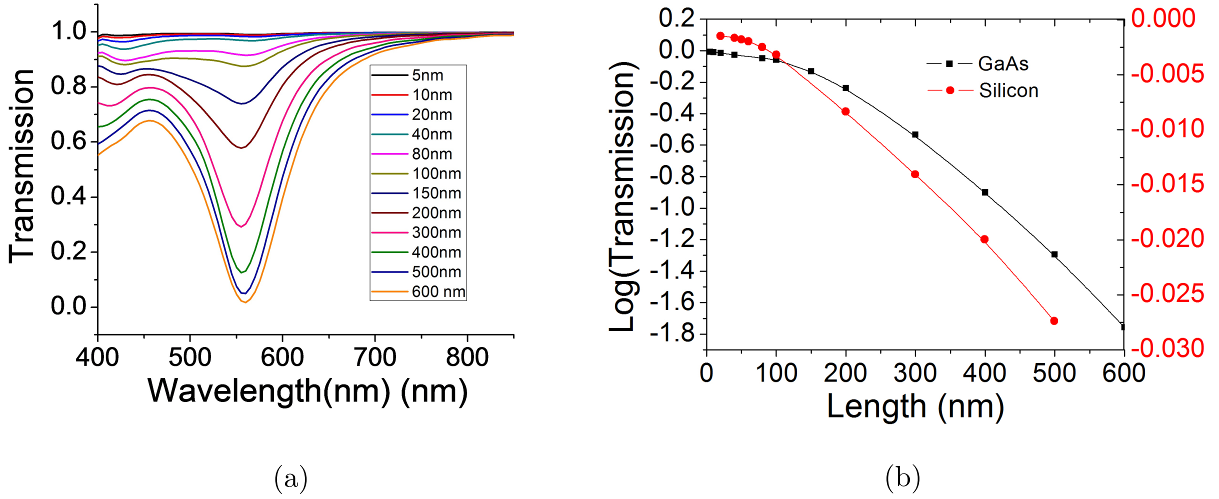


(a) (b)

Figure 3.13: (a) Transmission of power through GaAs nanowires for diameter 100 nm calculated using FDTD simulations (b) Comparison of logarithmic value of power as a function of nanowire length along which the power transfers

## 3.6 Shape Effect in Nanowires

We use FDTD simulations to compare the absorption characteristics of vertical silicon nanowires with square and cylindrical cross-sections and observe unintuitive behavior. As we have seen in earlier sections that the absorption peaks are attributed to the resonant excitation of transverse optical modes. Since the optical modes depend on the cross-shape, one would expect the absorption would vary if the shape of the nanowires is changed. However, there have been only very sporadic studies which have been carried out for nanowires other than cylindrical cross-sections. In a theoretical work, it was shown that the absorption becomes more broadband in elliptical nanowires as compared to cylindrical nanowires [76]. This was due to the breaking in the degeneracy of the optical modes and the ordinary and extraordinary modes being resonantly excited at slightly different wavelengths. Park *et al* [77] used elliptical nanowires to design polarization resolved pho-

todetectors. They further demonstrated reconfigurable imaging systems using elliptical nanowires [78]. Here we compare symmetrical shapes consisting of the circular and square cross-section of the nanowires using FDTD simulations. The very first step is to compare the electric field distribution inside both the cross-sections. Initially, the diameter(d) and radius(r) of the respective circular and square cross-section were chosen to be equal for the comparison. FDTD simulations were performed for semi-infinite structures with monitors 500 nm along the length of the nanowires. Figure 3.14 shows the contour plots of the radial fields excited in both the structures. Interestingly, for a=d the mode confinement does not match very well. However, when the fields are compared for diameter having same areas as square cross section the field confinement increases indicating the resonant wavelength being dependent on the area of cross section. Although the confinements of $HE_{11}$ modes match well for same cross-section areas but as seen in figures 3.14a and 3.14c, the mode shapes are not the same.

In the next step, nanowires of both cross-sections having the same area were simulated to calculate absorption for the wavelength range of 300 nm to 900 nm. The silicon substrate was inserted at the bottom for the practical context. Figure 3.15 shows the absorptions plots of the square and circular nanowires as the dimensions increase. Overall, these contour plots are more or less similar except for some fine differences. There are hot spots from 400 to 700 nm wavelengths for both shapes at smaller areas. These are due to the $HE_{11}$ modal excitations. The general trend of these absorption peaks is almost the same except that for the circular cross-sections the absorption seems slightly broadband for each hot spot. Moreover, around 300 nm wavelengths, square nanowires show slightly less absorption compared to circular nanowires across all area ranges. Thus, despite having different mode shapes, both the nanowire shapes show similar optical response over a wide range of wavelengths and diameters.

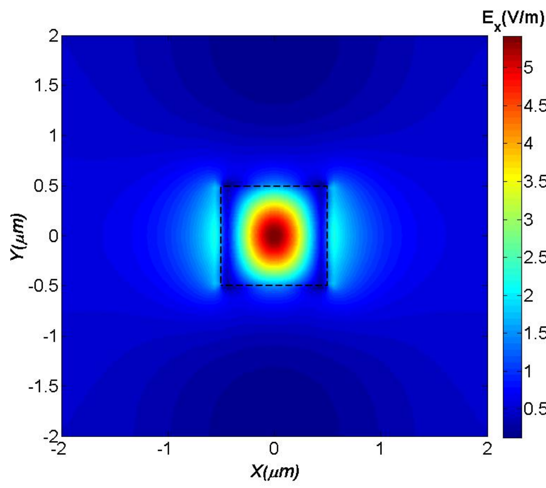


(a) Square - 100 nm

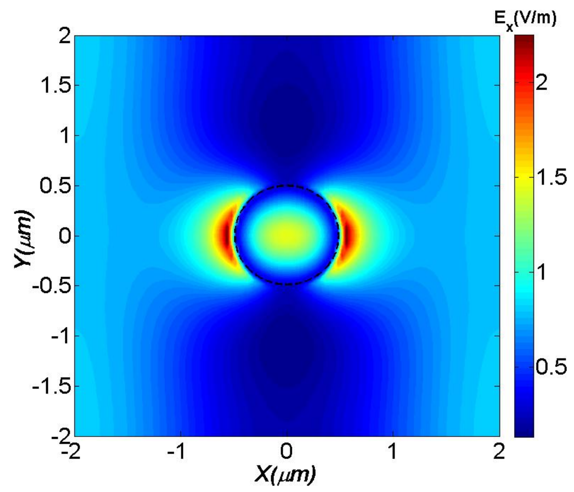


(b) Circle - 100 nm

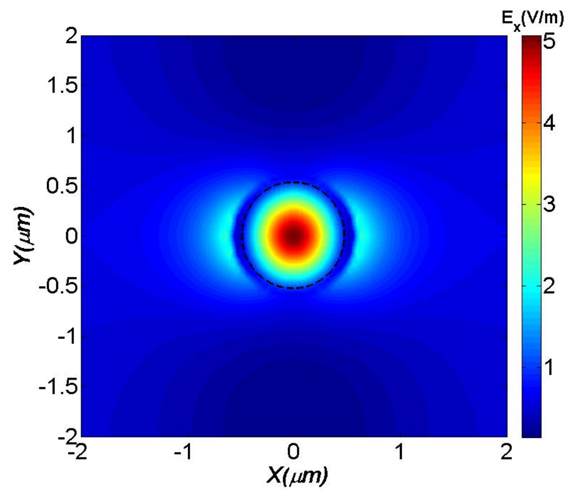


(c) Circle - 113 nm

Figure 3.14: Calculated electric field distributions for semi-infinite nanowires for (a) Square (b) Circular cross-sections having 100 nm diameter(c) Field distribution for circular cross-section having 113 nm diameter, thus having the same area of cross section as the square with 100 nm side.

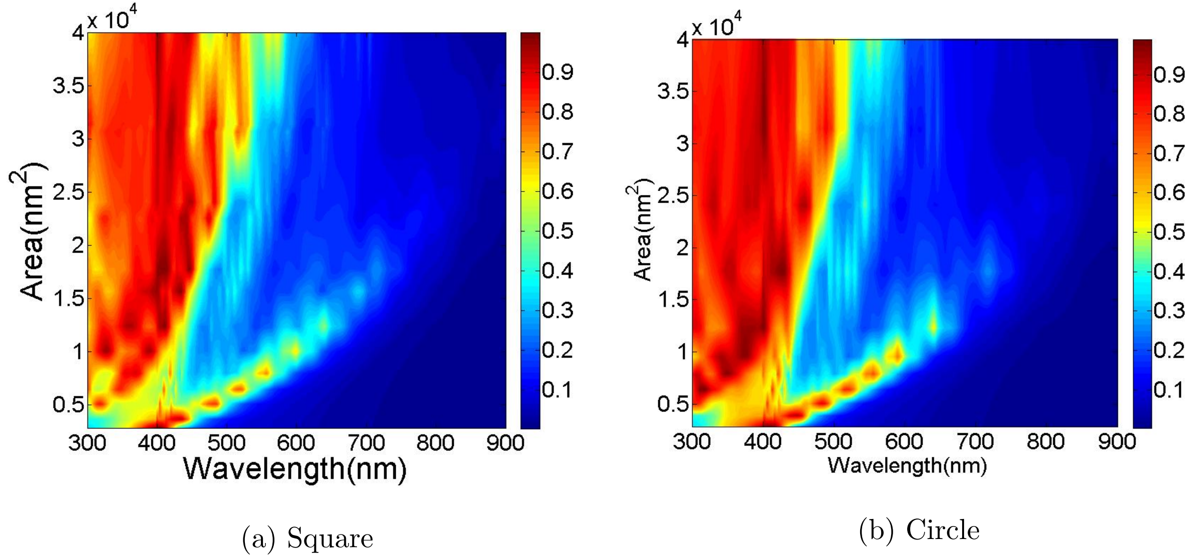


(a) Square

(b) Circle

Figure 3.15: Calculated absorption contour plots for nanowires for (a) Square (b) Circular cross-section . The length is 1 $\mu$m for all the nanowires.

Further, another diameter was chosen to establish the argument that modal behavior is different for both the nanowires. Figure 3.16 shows the mode profiles of nanowires of both the cross-sections for an area having square side 200 nm and diameter 226 nm respectively. The wavelength chosen was 516 nm wavelength, as nanowires were showing distinct absorption peaks at this wavelength for their respective diameters.

The mode profiles clearly differ from each other in their shape and represent higher order modes. Thus, despite having distinct modal excitations between square and circular cross-sections, these nanowires show strikingly similar absorption response showing the optical response of nanowires in this regime to be independent of the nature of geometry of the nanowires. This study has a potential to be extended to other cross-sections related to the crystal growth or etching of the nanowires as it could potentially give a generalized area dependent optical response of the nanowires for applications in photonics. This study could eliminate the need for shape specificity in nanowires based applications.

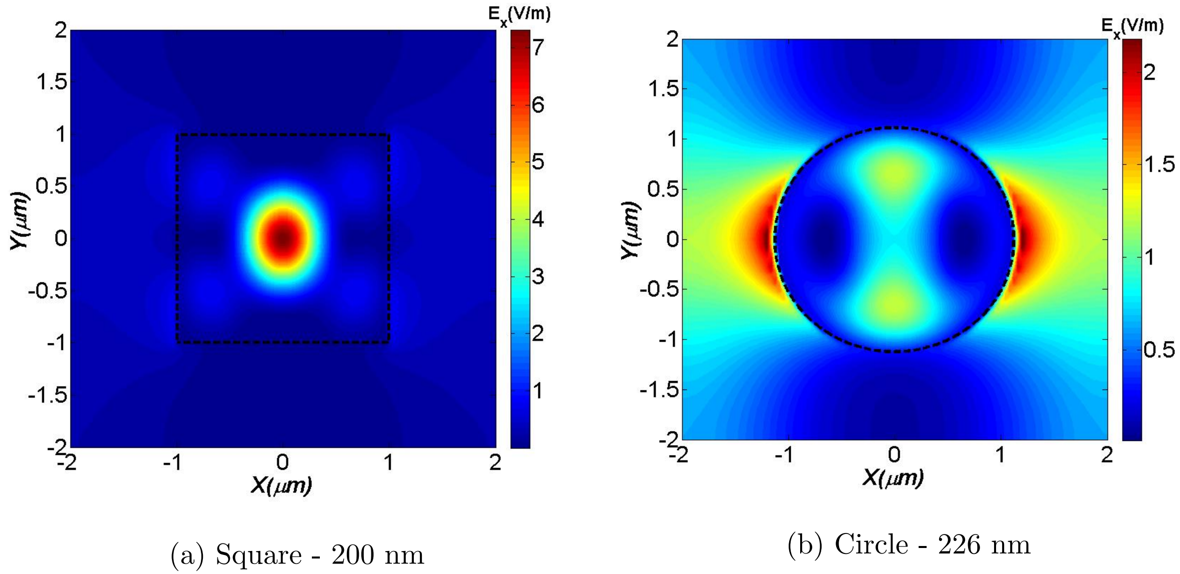


(a) Square - 200 nm

(b) Circle - 226 nm

Figure 3.16: Calculated electric field distributions for semi-infinite nanowires for (a) Square having 200 nm side and (b) Circular cross-sections having 226 nm diameter. Both cross-sections represent almost the same area.

## 3.7 Conclusion

The simulation studies of semiconductor nanowires were performed in this chapter predicting their waveguiding properties. It is shown that how the nanowires absorb incoming wavelengths by exciting cylindrical modes depending on their diameters. Also, the optical properties were understood for nanowires when the diameters, pitch, length and shape were varied. The dependence of the optical response on the real and imaginary part of refractive index was highly emphasized. With this, the theoretical models for generalized properties of semiconductor nanowires were established and verified using the properties of the materials that will be used in the next sections. From this chapter we see:

- Resonant modes are excited in the nanowires at wavelengths that depend on the diameter of the nanowires.

- The resonant wavelengths are also dependent on the real part of the refractive index (n), as the resonant wavelengths increase with the increase in n.
- For the low loss nanowires near field coupling is observed. The coupling was observed for silicon nanowires for which the imaginary part of the refractive index is low. a-Si and GaAs nanowires show no coupling as they have higher k.
- The periodically arranged nanowires act like coupled oscillators where n is equivalent to the spring constant and k is equivalent to the damping constant.
- Resonance exists due to the excitation of $HE_{1m}$ modes.
- F-P modes can further increase absorption where nanowires absorption is low.
- Nanowires only need to be 150 nm long for them to be described as waveguides.
- Scattering is low in these arrays.
- For symmetrical nanowires, the absorption features are very similar for the same area of the cross-section. However, their mode shapes differ from each other. Many of these observations brought new knowledge to the field.

# Chapter 4

# Nanowires Fabrication

In this chapter, different methods developed for etching nanowires in different semiconductors are described. We are mainly interested in nanowires arrays in silicon, a-Si, GaAs and GaN. The optical properties of nanowires are affected by their physical characteristics. The length, diameter, lattice arrangement, and alignment control their absorption and emission dynamics and so do the doping concentration, composition, crystal structure, direction and cross-section (for waveguiding). Thus control over these different characteristics is needed. As shown in next chapter, ordered nanowire arrays provide attractive waveguiding properties which we are interested in harnessing. There are two methods used for nanowire arrays: bottoms-up approach and top-down approach. Bottom-up methods involve the growth of nanowires while top-down approach involves etching the nanowires into a substrate. The different approaches are discussed in the next sections along with my experimental results.

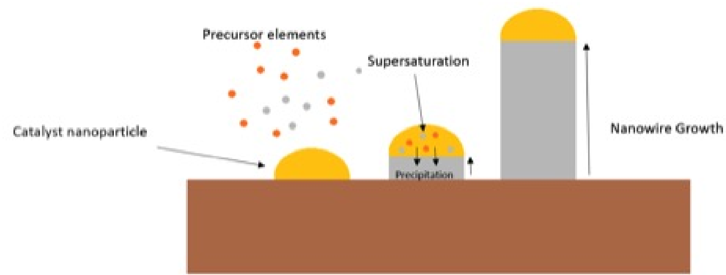


Figure 4.1: Vapour Liquid Solid bottom-up approach to grow a single nanowire

## 4.1 Bottom-Up Approach

Bottom-up growth is the cheap and popular method of yielding high volume of nanowires. The most common mechanism for bottom up growth is putting a metal seed on a semiconductor surface at high temperature (∼500°C-1000°C) and supply precursors for the intended material to grow nanowires at a controlled pressure. The metals that are usually used for the growth are Au, Pt, Al, Mn, Ni, Ag and Cu [79–88]. Bottom-up approach has been used for growth of different semiconductor nanowires including silicon, gallium-arsenide, indium phosphide, gallium phosphide, gallium arsenide phosphide etc. For the nanowires of interest to us, some of the relevant work is described below.

### 4.1.1 Silicon Nanowires

Silicon nanowires were the first of their kind to be demonstrated using vapor liquid solid (VLS) growth introduced by Wagner and Ellis [79] in 1964. These nanowires were grown using a metal catalyst-assisted growth of unidirectional whiskers at high temperatures. A schematic of the growth process is shown in Figure 4.1. In his process, metal nano-particles or nano-droplets are deposited on the substrate using various chemical and physical depo-

sition techniques. The growth process is initiated by the formation of liquid alloys by metal droplets and vapors of precursor elements. When the vapor concentration surpasses the equilibrium concentration (most probably due to vapor pressure fluctuations) to achieve the minimum free energy, the alloy gets supersaturated and the vapor components precipitate at the liquid-solid boundary resulting in the formation of nanowires. The growth continues as long as the vapor components are supplied. The radial growth is confined to the size of the metal catalyst [89]. Silicon nanowires are grown using Au catalyst and a gaseous precursor such as silane as a silicon source. Au-Si alloy has a drastically reduced melting point than the individual components. Gaseous silicon precursor, when exposed to the alloy droplets, is cracked at the silicon surface. Silicon after saturation point in Au-Si alloy droplet starts to precipitate at the droplet-wire interface and continues to grow as long as the silane supply and high-temperature persists [83].

A mechanism similar to VLS is Vapour-Solid-Solid (VSS) growth, where the solid catalyst is used instead of the liquid droplets. In this case, the melting point is reduced due to catalyst supersaturation, which means VLS growth can continue below eutectic temperature and the alloy particle solidifies if the supersaturation is not maintained [82].

Another derivative of VLS growth is the Solid-Liquid-Solid mechanism in which a thin layer of gold was deposited on the silicon substrate and was annealed in the quartz tube at 1000°C to transfer them into the liquid phase. Then the rapid cooling at the interface using nitrogen supply renders silicon atoms to self-assemble into wires [90]. In another variation, the precursor was decomposed in a high boiling solvent in the presence of catalyst nano-crystals [91]. Molecular Beam Epitaxy (MBE) has also been used as another clean, oxidation-free process of providing precursors in ultra-high vacuum $1e-10$ mbar range [85, 86, 88].

Ultra-narrow nanowires have been demonstrated using laser ablation to prepare sub-10

nm diameter catalyst clusters. In this, a pulsed laser targets the precursors and catalyst in a quartz tube. The diameter can be achieved as low as 3 nm through this process [83, 92].

### 4.1.2 Gallium Arsenide Nanowires

For GaAs Nanowire growth VLS is initiated in various systems like Metal Organic Vapor Phase Epitaxy (MOVPE) where trimethylgallium (TMG) and tertiarybutylarsine (TBA) are used as precursors for Ga and As respectively with Ga:As ratio of 1:25 [93]. In Molecular Beam Epitaxy (MBE) the GaAs substrate is thoroughly cleaned and transferred to the chamber. An effusion cell supplies gallium and $As_2$ is supplied by a gas cracker, operating at high temperature and extremely low pressure to achieve minimum mean free path and high yield [85, 86, 88].

Chemical Beam Epitaxy (CBE) is different from MBE as the precursor for Gallium decomposes on the substrate surface inside the chamber and the one for Arsenic gets decomposed to $AS_2$ outside the chamber. The pressure in CBE is also four to five orders lower than MBE process [94].

### 4.1.3 Gallium Nitride Nanowires

VLS growth can also be employed for the fabrication of GaN nanowire growth. In one study [95], molten gallium (99.9999% pure), and several iron, nickel, and cobalt based alloys were used in the quartz tube at 800 - 1050°C and purged with ammonia gas to achieve high-density GaN nanowires having wurtzite crystal structure. In another experiment [96], laser-assisted catalytic growth was used to grow GaN nanowires using Fe as a catalyst, and Ga and N vapors as the catalysts at 900°C. Fe is the desired catalyst in this process as it can dissolve both Ga and N but does not form more stable solid phase than GaN.

There are other unconventional methods to grow GaN nanowires such as in one study [97], instead of using metal catalyst, carbon nanotubes were used to confine the growth process using $Ga_2O$ and $NH_3$ as precursors.

## 4.2 Drawbacks of Bottoms-up Approach

Although the bottom-up growth of nanowires has demonstrated numerous possibilities of exploring flexibility in size, shape, yield and type of material, still it has its own limitations when trying to explore its end products for applications. One limitation is as a result of contact between metal and semiconductor in the form of the liquid alloy at high temperature, the nanowires get contaminated as a result of diffusion of metal during the growth process. It alters the optical properties and impurity level in the band gap of the nanowires. Another drawback is due to the lack of control while inducing crystal growth; it is hard to achieve consistency in controlled array arrangement, crystal orientation, controlled cross-section and consistent vertical alignment and repeatability. Removing metallic masks after the growth is also an issue under consideration as a requirement for various applications. Further, heterojunctions (e.g. a quantum well in a wire) are difficult to achieve in this method.

The above-mentioned issues with nanowire growth have led to the search for new methods of achieving the same morphology. The top-down approach is an alternative way of achieving nanowire structures by etching down the semiconducting material from the macroscopic wafer scale.

## 4.3 Top-Down Approach

The top-down approach brings in a different concept and scope in the production of semiconductor nanowires. Due to some unresolved drawbacks in nanowire growth techniques, more and more attention is being given to the etching methods of nanowires. It gives a much better control over the size, shape, composition, crystal orientation, aspect ratio, arrangement and repeatability in the production of nanowires. The surface is patterned with the mask and nanowires are etched into the substrate. There are different approaches to etch the semiconducting surfaces.

### 4.3.1 Catalytic Chemical Etching

In this method metal particles are deposited on the semiconductor wafer by a wet deposition method, then the wafers are immersed and left to dissolution into the etching solution such as HF or $AgNO_3$ for silicon. The silicon in contact with catalyst clusters/particles is etched off as the metal catalysis the etching process in the presence of etchant [98, 99]. Moreover, the single crystal nanowires with desired orientation can be created by choosing the desired crystal orientation of the wafer. Although this method gives control over crystal orientation and sidewalls smoothness to some extent, but it still lacks the control over shape, diameter, uniformity and consistency.

### 4.3.2 Reactive Ion Etching

Reactive Ion Etching (RIE) is an anisotropic etching method to get highly precise morphologies of nanostructures with great control on sidewall smoothness, diameter, length, and shape while achieving high aspect ratio and preserving axial heterostructures, doping and crystal orientation of the bulk. However, reactive ion etching alone cannot achieve

all these features, it has to be accompanied with inductive coupled plasma (ICP) on a wafer covered with hard masks patterned with the help of optical or electron beam lithography. Photoresist, $SiO_2$ particles and polystyrene (PS) beads have also been used as mask [100–102]. Photoresists, however, act as a poor mask with low selectivity while the $SiO_2$ particles and PS beads are difficult to arrange in the desired patterns. The schematic of dry etching is shown in Figure 4.2.

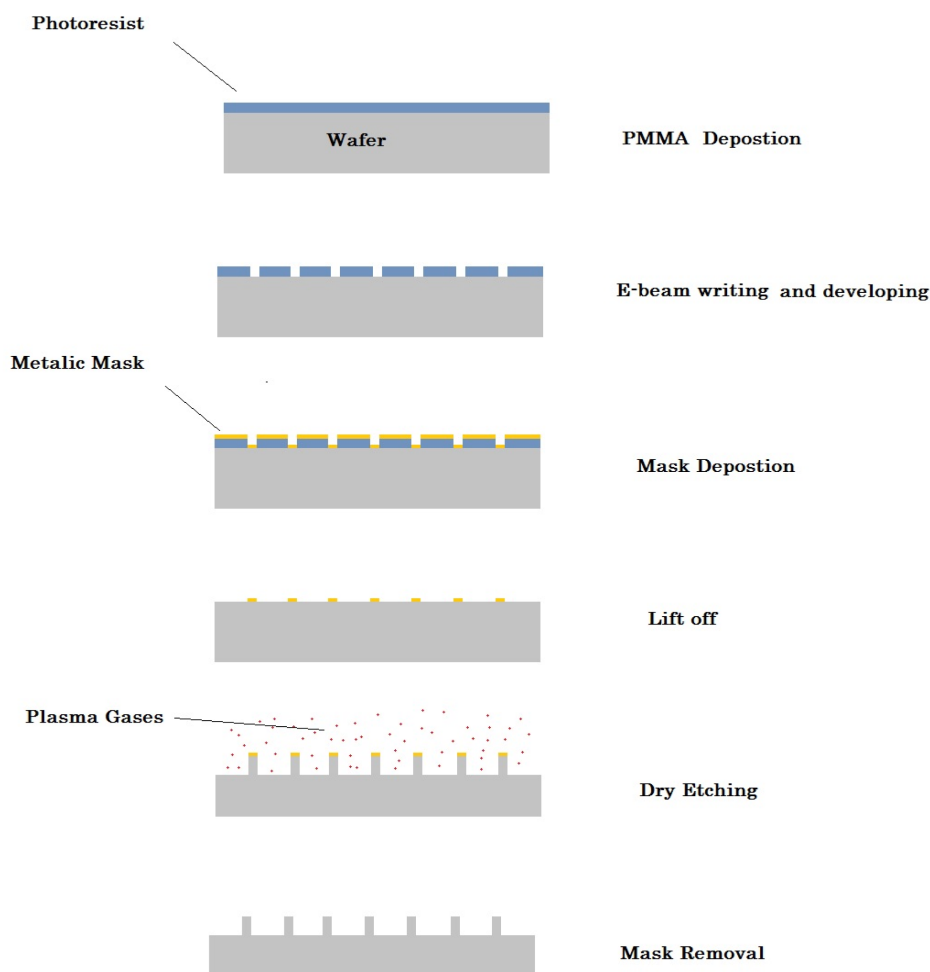


Figure 4.2: Schematic of a nanowire fabrication process by dry etching

In RIE system, a single RF plasma source controls both the density and energy of ions,

which makes it hard to balance the etch rate, anisotropy and damage control of nanowires. On the other hand, introducing ICP source can manage to generate plasma density 10-100 times more at pressure 5-100 times lower than RIE [103]. ICP-RIE decouples the incident ion energy from plasma density generation by applying RF power independently to a coil wrapped around the plasma chamber . Controlling both features independently gives higher etch rate due to high plasma density and high morphology control due to independent ion energy control using forward power, along with minimized physical damage due to ion bombardment to the intended throughputs.

The mask used for defining the nanowire arrays can be achieved through electron-beam, optical or nano-imprint lithography. Electron beam lithography (EBL) has an edge over optical lithography as the resolution is limited to optical lithography due the diffraction limit. The smallest feature reported by optical lithography is 50 nm. Whereas, electrons having much lower wavelength than UV helps e-beam lithography patterning the features in sub-10 nm range. Nano-imprint Lithography is another method to achieve features up to sub-50-nm with the cost much lower than EBL [104]. In this technique, a mold having nanometer scale features is pressed into a thin resist film on the substrate. Then the remaining resist on compressed areas is removed by RIE or wet etching. Later, either the resist can act as mask or metal can be deposited or sputtered as a mask. In this work, we have used e-beam lithography and ICP-RIE etching for nanowires in silicon (crystalline and amorphous), GaAs and GaN. Our methods and results are discussed in the following sections.

### 4.3.3 Crystalline Silicon Nanowires

Fabrication of ordered vertical crystalline silicon nanowires and the precise control on their morphology has become an established process in the past couple of years [23, 35, 36, 70,

| Parameter | $C_4H_8$ | $SF_6$ | ICP | CCP | T | P | Etch Rate |
|---|---|---|---|---|---|---|---|
| | (sccm) | | (W) | | (°C ) | (mT) | (nm/min) |
| Value | 42 | 22 | 1200 | 20 | 15 | 10 | ∼400 |

Table 4.1: Pseudo Bosch etching parameters for Silicon Nanowires

101, 105, 106] for various applications including work done by our group. In the ICP-RIE process, the gas mixture of $SF_6$ and $C_4H_8$ is used as the etchant and best results are achieved with aluminum as a mask. In this famously known as Pseudo-Bosch process, the etching rate and passivation rate are controlled independently by $SF_6$ and $C_4H_8$ respectively. The fluorine ions and radicals from $SF_6$ at a specific forward power etch the silicon and make the end product $SF_4$. The ionization of $C_4H_8$ creates polymer chains of $CF_2$, that act as a passivation layer on the silicon surface. Thus, creating an appropriate balance of plasma density and ion energy, control over the etching process can be achieved where undercutting, surface passivation and sidewall roughness can be reduced to achieve vertical and smooth sidewals [107]. The process used here was developed initially by a previous lab member Reza Khorasaninejad but it was further extended to control the shape and taperedness of silicon and a-Si nanowires. The parameters used for Pseudo-Bosch etching of silicon are shown in table 4.1.

In order to achieve highly ordered arrays with controlled diameter and spacing, we use the e-beam lithography to pattern the hard masks. PMMA950-A3 (Poly(methyl methacrylate)) was spin-coated on a silicon wafer at a thickness of around 170 nm, which was further baked at 180°C for 20 minutes. Patterning using e-beam was done at 20 kV on the circular-filled, periodically arranged design patterns created by RAITH150 two CAD software. The step size of e-beam was ∼10 nm with a beam size around 7-8 nm to write on the e-beam resist. This method is different than the conventional method in which changing

dosages at large step sizes, equal to the intended periodicity of the nanowires, were used to achieve desired diameter size. The current method helps in the flexibility in the design of the nanowire patterns. The patterned sample was developed in Methyl-isobutyl-ketone (MIBK) and isopropyl alcohol (IPA) solution in 1:3 proportions respectively for 30 seconds and then IPA or water is used as a stopper. Then the sample was installed in an upside down rotating stage in Intlvac e-beam physical deposition chamber to deposit $\sim$30 nm thick aluminum as a mask. The sample was then put in acetone or PG remover solution to remove the remaining e-beam resist and metal. Through lift-off process, the masked sample is put in an oxygen plasma ashing chamber to remove carbon impurities. Later on, the masked sample is installed in OXFORD PlasmaTherm ICP-RIE for the dry etching process. The etching chemistry is already mentioned above.

In [69], we demonstrated vivid structural color generation due to diffraction in highly ordered nanowire arrays (ideas developed by another group member and part of his thesis). Different colors can be generated either by changing the angle of the incident beam or changing the pitch between the nanowires in the array. Further, to generate pure colors, the pitch had to be controlled effectively over the array and the diameter had to be kept constant for different pitches. Due to the incapability of Raith software to define different step sizes in a single run, these goals were not possible using the method previously demonstrated [70] where dosage control was used to achieve different diameters and step size used as pitch. In our method, we used the Raith-150 two licensed CAD design software to build the array of circular patterns with a step size of 10-20 nm depending on the required diameter, and keeping the balance between resolution and time consumption. The method gave us fairly accurate results and made it possible to create different pitches in a single patterning saving time and resources. Figure 4.3 shows the scanning electron microscope (SEM) images of the fabricated nanowire arrays with pitches ranging from 400 nm to 1200 nm. Using this method, we could achieve the pitch as small as 200 nm. At

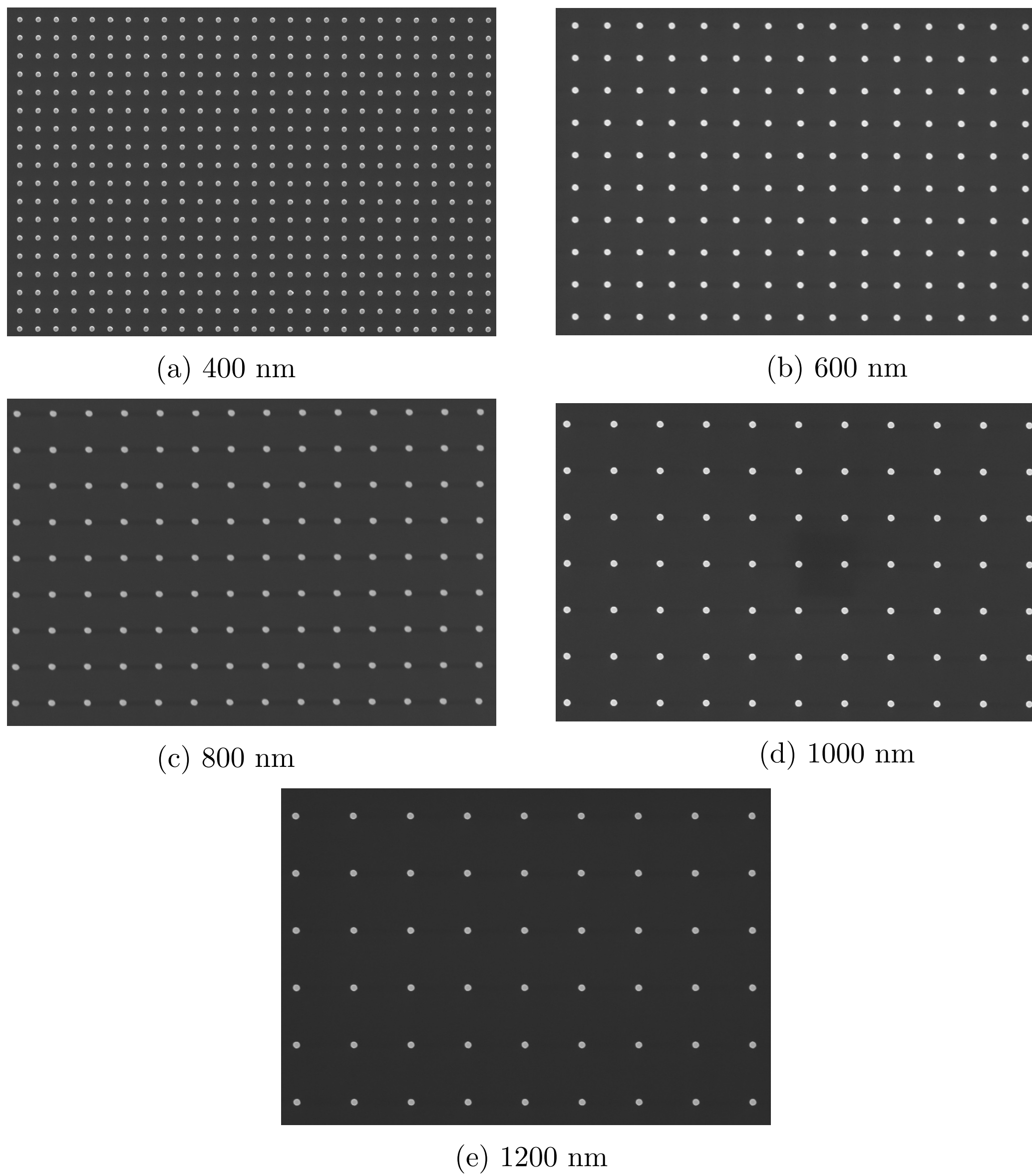

(a) 400 nm

(b) 600 nm

(c) 800 nm

(d) 1000 nm

(e) 1200 nm

Figure 4.3: Top-view SEM images of silicon nanowires at different pitches.

smaller pitches, the dosage needs to be reduced by ∼10% to keep the diameters constant.

While studying the optical properties of cylindrical nanowires, the change in cross-section geometrical shapes of the nanowires also demands an attention. Having a powerful anisotropic etching technique, it is possible to control the shape of nanowire cross-section and it calls for an opportunity to explore the properties of such nanostructures. Figure 4.4 shows SEM images of nanowires with square, triangular and circular cross-sections. The length of the nanowires is ∼1 $\mu$m in all these samples. As can be seen, good reproduction of the desired shapes is achieved. As discussed in the Chapter 3, some interesting properties are observed when the cross-section shapes of nanowire change.

In addition to exploring cross-section shapes, the tapered and disordered profiles of nanowires can also be achieved. In the tapered profiles, the etching recipe had to be modified by reducing the passivation gas $C_4H_8$ and increasing the forward power. Theoretically, the increased forward power should be etching away the mask quickly whereas decreased passivation layer should increase the lateral etching of the nanowires. Although, the mask seems to remain to intact on the top of the nanowires as shown in Figure 4.5(b), the nanowires showed taperedness owing to the reduced passivation gas. The etching recipe used for achieving the tapered profiles is shown in Table 4.2.

| Parameter | $C_4H_8$ | $SF_6$ | ICP | CCP | T | P |
|---|---|---|---|---|---|---|
| | (sccm) | | (W) | | (°C ) | (mT) |
| Value | 33 | 22 | 1200 | 22 | 15 | 10 |

Table 4.2: Etching parameters to achieve tapered profiles for Silicon Nanowires

For creating random patterns, the individual elements of circular patterns were moved into random directions, starting from the ordered pattern. despite being a laborious process, it ensures the randomness in the nanowire pattern remains high. On the other hand,

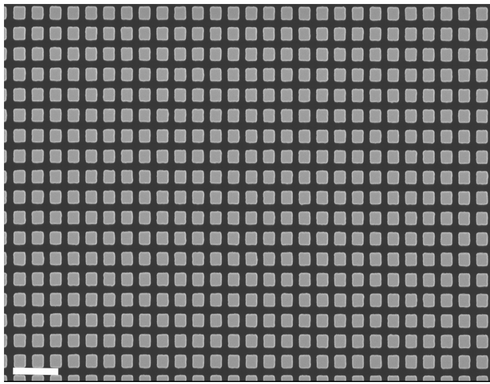

(a)

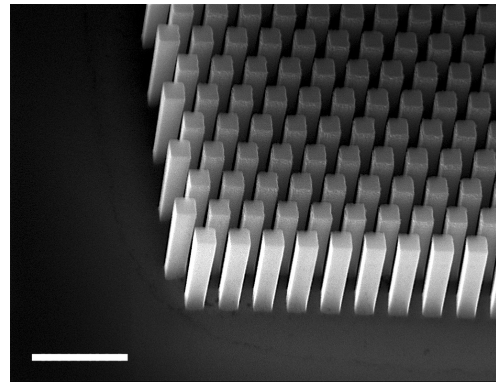

(b)

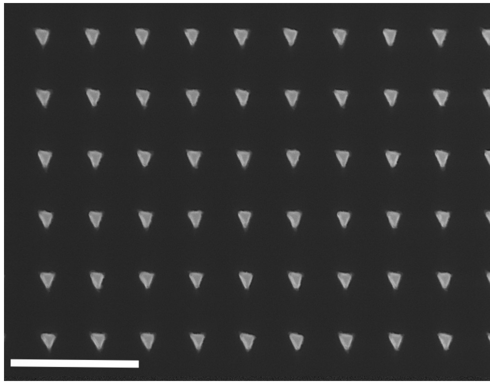

(c)

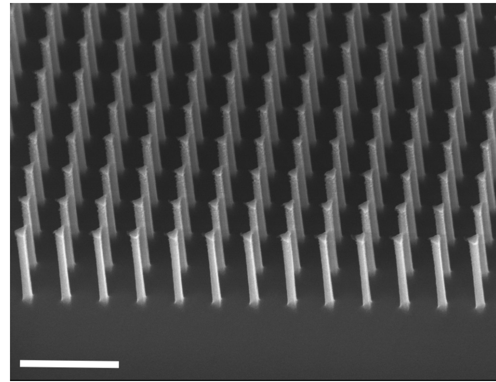

(d)

Figure 4.4: Top-view and side-view SEM images of silicon nanowires with (a),(b)square and (c),(d)triangular cross-sections. The scale is $1\mu$m for all figures.

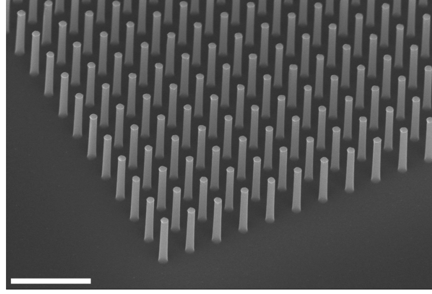

(a) Ordered Cylindrical Nanowires

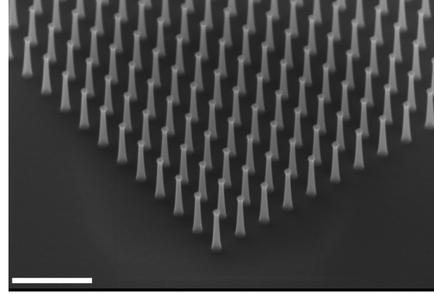

(b) Tapered Nanowires

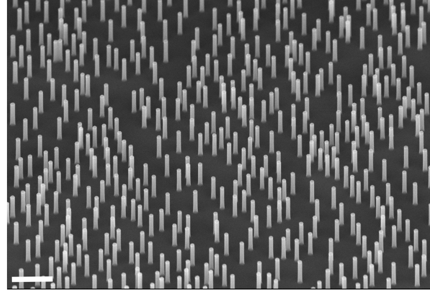

(c) Disordered Cylindrical Nanowires

Figure 4.5: Side-view SEM images of silicon nanowires with (a) Ordered (b) Disordered arrangement and (c) Tapered longitudinal profile. The scale bars are 1 $\mu$m for all figures.

designing ordered patterns is the inherent capability of RAITH150-two CAD software. Figure 4.5(c) shows the side-view SEM image of the disordered nanowires showing the presence of truly random structures.

### 4.3.4 Amorphous Silicon Nanowires

We also investigate whether a-Si nanowires can be fabricated on thin films for applications in transparent and colorful solar cells. We were afraid that ICP-RIE etching could lead to sidewall disintegration in an amorphous material. Normally a-Si etching is different from crystalline silicon etching.

Figure 4.6 shows the a-Si nanowires on a glass substrate etched using the same recipe

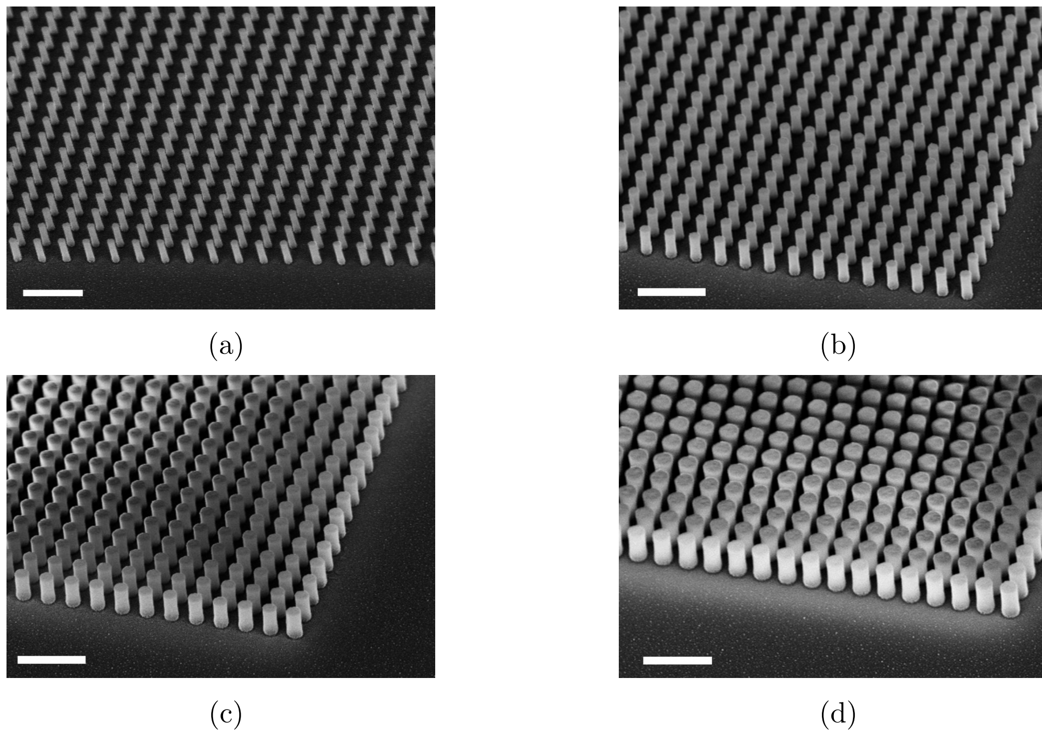

Figure 4.6: Side-view SEM images of a-Si nanowires fro four diameters (a) 100 nm (b) 150 nm (c) 200 nm and (d) 250 nm. The scale is 1$\mu$m for all figures.

as our crystalline silicon nanowires. This is due to the nature of anisotropic dry etching in which DC bias predominantly controls the morphology due to the energy of fluorine ions and radicals [107]. To our knowledge, this is the first demonstration of top-down etched a-Si nanowires with such precise control over dimensions. In fact, in this work we were able to control the nanowire length right down to the glass substrate as will be described later.

### 4.3.5 Gallium Arsenide Nanowires

Though ICP-RIE etching has been widely used for GaAs semiconductor lasers [108–110], surprisingly it had not been applied widely for nanowire based applications. The first fully controlled method for etching GaAs nanowires was developed during this study. We can control the diameter, pitch, and length of the nanowires independently. The GaAs nanowires were fabricated using a top-down approach by patterning a metal mask with e-beam lithography and then using ICP-RIE etching with $Cl_2/N_2$ chemistry to form the nanowires from (100) GaAS wafer. The samples were cleaned using 2-propanol, acetone, and DI water in succession and then sonicated in acetone for approximately 10-15 min. PMMA 950 A3 was spin coated on the wafer to the thickness of $\sim$170 nm and baked in a YES- CV200RFS plasma strip/descum system. The pattern was written using Raith 150 Two (ultra-high resolution direct write tool) at 20-25 kV and was developed in MIBK : IPA solution for 30 s. Metallic hard masks were deposited using Intlvac Physical Vapor Deposition System and lift-off was performed in Remover PG solvent stripper. The metals used for hard mask include Cr, Ni, Al, and Ti. The nanowires were arranged in a highly uniform square lattice over a 100 $\mu$m $\times$ 100 $\mu$m array and were targeted for many variations in diameters and pitches.

To achieve high aspect ratio in nanowires requires high selectivity of the metal mask in

the $Cl_2/N_2$ chemistry. Nickel has been successfully used as a metal mask for etching GaAs nanostructures [111]. However, Ni is avoided to be exposed in III-V etching chamber due to its role as a potential contaminant to some devices (for example, as a magnetic impurity in the fabrication of super- conducting nanowires) in the cleanroom. Instead, chromium (Cr) was used, which also has low etch rate in $Cl_2/N_2$ chemistry. However, Cr being a soft metal leads to ′nano-whiskering′ where Cr residue on side of the mask remains on the pattern after lift-off as it does not tear off well from the sidewalls of the pattern. This is a common problem with Cr which is exacerbated as the thickness of the mask increases [111].

Figure 4.7a shows a scanning electron microscope (SEM) image of a 45 nm Cr mask after lift-off. The nano-whiskers around the circular mask patterns are clearly visible. After etching, the whiskers were etched down to form nano-walls of sub-10 nm dimensions, as shown in figure 4.7b.So the etching is very anisotropic. This problem was overcome by depositing a 20 nm aluminum layer before depositing the Cr mask. The Al layer allows for the clean lift-off as observed in figure 4.7c. Clean lift-off was achieved for varying thickness of Cr (ranging from 20 nm to 45 nm) on the top of 20 nm thick Al. Another advantage of using Al at the base is that it can be etched in Al etchants, which does not affect the GaAs nanowires, and the metal mask removed after the fabrication. This is difficult with Cr since Cr etchant also etches GaAs. Cr also gets etched in our plasma-etching recipe, though it is a slow process (at a rate of $\sim$10nm/min) and hence the thickness of Cr needs to be adjusted for different lengths of nanowires. Use of such hybrid metals as masks is the first demonstration of its kind to our knowledge (though metals like Cr and Titanium are used as adhesion layers for electrical contacts).

The etching of the nanowires was done in an Oxford Plasma-Therm ICP-RIE system using $Cl_2/N_2$ chemistry. Plasma conditions were optimized to achieve vertical sidewalls and reproduction of the metal mask into the semiconductor nanowire allowing for controlled

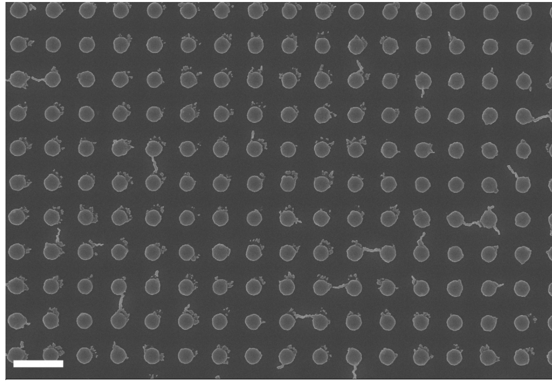

(a)

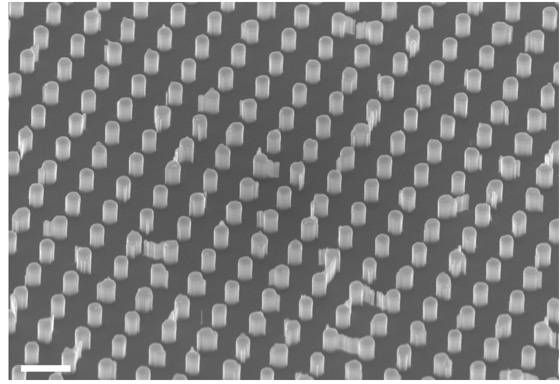

(b)

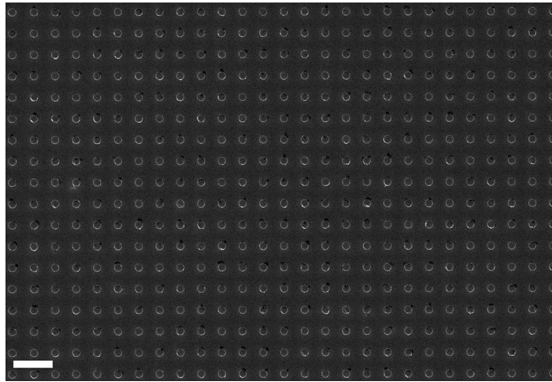

(c)

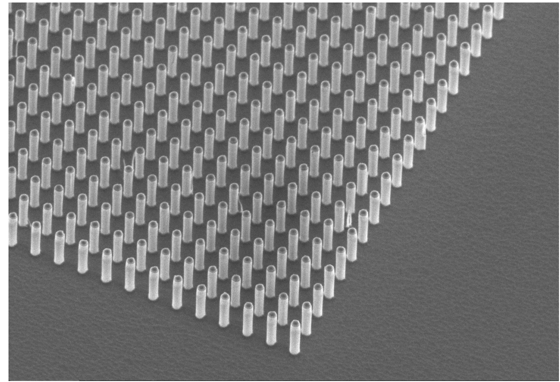

(d)

Figure 4.7: (a)Top-view SEM of chrome masks after lift-off, (b) Side-view SEM of GaAS nanowires after etching of (a). (c)Top-view SEM of Al/Cr mask after lift-off, (d) Side-view SEM of GaAS nanowires after the etching of (c). The scale is 1$\mu$m for (a) and (b) and 1$\mu$m for (c) and (d).

fabrication of the nanowire. Chlorine is widely used in all kind of wet and dry etching due to its high reactivity. In anisotropic etches, $Cl_2$ requires neutral gas species to enhance the sputter desorption of etch products such as $GaCl_x$ and $AsCl_x$, thus reducing the chlorine radicals to control the etch rate. Most widely used neutral gas species are Ar and $N_2$. We chose $N_2$ for its moderate sputtering efficiencies, allowing the fine tuning of chlorine radicals density. The previous researchers while testing the GaAs etching, explored the etching parameters in their distinct etching chambers. In these studies [112–115], the etching parameters vary widely ranging from 1:4 to 10:1 for $Cl_2$:$N_2$ ratio,100-1000 W for ICP Power and 60-200 W for forward power. The chamber pressure is considered safe under 10 mT. However, too low pressure could lead to lower etch rates and mask erosion. The most studies used 5 mT as their sweet spot, it, however, did not work for us as it reduced the etch rate drastically leading to tapered structures. Temperature does not make a significant effect on the etch rates and sidewall profiles.

Optimized etching was achieved with 20 sccm of $Cl_2$ and 5 sccm of $N_2$. The RF source power was 500 W, ICP power was 60 W with the chamber pressure of 10 mTorr. $N_2$ allows for surface passivation of the nanowires and was chosen specifically instead of $CH_4$ or Ar which can lead to polymerization and redeposition. Etching was done at a rate of ∼10 nm/s at a plate temperature of 20°C. These parameters lead to very good quality GaAs nanowires, not reported before with etching. The most successful etching recipe for GaAs nanowires is shown in Table 4.3.

| Parameter | $Cl_2$ | $N_2$ | ICP | CCP | T | P | Etch Rate(nm/min) |
|---|---|---|---|---|---|---|---|
| | (sccm) | | (W) | | (°C ) | (mT) | (nm/min) |
| Value | 20 | 5 | 600 | 50 | 20 | 10 | ∼1100 |

Table 4.3: Etching parameters to achieve GaAS Nanowires of 1$\mu$m length

Figure 4.8 shows typical SEM images for some of the GaAs nanowires of different lengths, diameters, and pitches. As can be readily seen, the arrays are highly uniform and the sidewalls are vertical. There is no undercutting of the mask and the features in the mask pattern are accurately reproduced. The diameters achieved were as small as 30 nm and as large as 400 nm. Diameter to pitch ratio of 60% was achieved, the highest packing density reported for GaAs nanowires. This allows us to fabricate nanowires with parameters which have been simulated to be optimum for wide band absorption (as will be discussed in next Chapter). The smaller diameters were achieved by writing patterns at smaller beam step size, thus changing the size of the mask pattern and not by severe undercutting as previously demonstrated [111]. The sample with nano-whiskers from the Cr mask was etched to a depth of ~600 nm as shown in figure 4.8b showing the anisotropic nature of the etch.

Although some of these nano-whiskers were less than 10 nm in width, they were nevertheless successfully maintained to the bottom of the etch with no sign of undercutting. This clearly shows that the etching process is highly anisotropic and reproduces the mask pattern into the GaAs semiconductor extremely well. This allowed us to achieve small diameters for long lengths as shown in figure 4.8a where the diameter is 65 nm and length is 2.2 $\mu$m. For this sample, the top ~100 nm has been eroded due to complete etching of the mask. This can be avoided by increasing the Cr thickness. For the 1 $\mu$m long nanowires, 20nm Al and 30nm Cr was used as a mask while for 1.9 $\mu$m and 2.2 $\mu$m long nanowires, 15 nm Al/45 nm Cr was used as a mask.

To confirm the etching quality, transmission electron microscopy (TEM) images were obtained using a JEOL 2010F by our collaborators at McMaster University, and a representative image at the nanowire surface is shown in figure 4.9. The diameter for the nanowire was 135 nm in the range where high solar absorption efficiencies have been predicted [48].

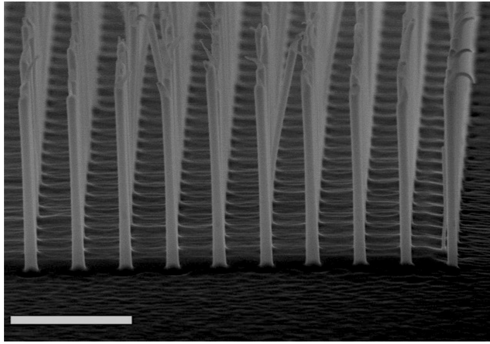

(a) D - 65 nm, P- 400 nm

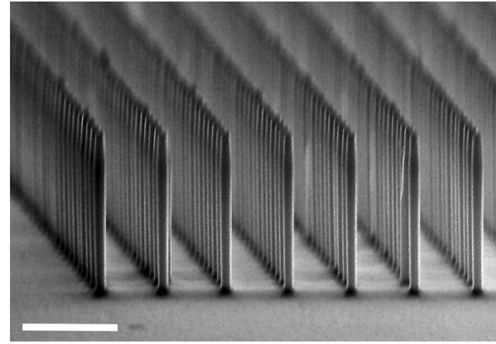

(b) D - 100 nm, P - 500 nm

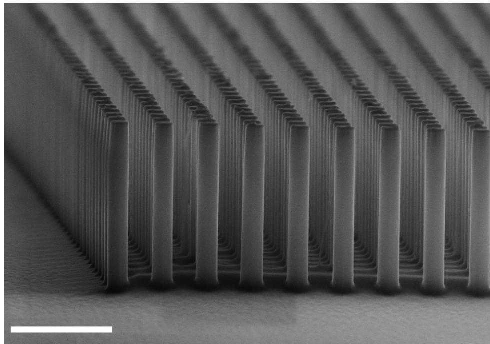

(c) D - 200 nm, P - 500 nm

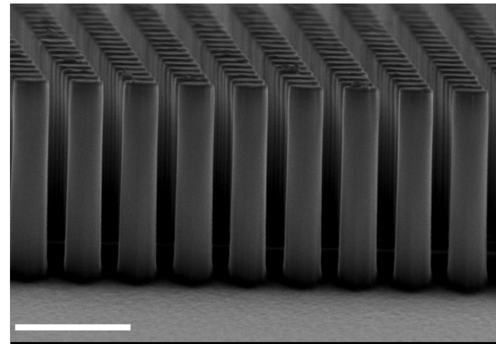

(d) D - 300 nm, P - 500 nm

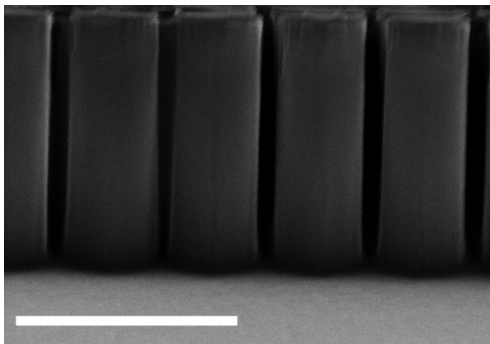

(e) D - 400 nm, P - 500 nm

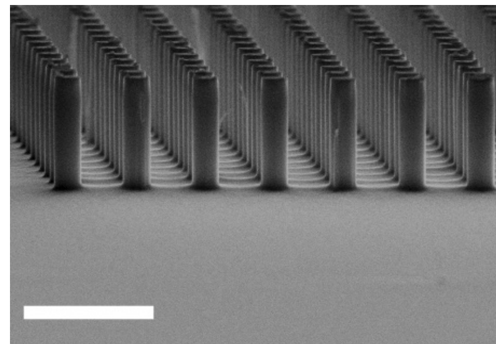

(f) D - 400 nm, P - 1100 nm

Figure 4.8: Side-view SEM images of GaAS nanowires for different diameters and pitches. The details for each figure are shown in the sub-captions. The scale is 1 $\mu$m for figures (a)-(e) and 2 $\mu$m for (f)

.

As can be seen from the image, the sidewall roughness is less than 1 nm. Also as will be shown later, the optical performance of the fabricated nanowire arrays is very similar to what is predicted by the simulations, which again proves the quality of the nanowires fabricated.

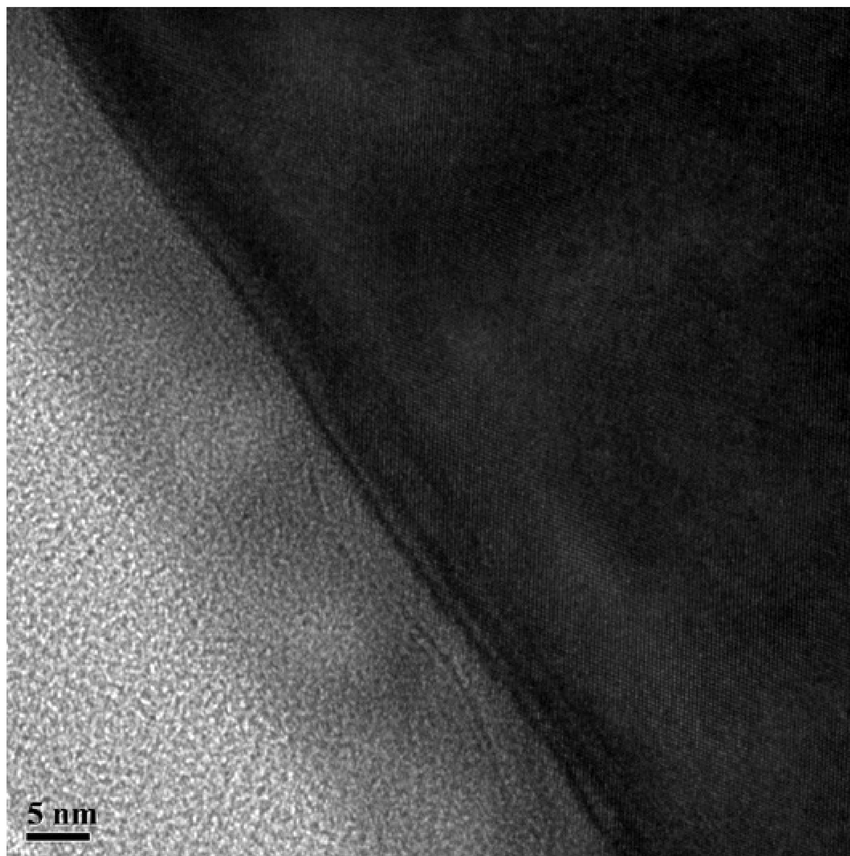


Figure 4.9: TEM image of the GaAs nanowire with 135 nm dimeter.

The tapered nanostructures are known for their strong antireflection properties compared to cylindrical nanowires [34,116]. To reduce reflections, it is desirable to have tapered nanowires with the diameter being smaller on the top and slowly increasing to the desired value [101]. Tapering can allow for adiabatic coupling of incident light into the nanowire optical modes, thus reducing reflections and increasing efficiency. Thus, we also investigated whether we could achieve tapered nanowires using the etching method. The idea

was based on the controlled etching of the mask. This was achieved by using a Ti/Cr/Ti sandwich metal mask. The bottom Ti layer was to achieve clean lift-off while the Cr layer acted as a metal mask for etching. The top Ti layer provided a controlled etching of the mask. While Ti etches in $Cl_2$ based chemistry, the process is slowed down due to the formation of the native oxide [103]. Figure 4.10 shows SEM images of tapered nanowires 1.9 $\mu$m in length and around 180 nm diameter at the base. As can be readily seen and as opposed to Figure 4.8, the nanowires are tapered for the top 300 nm and then follow a columnar geometry. To our knowledge, this is also a unique nanowires shape reported for the first time.

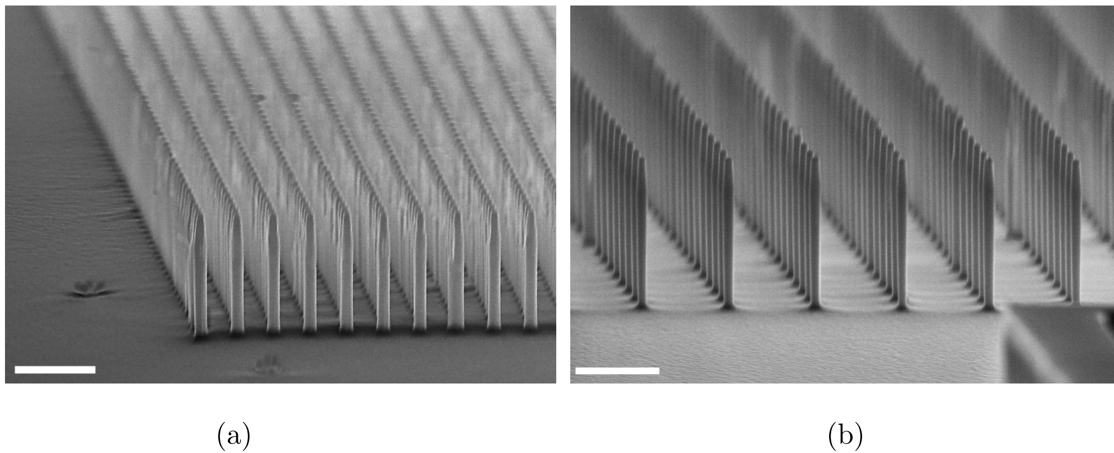

(a) (b)

Figure 4.10: Side-view SEM images of GaAs tapered nanowires with (a) 2.2 $\mu$m (b) 1.6 $\mu$m lengths. The scale is 1 $\mu$m for both figures.

### 4.3.6 Gallium Nitride Nanowires

GaAs interests the researcher community for its practical applications in ultraviolet-blue lasers, LEDs or photodetectors. There are several growth based nanowires and their applications reported previously [52, 60, 95–97, 117]. Also, there are some attempts are made to etch the nanowires using ICP etching [118, 119]. But the cylindrical nano-waveguides with

vertical sidewalls is still a challenging task in both top-down and bottom-up approaches. We have attempted to achieve these nanostructures using $Cl_2$ and $N_2$ chemistry using various masks and additional passivation . The full list of etching recipes and masks used are shown on the table 4.4. Initially, the standard clean recipes to etch III-V semiconductors had been used on the Cr, Al/Cr metal masks. Since GaN is a hard material compared to GaAs, the chlorine supply, and forward bias was increased initially to physically and chemically increase the etch rate. The results showed highly tapered structures with the masks completely etched away. In the next step, the $N_2$ ratio is decreased drastically to allow the undercutting to balance the profile. The etch rate was slightly increased but not much change was observed in the nanowire profile.

| # | $Cl_2$ | $N_2$ | Ar | $CH_4$ | ICP | CCP | T | P | Mask |
|---|---|---|---|---|---|---|---|---|---|
| | (sccm) | | | | (W) | | (°C ) | (mT) | (nm) |
| 1 | 38 | 13 | | | 500 | 200 | 20 | 5 | Al/Cr - 25/25 |
| 2 | 38 | 20 | | | 500 | 200 | 20 | 5 | Cr - 45 |
| 3 | 38 | 5 | | | 500 | 200 | 20 | 5 | Al/Cr - 10/40 |
| 4 | 25 | 5 | | | 500 | 100 | 20 | 10 | Al/Cr - 10/40 |
| 5 | 25 | | 2 | | 150 | 40 | 20 | 10 | SiN//Cr/Al - 100/15/40 |
| 6 | 38 | 20 | | 10 | 500 | 200 | 15 | 10 | SiN/Cr/Al - 100/15/40 |
| 7 | 38 | 20 | | 10 | 500 | 200 | 15 | 10 | Ni/SiN/Cr/Al - 100/15/40 |
| 8 | 38 | 20 | | 10 | 500 | 200 | 15 | 10 | $SiO_2$/Cr/Al - 100/15/40 |
| 9 | 38 | 20 | | 5 | 500 | 200 | 13 | 10 | $SiO_2$/Cr/Ni/Al- 100/15/40 |

Table 4.4: Etching parameters for different tests to fabricate GaN Nanowires

Later on, a standard etch recipe was used with $Cl_2$ and Ar by depositing SiN on GaN

before patterning the masks on the top. SiN was deposited using standard PECVD recipe shown in Table 4.5. Also, methane was added to increase the surface passivation. SiN was deposited with PMMA and baked in the oven for 20 minutes. Then the periodic nano-patterning was done using e-beam lithography and the metal masks were deposited on the top. Finally, the remaining metal and PMMA was removed using PG remover. Later on, the standard SiN recipe was used to etch SiN that was not under the metallic masks. The SiN recipe used is shown in table 4.6. The thin film was etched till the GaN wafer was exposed and then the sample was plasma ashed with oxygen to remove carbon impurities and then etched using the recipes number 5 and 6.

| $SiH_4$ | $N_2$ | P(mT) | RF Power | Temp(°C ) | Deposition Rate(nm/min) |
|---|---|---|---|---|---|
| 30 | 90 | 600 | 40 | 330 | 20 |

Table 4.5: Parameters for SiN thin film deposition on GaN wafer

| $SF_6$ | $C_4H_8$ | P(mT) | RF Power | ICP | Temp(°C ) | Etch Rate(nm/min) |
|---|---|---|---|---|---|---|
| 32 | 28 | 10 | 20 | 1200 | 15 | 23.81 |

Table 4.6: Etching parameters for SiN thin film deposited on GaN wafer

| $SiH_4$ | $O_2$ | P(mT) | RF Power | Temp(°C ) | Deposition Rate(nm/min) |
|---|---|---|---|---|---|
| 30 | 45 | 600 | 40 | 250 | 29 |

Table 4.7: Parameters for $SiO_2$ thin film deposition on GaN wafer

Similarly, the same process was used by replacing SiN with $SiO_2$. The deposition and etching recipes for $SiO_2$ are shown in Tables 4.7 and 4.8. To check the etch rates for SiN and $SiO_2$, a dummy wafer was deposited with the respective thin films and half of the wafers were coated with an aluminum mask. The etching was performed on that wafer

| $C_4H_8$ | $O_2$ | P(mT) | FWD Power | ICP | Temp(°C ) | Etch Rate(nm/min) |
|---|---|---|---|---|---|---|
| 40 | 15 | 10 | 200 | 2500 | 50 | 430 |

Table 4.8: Etching parameters for $SiO_2$ thin film deposited on GaN wafer

to make sure the standard etch rates are accurate. The etch rates were quite precise for both the materials. A partial success was achieved to reach ∼85° sidewalls angles for diameters larger than 200 nm, as shown in figure 4.11. The etching recipes need to be further explored with different gasses and etch masks to achieve vertical nanowire profiles. To our knowledge, this is the best sidewall angle achieved for the GaN nanowires.

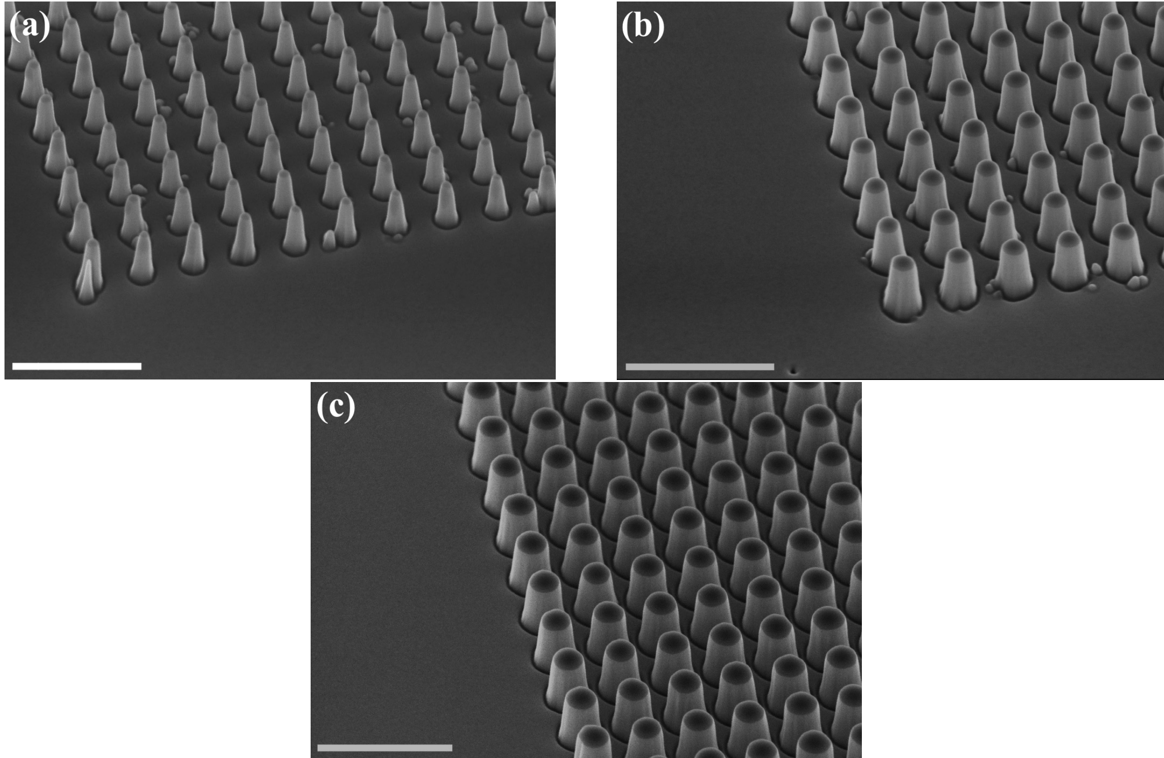


Figure 4.11: Side-view SEM image of GaN nanowires for three diameters (a) 100 nm (b) 200 nm (c) 260 nm. The scale bar is 1 $\mu$m.

### 4.3.7 Diameter Distribution of Nanowires

To verify the consistency of nanowire patterning and etching, the diameter distribution of nanowire was calculated using image analysis software ImageJ. The top-view SEM images of nanowires having 85 nm targeted diameter with different pitches and random distribution were analyzed at 10,000 × magnification. The diameter distribution is plotted in figure 4.12. The majority diameters lie in the range of 82 nm to 88 nm while the targeted diameter

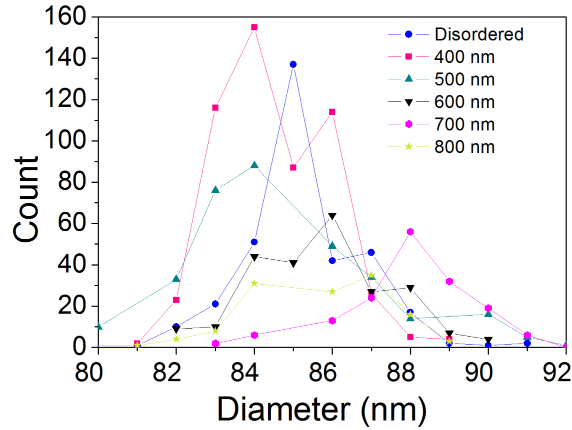


Figure 4.12: The diameter distribution of silicon nanowires with 85 nm diameter and pitches ranging from 400 nm to 800 nm. The distribution for disordered nanowires is also plotted.

was 85 nm. The diameter count decreases with increase pitch because of the reduction in fill fraction for the nanowires. The distributions indicate the standard deviation of ± 3 nm from the original diameter of 85 nm. This gives an idea about the consistency with which the patterning and etching produce the lateral dimensions of the nanowires arrays and some of the most consistent nanowires ever reported. This consistency helps us completely verify the various physical features in chapter 3.

## 4.4 Conclusion

In this Chapter, fabrication techniques for silicon, a-Si, GaAs, GaN to achieve periodic nanostructures of desired shape and dimension have been summarized. For silicon nanowires, the main achievement was improving the fabrication process to achieve higher control in diameter and pitch especially when different geometrical parameters are to be changed close by and controlling the tapered profiles of the nanowires. Also, the first etch controlled a-Si nanowires were demonstrated and a new process for GaAs nanowires to achieve desired parameters were developed. In the end, the etching process to fabricate cylindrical vertical GaN nanowires were shown. Various masks and etching parameters were tested to achieve vertical profiles for sidewalls and a partial success was achieved by decreasing the sidewall angles of the nanowires. These nanostructures are important because they have the potential to be used in the advanced optoelectronics applications in the future. Concluding Summary:

- Highly controlled dry etching processes were developed for GaAS, Si, a-Si and GaN nanowires.
- Diameter variation in an array was as low as 3 nm.
- Different shapes were demonstrated showing the capability of ICP etching.
- Tapered nanowires were achieved for GaAs and silicon nanowires.
- These controlled fabrication processes allow us to study and fully understand the optical properties of the nanowire arrays and will be discussed in the next chapter. This allowed us to design controlled experiments for the first time in the field.

# Chapter 5

# Optical Measurements and Experimental Studies

## 5.1 Introduction

A material and its surface properties can be studied using various characterization techniques. Reflection is one of the most fundamental optical response of a material. Color and luster are the few intuitive responses of a surface when photons in the visible region get reflected back from it into human eyes. Reflection, however, is not limited to the visible range and requires special optical setups to detect the photons outside the range of the human eye. The color of a material represents the range of wavelengths in visible region that are absorbed and reflected from a surface, whereas luster represents the type of reflection and hence the texture of the surface. Reflection from the surface of a material can be quantified using an appropriate optical setup where lenses, beam splitters, and a spectrometer is required. In the previous reflection studies of semiconductor nanowires, researchers have followed various approaches to representing reflection parameters to quantify the nanowire properties. The initial antireflection studies of nanowires involved the randomly grown

or wet etched high-density nanowire ensembles which were highly dominated by diffuse reflections. These diffuse reflections usually happen due to the high disorder and random orientation of nanocylinders. In ordered arrays of nanowires, light diffraction could be observed due to the presence of lattice spacings larger than the wavelength. For cylindrical nano-pillar arrays, it is necessary to avoid spurious spectral features in order to accurately understand their optical response experimentally. To achieve that we need to focus on reducing both the N.A of the focusing objective and lattice spacing of the arrays. Low N.A′s are preferred during the reflection measurements as they significantly reduce the diffuse reflection and also the beam depolarization is avoided at low numerical apertures [120]. For incident light polarized with the electric field in the x-direction, the electric field is antisymmetric under reflection about the y-z plane.

The reflections features of the nanowires give an important of information about the waveguiding properties of the nanowires. The nanowires are characterized using the reflection while they are on the top of a substrate. Therefore, they should be showing the reflection features of the bulk where they do not absorb very well, which is usually at the longer wavelengths. At the resonant wavelength, the nanowires are highly absorbing showing a reflection dip almost close to 0%, due to the excitation of modes. At wavelengths below the resonance, the reflections tend to increase as the effective index tends to be larger, however, they can still absorb as the other higher modes could be exciting.

### 5.1.1 Reflection and Transmission Measurements setups

#### Filmetrics F-40

We used two different types of measurement instruments to collect reflection and transmission spectra. One of the setups is the Filmetrics F-40, which provides a squared measurement spot with size as small as 5 $\mu$m in the wavelength range of 400 nm to 850 nm.

However, to avoid high N.A$'$s, we chose the spot size as large as 25 $\mu$m. The sample is placed on the microscopic stage under the objective, and the incident and reflected beams are passed through the same objective. The reflected signal is fed to the spectrometer connected to the microscope.

**Home-made optical setup**

The second setup for reflection measurements is the home made optical setup having 20 objectives, splitters, a halogen lamp and a spectrometer as shown in figure 5.1. Light from an Ocean Optics Halogen Lamp white light source was collimated and focussed to a spot size of $\sim$20 $\mu$m on the array with a focusing lens. Reflected light was separated from the incident beam using a 3-dB coupler. The reflected light was further split using a 90%-10% splitter where the 90% port was used to measure the reflection with a spectrometer while the 10% port was used to image the array. The imaging port allowed us to center the incident beam on a specific array under measurement. The reflection data was normalized by replacing the sample with an aluminum mirror with known reflection spectra in the measured wavelength band. For measuring the transmission, light at the transmission end was focused into an optical fiber and measured with a spectrometer. The transmitted light was normalized with respect to transmission from just the glass substrate.

### 5.1.2 Analysis of a Reflection Spectrum

A reflection spectrum of nanowire arrays mainly consists of three regions in the electromagnetic spectrum. The first region is the wavelength range longer than the guided waveguide reflection dip. These are at wavelengths that are larger than the radial dimensions (diameters) of the nanowires and lie above the leaky waveguide dip . These wavelengths being larger than the structures interact weakly with the nanowires reflecting directly from the

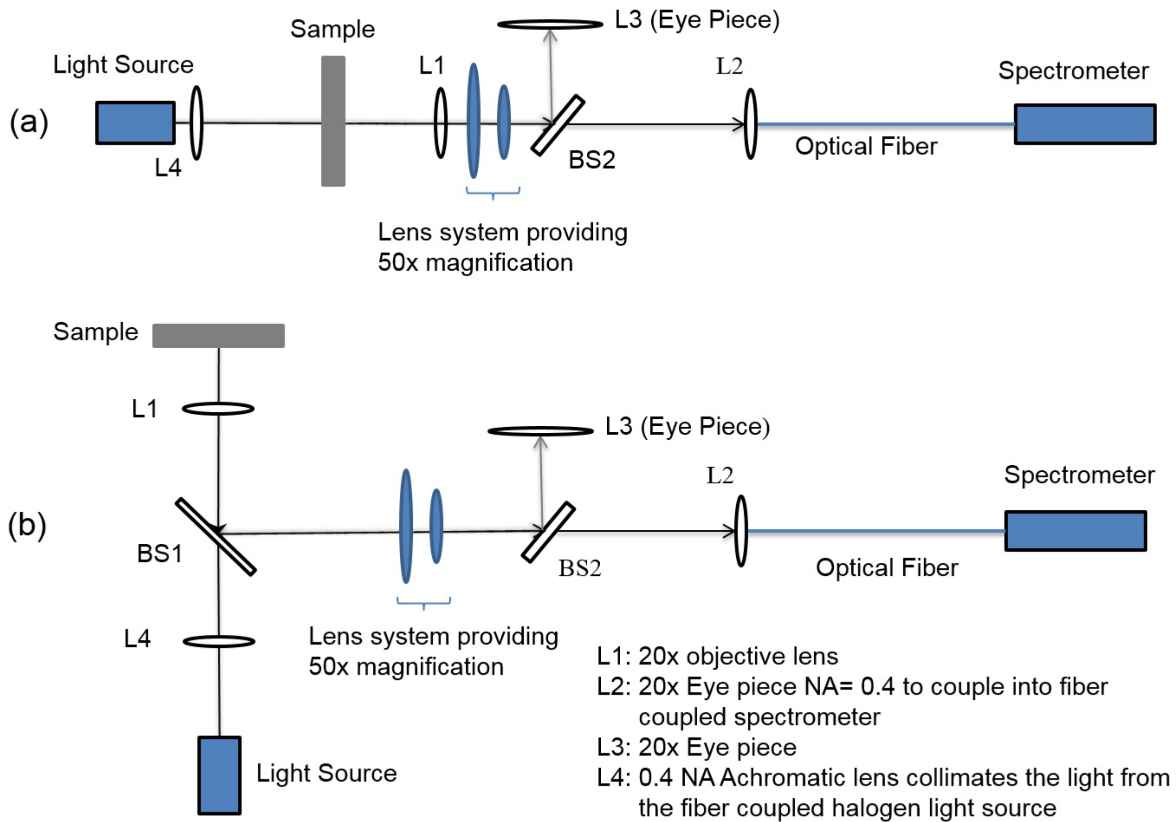


Figure 5.1: Home made optical setups to measure (a) reflections and (b)transmissions from the nanowire samples

substrate. The larger the wavelength, the more bulk reflection properties are observed. While going towards the smaller wavelengths, the interaction of photons starts becoming stronger with the nanowires and F-P (longitudinal) resonances start to dominate. This F-P cavity nanowire/substrate interface and nanowire/air or nanowire/mask interface. The second region is highly absorbing part of the nanowires showing the reflection minima of the complete spectrum. It is the region where leaky modes, as well as the F-P resonances predominantly, confine the energy inside the nanowires. As discussed in the previous chapter , the excitation of leaky waveguide mode is diameter dependent. So this region can show-up in any part of the spectrum depending on the diameter of the nanowire. The third region is located at wavelengths shorter than resonant reflection dip. It is the most complex region to interpret since the wavelengths are usually smaller than the nanowire diameters in this region, which causes multiple phenomena in this region. In this wavelength range the weakly guided higher order modes excite in this region. Furthermore, having the finite thickness and having the refractive index contrast at the top and bottom interface, this region also excites F-P resonances. However, since this region usually has high absorption coefficient leading to small absorption length and therefore, the F-P resonances usually do not dominate this region.

### 5.1.3 Structural Colors

When nanostructures interact with the photons behave differently than the bulk counterparts. Diffraction, scattering and waveguiding of photons allow the nanostructures to absorb, emit and reflect colors in the visible range. When it comes to semiconductor nanostructures, this paradigm shift is no stranger than other materials. As we have discussed that nanowires reflect the light differently for different wavelengths ranges compared to bulk materials. Their reflected properties can either be observed by collecting the reflec-

tion data using spectrometer or through naked eyes by observing the change in color. The structural color might not represent the material properties as quantitatively as the reflection measurements but after fine tuning the color information in hue, saturation and tint tagged along with material specificity and dimensions, the structural colors can be a useful information to understand the physical phenomenon and even be used in many applications. Color information of nanostructure can be collected by capturing them in an image under high magnification. One condition for observing or using the color information is to keep the exposure setting of the microscope and camera constant for every measurement. We used MX61 - Olympus Microscope for the measurement of structural colors of nanowires and the images were captured at 5 × magnification using brightfield mode. Let us now consider measurements done on different nanowires to interpret various physical phenomena like modal excitations, near-field coupling, the effect of length, taper and mask, and color.

## 5.2 Modal Excitations in Nanowires

### 5.2.1 Gallium Arsenide Nanowires

#### 1$\mu$m long nanowires

Figure 5.2 shows the measured (solid lines) and simulated (dashed lines) reflectance spectra for 1 $\mu$m long nanowires with a fixed pitch of 400 nm and diameter ranging from 30 nm to 230 nm. The measured reflectance data is represented in a two-dimensional (2D) contour plot in figure 5.2(a) and then as individual reflectance spectra in figures 5.2(b)-(d) for different diameters. While the 2D contour plot helps one visualize the wavelengths of high and low reflections and the effect of diameter, the individual reflectance spectra allow one to get an intuitive feeling about the various light interactions that happen within

the nanowires including regions of high absorption and regions where strong longitudinal modes exist. The diameter range has been divided into two different figures for ease of visualization and due to two different fundamental optical behaviors observed. For the larger diameter nanowires, a representative match between experimental and simulated results is shown in figure 5.2(d). Reflectance measurements taken from the GaAs substrate next to the arrays are also shown (black curve, labeled ′offpad′). There is an excellent agreement between the experimental and simulation results over the complete range of diameters studied. For the 30 nm diameter, the reflectance spectrum is slightly lower than that of the GaAs substrate, but has fundamentally the same shape, as confirmed by the simulation, indicating that the nanowires do not have a significant waveguiding effect and present only a minor optical perturbation over the measured wavelength range. For diameters ranging from 55 nm to 140 nm in figure 5.2(b), the measured reflectance is low for short wavelengths and then increases abruptly to approach that of the GaAs substrate in agreement with the simulations. The wavelength, at which this abrupt change occurs, increases with the nanowire diameter. This behavior is similar to that previously demonstrated for InAs [21]. As seen later with the aid of further simulations, these features are produced due to strong absorption peaks observed in these nanowires. As the diameter is increased above 140 nm as in figure 5.2(c), F-P like resonances due to longitudinal modes begin to appear in the reflectance spectra with the absence of the abrupt changes seen for smaller diameters. Strong F-P peaks suggest that the absorption within the nanowires has decreased allowing light to bounce back and forth many times within the nanowires. To our knowledge, this reflectance behavior at larger diameters has not been demonstrated before for III-V nanowires. These results suggest that the absorption is decreasing after a certain diameter, a fact previously seen theoretically. In this diameter range, the simulations also match the experimental data as in figure 5.2(d) for a diameter of 230 nm. Although simulated data is not shown in figure 5.2(c), a similar agreement between the experimental

and simulated spectra was also obtained for these other diameters.

### 2.2$\mu$m long nanowires

To determine the dependence of the reflectance on nanowire length, identical nanowires as used for figure 5.2 were fabricated but with more than twice the length. Figure 5.3 plots the measured (solid lines) and simulated (dashed lines) reflectance spectra for 2.2 $\mu$m long nanowires, with the pitch of 400 nm, and diameter varying from 40 to 205 nm. The same features and trends are observed as previously discussed for figure 5.2. Good agreement is again obtained between the measured and the simulated results over the complete range studied. As can be seen by comparing figure 5.2 and 5.3, the center wavelength where low reflectance and high absorption is observed does not change with length. However, the wavelength band over which low reflectance is observed does increase with increased length. These results show that the absorption features observed in the nanowires are due to the diameter dependent waveguide properties and not the longitudinal cavity resonances. For diameters ranging from 145 nm to 205 nm, the reflectance is lower than 5% over the complete spectral range. This behavior is different as compared to the same diameter range for the shorter length. The results suggest that the absorption has increased sufficiently with length to reduce the F-P resonances. This low reflectance would be beneficial for solar cell and photodetector applications.

### Absorption

In order to understand the spectral features observed in figures 5.2 and 5.3, the absorptance spectra for the nanowires were calculated from the same simulations used to calculate the reflectance (which showed good agreement with experimental data). Figure 5.4(a) and (b) plot the simulated absorptance spectra as a 2-dimensional contour plots for the 1 $\mu$m and

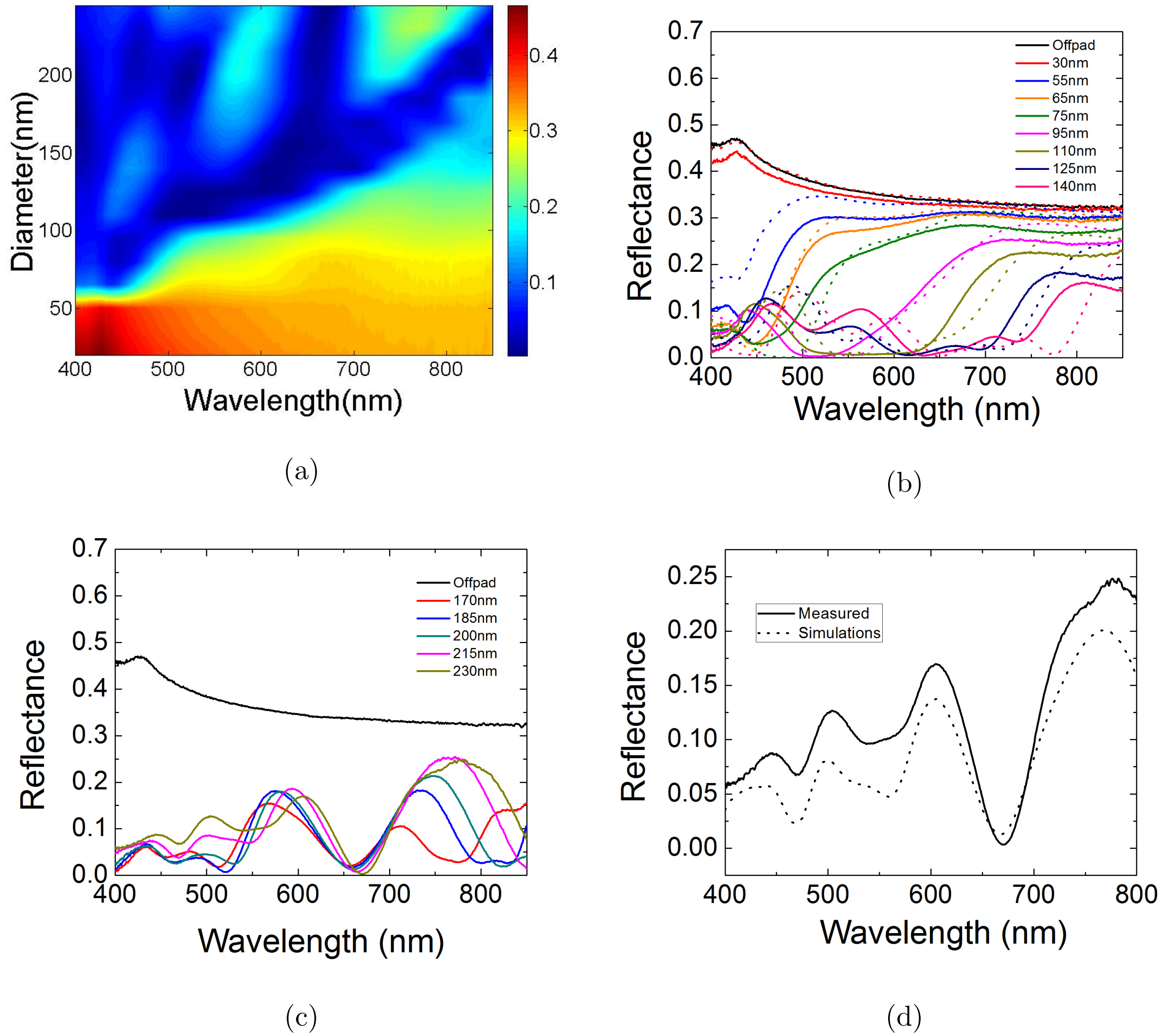


Figure 5.2: Reflectance spectra from 1 $\mu$m long GaAs nanowires spaced 400 nm from each other (a) 3-D contour plot of reflections for all the diameters (b) 2-D plot of reflections from 30 nm to 140 nm diameters (c) Reflections from 140 nm to 260 nm diameters (d) FDTD simulations matching the reflection spectrum of nanowires of 230 nm diameters.

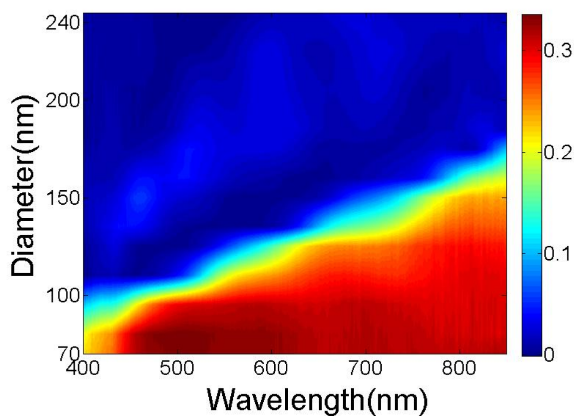


(a)

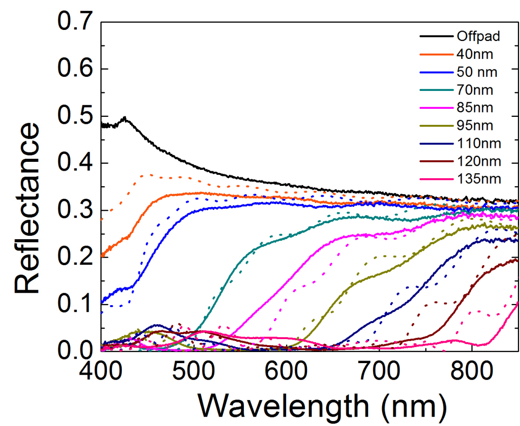


(b)

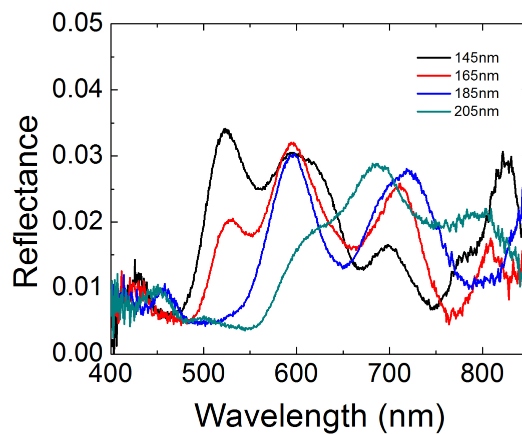


(c)

Figure 5.3: Reflectance spectra from 2.2$\mu$m long GaAs nanowires spaced 400 nm from each other (a) 3-D contour plot of reflections for all the diameters (b) 2-D plot of reflections from 40 nm to 135 nm diameters (c) Reflections from 145 nm to 205 nm diameters.

2.2 $\mu$m long nanowires, respectively, with a fixed pitch of 400 nm and various diameters (corresponding to figure 5.2 and 5.3, respectively). In both cases, a strong absorption peak is clearly observed that shifts towards longer wavelength with increasing nanowire diameter to 175 nm. This shift in the absorption peak corresponds to the red-shift of the reflectance spectra in figures 5.2 and 5.3. As the diameter is increased to 200 nm, the peak is not observed and the absorption is lower in the 500 nm-800 nm wavelength range as compared to the smaller diameters. The reduced absorption results in the strong F-P peaks observed for the larger diameter nanowires. For the diameter of 250 nm, a new absorption peak appears clearly at a shorter wavelength. For the smaller diameters, at wavelengths longer than the absorption peak, the absorption decreases quickly within the nanowires, and a large part of the reflectance then comes from the GaAs substrate. For the longer length of 2.2 $\mu$m, the same absorption peaks are observed centered at the similar wavelength as for the 1 $\mu$m length. The absorption peaks are broadened for the longer length which is expected from the exponential dependence of Lambert-Beer′s Law allowing photons around the peak to have a better chance to be absorbed as the length is increased. Further, the absorption on the shorter wavelength side increases. Previously, it has been theoretically suggested that specific diameters in III-V nanowires have the highest efficiency for solar cells. The reason becomes clear from figures 5.2 to 5.4. It is the excitation of the optical mode resulting in enhanced absorption peaks along with the exponential dependence of Lambert-Beer′s Law which allows the broadening of the absorptance making the nanowires efficient solar absorbers. Alternatively, by using shorter lengths, one can also fabricate narrowband spectral photodetectors for applications in multi-spectral imaging.

Knowing the absorption profile of the nanowires as shown in figure 5.4, the absorption profile of nanowires can be designed for broadband absorption by using the range where the $HE_{11}$ and $HE_{12}$ modes excite. From the figure 5.4, it is shown that the nanowires start to excite $HE_{11}$ at ∼60 nm diameter and stop at ∼175 nm diameter. $HE_{12}$ modes start

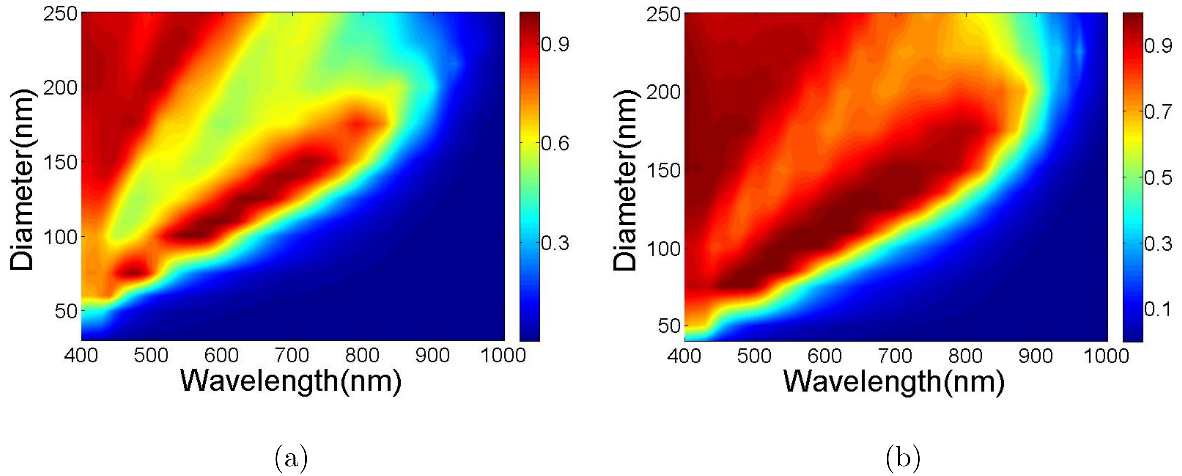


Figure 5.4: Absorptance contour plot for (a) 1 $\mu$m long GaAs nanowires and (b) 2.2 $\mu$m long nanowires spaced 400 nm.

to excite at $\sim$ 120 nm diameter and keep exciting till the band edge for diameters larger than 250 nm. Thus the diameter range to get the broadband absorption should be around 175 nm where $HE_{11}$ mode is just at the band edge and $HE_{12}$ helps to absorb at shorter wavelengths. This is the first time the design has been proposed for the nanowires.

### 5.2.2 Amorphous Silicon Nanowires

The ability of a-Si to be deposited uniformly on a large variety of surfaces at low cost makes it a favorite material for commercial optoelectronics applications for mass production. Being a direct band gap material makes it the low-cost alternative to the III-V materials. Further, the low-temperature deposition of a-Si makes it a good candidate for the designs earlier proposed for crystalline silicon nanowires. However, as it is optically different than silicon it is necessary to understand its waveguiding properties to engineer its properties for all those applications. Here, we fabricate the a-Si nanowires to study their reflection, transmission and reflection properties experimentally.

Figure 5.6 shows the reflection and transmission spectra and figure 5.7 shows the absorp-

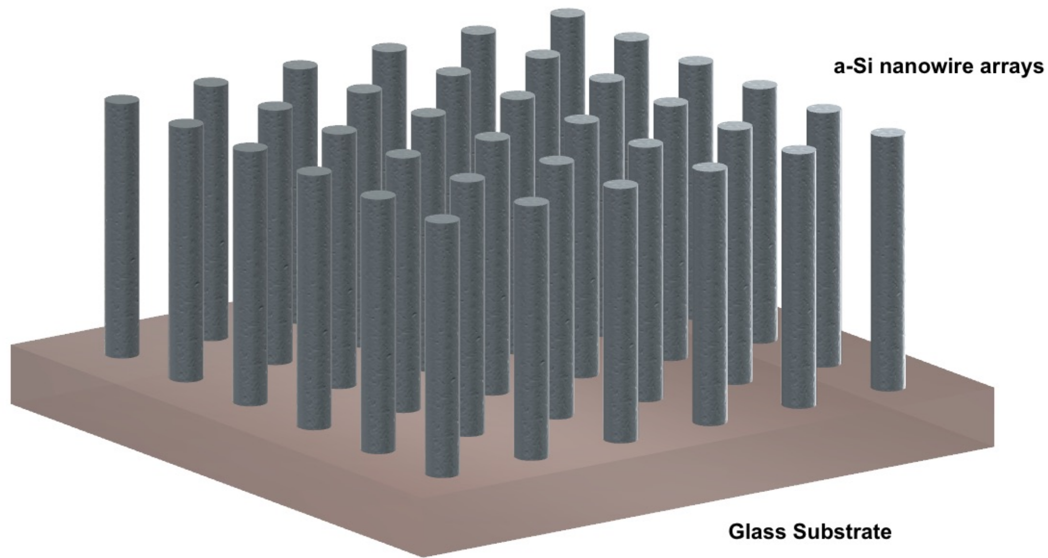


Figure 5.5: Schematic of the aSi nanowires on glass

tion spectra of the a-Si sample having 100 nm to 250 nm diameters, similar to the ones discussed in the simulation studies in chapter 3 and were fabricated in chapter 4. The nanowire samples were etched down from 535 nm thick film all the way down to the glass substrate as shown in figure 5.5. Since the nanowires are on the glass substrate, we can also measure the transmission and hence the absorption can be calculated directly. For 100 nm diameter and pitch 400 nm(Figure 5.6a) , the nanowire on glass sample exhibits less than 10% reflectance over the visible range and is below 5% for wavelengths smaller than 600 nm, a result similar to those observed for Si nanowires embedded in PDMS layers [121]. In the transmission spectrum, a sharp dip is observed at 600 nm. Optical transmission approaches 90% for wavelengths greater than this dip. A single absorption peak centered at 600 nm is observed in figure 5.7a which is complementary to the dip in the transmission spectrum in figure 5.6a. The absorption spectrum reveals that 90% of

incoming photons at the resonant wavelength, $\lambda_{res}$, are absorbed even for as short a length as 535 nm. With a fill factor, defined as $\pi R^2/P^2$ where R is the radius (50 nm) and P is the pitch (400 nm), of only 5%, the remarkable resonant absorption characteristics of the nano- wire array at the resonance are clear. The absorption peak in the simulations is slightly higher and narrower than those obtained experimentally which could be due to the small variations in the diameter of the fabricated nanowires in the array. If one compares these results with silicon nanowires embedded in PDMS [122], the filter response is very similar. Comparatively, the absorption is higher in a-Si nanowires even though the length of the nanowires is nearly half of that of the silicon nanowires. This is due to the higher density of a-Si nanowires and also higher absorption coefficient for the a-Si thin film as compared to crystalline silicon in the measured wavelength span. The resonance wavelength, $\lambda_{res}$, is also higher than that for the crystalline silicon of the same diameter by ~30 nm. The ratio of the resonance wavelengths for the two materials corresponds to the ratio of the real part of the refractive indices of the semiconductors, a fact observed in literature in other semiconductor nanowires of the same diameter [20, 21, 123]. Above $\lambda_{res}$, the absorption drops very quickly, increasing the transparency of the nanowires. Thus, such nanowires are good absorbers only at wavelengths where the resonant optical modes are excited.

The absorption spectra for the 150 nm, 200 nm and 250 nm diameter of nanowires freely standing on glass are quite different as compared to the 100 nm diameter where a single absorption peak was observed corresponding to the $HE_{11}$ mode. Figures 5.6 (b), (c) and (d) show the reflectance and transmission spectra for these diameters and figures 5.7 (b), (c) and (d) show the corresponding absorption spectra. A lot more spectral features are observed in these compared to 100 nm. These could be due to resonant excitations of higher order leaky waveguide modes or even due to F-P longitudinal modes. Simulated spectra for nanowires on the glass substrate and semi-infinite nanowires were calculated

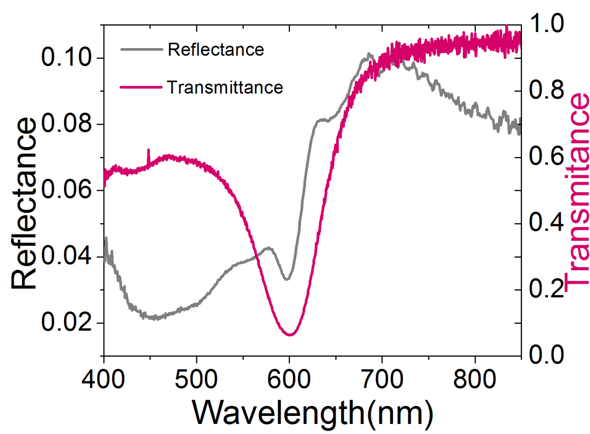


(a) 100 nm

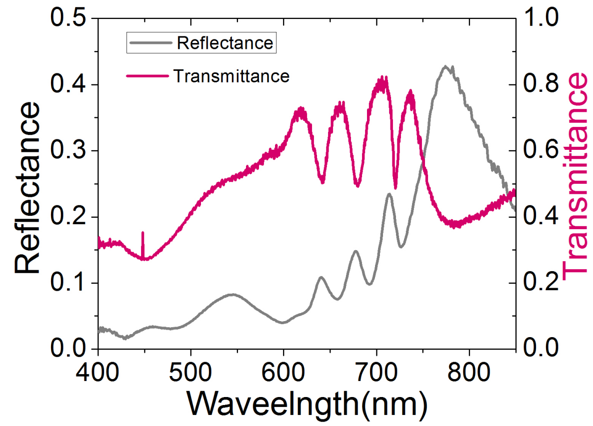


(b) 150 nm

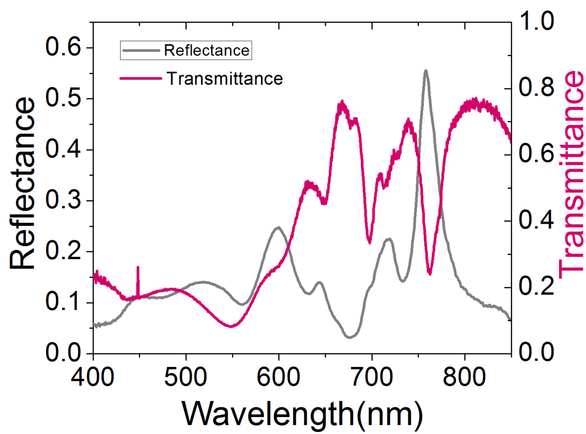


(c) 200 nm

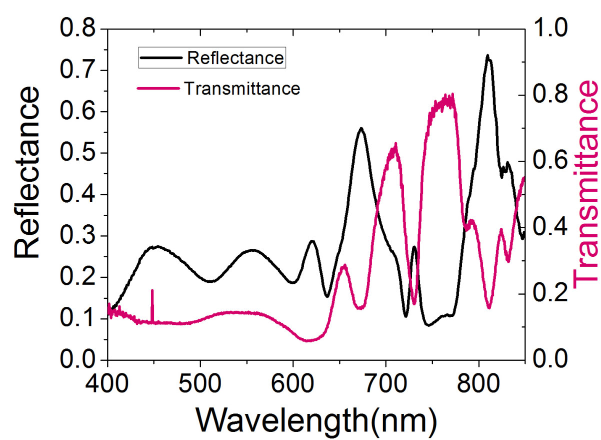


(d) 250 nm

Figure 5.6: Reflection and transmission spectra of a-Si nanowires for four diameters 100 nm, 150 nm, 200 nm and 250 nm measured using the home made optical setup.

and are plotted in figure 5.7. The spectral features for wavelengths longer than 600 nm vanish completely when the cavity is removed as shown in figure 5.7, showing those features were due to the reflections from the nanowires-glass interface. For the 100 nm diameter studied previously, $HE_{11}$ mode was excited at 600 nm wavelength exactly as predicted by simulations.

For 150 nm diameters, it is expected that this resonance peak red shifts to wavelengths larger than 600 nm. However, there is no such peak above 600 nm in figures 5.7b, we can expect that the first order mode must be excited beyond the band edge (∼727 nm) of a-Si. The first order mode for this diameter is expected at a wavelength of 800 nm. However, there is ∼70% absorption at ∼ 450 nm wavelength for both nanowires on glass (experimental and simulations) and semi-infinite nanowires. The absorption is slightly higher for finite structure due to the presence of the minor reflections at the nanowire-glass interface due to the refractive index mismatch.The increased absorption at 450 nm could arise due to the excitation of higher order modes, specifically $HE_{12}$. The four absorption peaks at 600 nm, 640 nm, 680 nm and 720 nm are not present in the semi-infinite nanowires simulations showing that they are not dependent on the radial structure of the nanowires. They arise due to the excitation of longitudinal modes resulting from F-P resonances within the nanowires. There should be no absorption expected beyond the band gap (∼ 727 nm) but high absorption peaks are observed for diameters 150 - 250 nm at wavelengths around 800 nm. This is due to the presence of aluminum mask on the top of these nanowires [124]. The light reflects back and forth between the nanowire/mask interface and nanowires-glass interface, and gets absorbed within the mask due to excitation of the cavity created plasmonic mode as will be shown in next sections. This was confirmed by removing the mask in the simulations, where certain peaks were missing at longer wavelengths as shown in figure 5.8. The mask does play a role in enhancing the F-P peaks also as the reflection at nanowire-air interface increases and results in increased absorption within the nanowires.

Thus, the aluminum mask is beneficial in increasing the absorption within the nanowires and need not be removed post fabrication. In future, this can facilitate making contacts with the nanowires in a self-aligned fabrication process.

For the 200 nm diameter, the $HE_{12}$ mode is excited at ∼550 nm and a new peak is excited at a shorter wavelength of ∼450 nm. As the diameter of the nanowires is further increased, higher order modes will be supported and the peak at ∼450 nm could be due to the excitation of $HE_{13}$ and other higher order modes or due to the larger absorption coefficient at this wavelength [125]. The F-P resonances were excited between 620 nm and 726 nm showing multiple peaks in A, R, and T in this wavelength range. For diameter 250 nm, an absorption peak is observed at 620 nm primarily due to the excitation of $HE_{12}$ mode. Also, the peak is split into two due to the presence of F-P modes since there is only a single peak is observed in semi-infinite simulations. Another peak is observed at a shorter wavelength of ∼525 nm due to the excitation of higher order modes. F-P resonances dominate the absorption spectrum from 620 nm to 720 nm. Also, the nanowires become multimode at these diameters and there are other higher order modes that can be observed along the length of the nanowire as shown in figure 3.5 d and e.

### 5.2.3 Structural Colors

As discussed in the previous section, the reflected colors represent the optical response of the nanowires in the visible range. The reflected hue of nanowire array represents the wavelengths the wavelengths that are dominantly reflecting back. The reflected color could be due to the primary wavelength region like yellow, red or blue or combination of different wavelengths making the secondary colors like purple, green or orange depending on the reflection spectrum. In figure 5.9 the reflected colors for GaAs, Silicon, and a-Si nanowires are shown from the smallest to the largest diameters. For all materials, it can

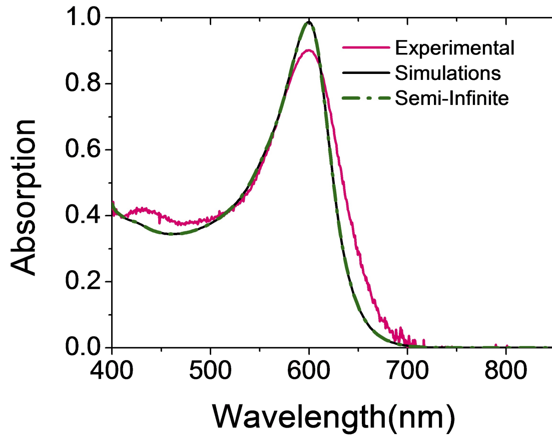


(a) 100 nm

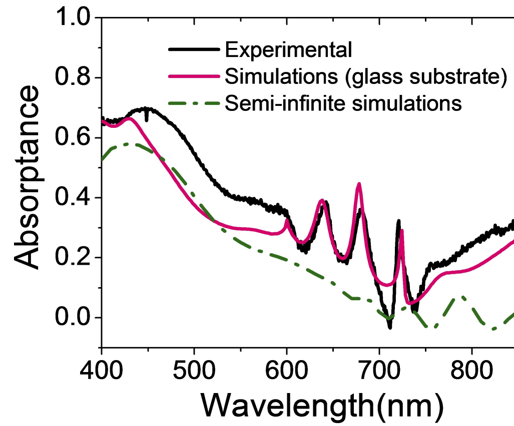


(b) 150 nm

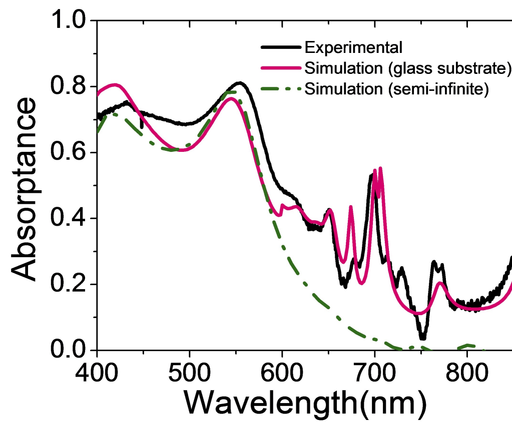


(c) 200 nm

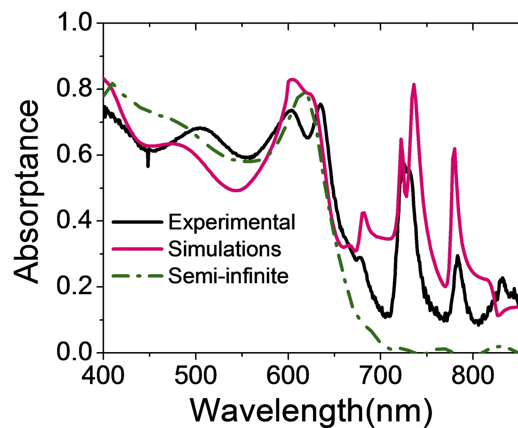


(d) 250 nm

Figure 5.7: The absorption spectra of a-Si nanowires for four given diameters,. Also, the simulated spectra for semi-infinite and nanowires on glass setup are also shown for each diameter.

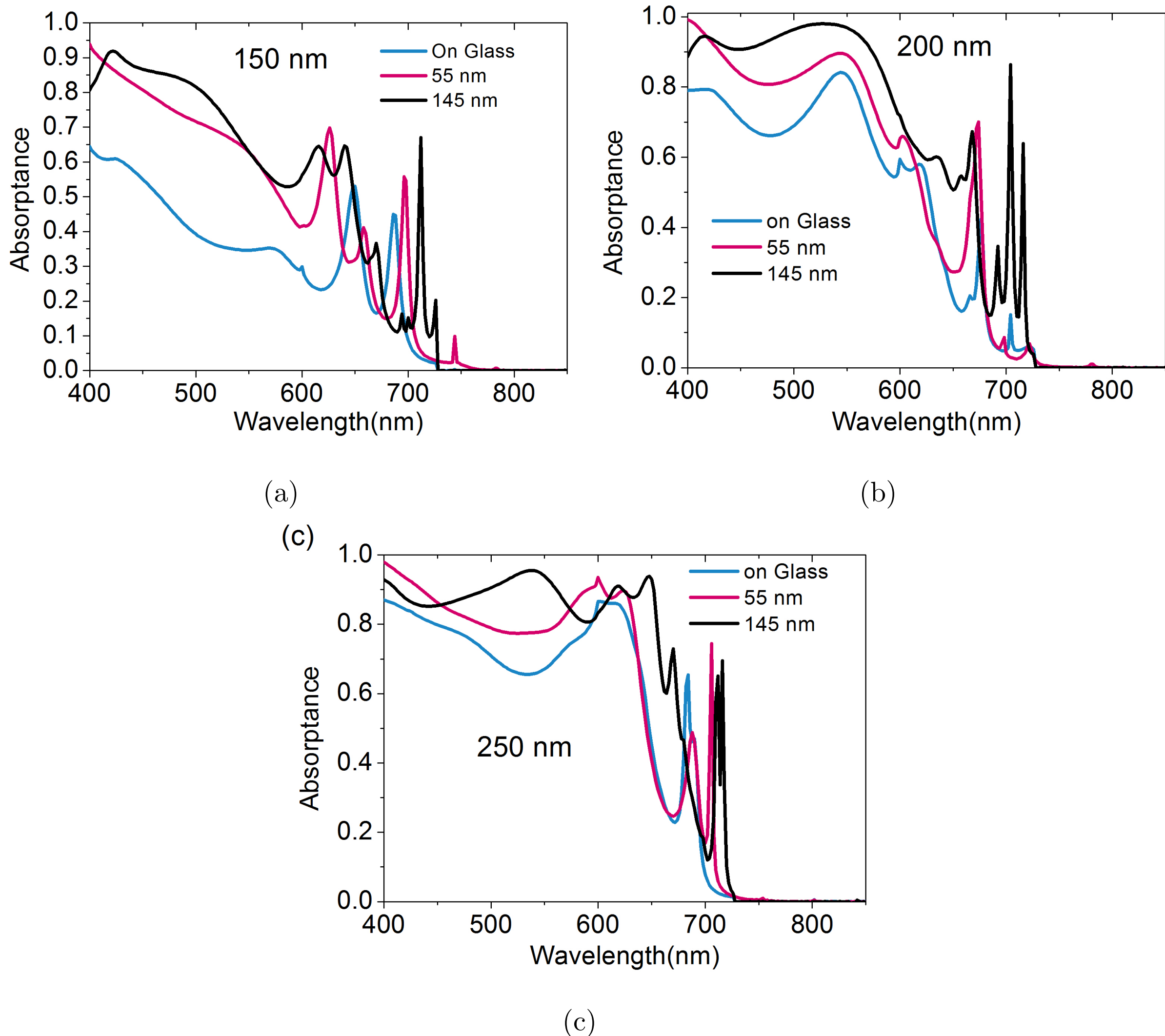


(a)

(b)

(c)

Figure 5.8: Absorptance in bare nanowires for diameters (a) 150 nm (b) 200 nm and (c) 250 nm showing there is no absorption beyond the band gap in the absence of mask. Also, the peak intensities and F-P positions change due to the absence of mask.

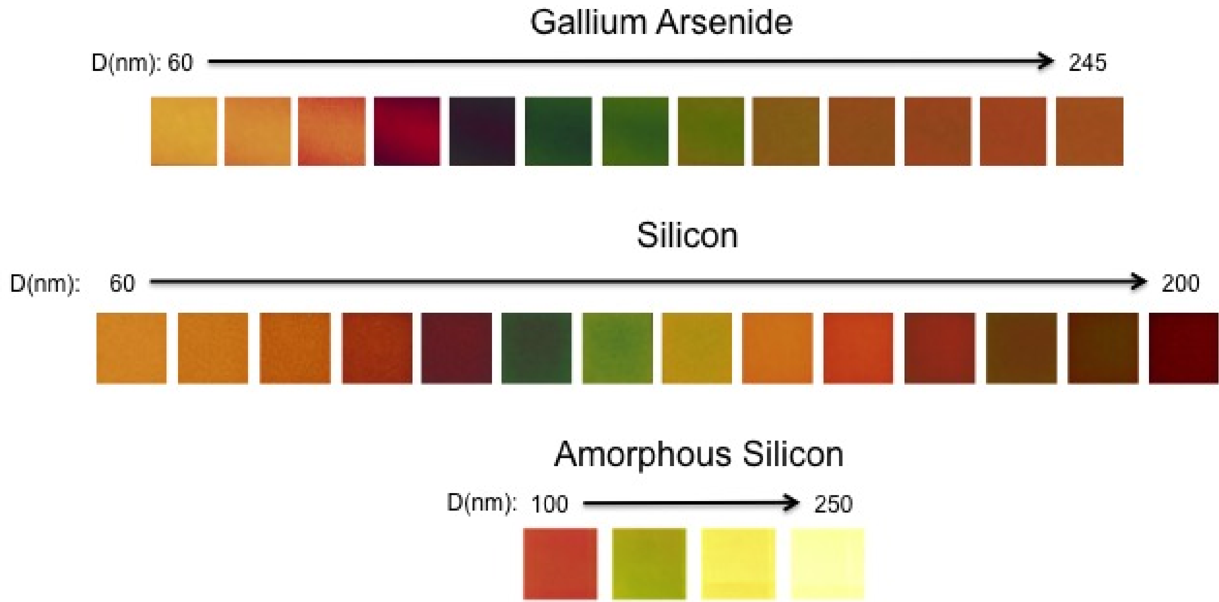


Figure 5.9: Reflection Colors of GaAs, Silicon and a-Si nanowires for different diameters

be seen that the colors are dominated by red/orange hue for the small diameters due to the high absorption in the blue region due to the resonant $HE_{11}$ modes. While moving towards larger diameters the dark red region starts to show indicating the green is getting completely absorbed and then green starts to dominate in reflection as the resonant modes start to shift towards the red region. Eventually, the $HE_{11}$ modes move out of the visible region and higher order modes start to appear in the short wavelengths in the blue region, making red/orange dominant again. This pattern is similar for GaAs and Silicon nanowires and a-Si also shows a similar trend towards it. In the future section, the colors will be shown to show the effect of the change in parameters like pitches, disorder or effect of thin-film integration.

## 5.3 Near Field Coupling: Comparison of Silicon, aSi and GaAs Nanowires

We already tested the near field coupling between semiconductor nanowires using simulations where the pitch was varied while keeping the diameter constant and the results are plotted in section 3.3. It was seen that for the GaAs resonance wavelength shifts very weakly even over large changes in the pitch as opposed to the results for silicon nanowires. These simulations clearly show that the absorption peaks arise due to the optical modes of the individual nanowires as has been suggested previously. This phenomenon was confirmed experimentally by fabricating a sample where the pitch was varied while keeping the diameter and length fixed at 115 nm and 1.6 $\mu$m, respectively. The results are plotted in figure 5.10. The simulated reflectance is also plotted as dotted lines. As can be seen, the reflectance minimum between 550 and 700 nm, due to the $HE_{11}$ mode, shifts very weakly even over large changes of pitch. The results agree well with simulations except for slightly higher predicted reflectance away from the absorption peaks. The small discrepancy could be due to the roughness of the bottom GaAs substrate between the nanowires after etching making the light scatter rather than reflect back. These results experimentally demonstrate that indeed the GaAs nanowires are acting as individual waveguides with negligible coupling between them in an array over the range of pitches studied.

Similar tests were performed for silicon nanowires as they showed near-field coupling in simulation studies and also the mode specificity increases due to low absorption in the nanowires. Pitches from 400 nm to 800 nm were fabricated at 85 nm diameter and reflection measurements were taken as shown in figure 5.11a. The absorption decreases while the pitch increases as the nanowire density decreases. As observed in simulation studies, the red-shift in resonant wavelength with the change in pitch can be seen in the experimental

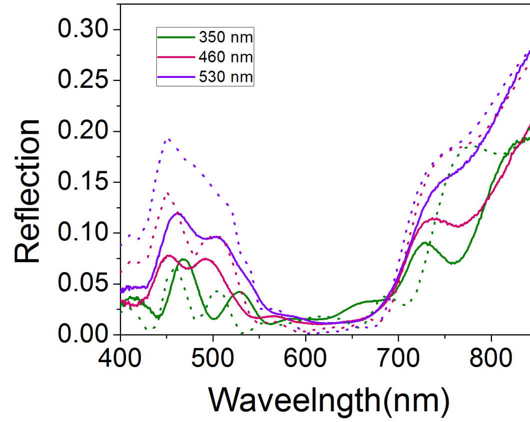


Figure 5.10: Experimental reflection measurements of 115 nm diameter nanowires with three different pitches and 1.6 $\mu$m length. FDTD simulations of reflectance of the same three pitches is also shown in dotted lines of same color.

studies as well. This is due to the excitation of Bloch photonic crystal modes when the nanowires are closely spaced and mode to larger wavelengths when the spacing increases. The shift is due to the reasons explained in chapter 2 and 3. The FDTD simulations were performed for the nanowires on the silicon substrate to replicate the results shown in experimental data. Figure 5.11b shows the simulated results for the nanowires having same diameter, pitches, and length. As opposed to experimental study where the red shift continues till 800 nm pitch, in simulation studies, the red shift stops at 600 nm. This anomaly could be due to the variation in diameters for experimental data. As shown in figure 5.13b, for 700 and 800 nm pitches the diameters are $\sim$ 2-3 nm larger than other pitches. Also, the reflection dip for 400 nm pitch is much wider than other pitches for both experimental and simulation spectra owing to increased confinement due to large fill fraction.

Figure 5.12 shows the microscope images of different nanowire arrays as the pitch is changed for the same diameter. For silicon nanowires, the color hue changes abruptly as

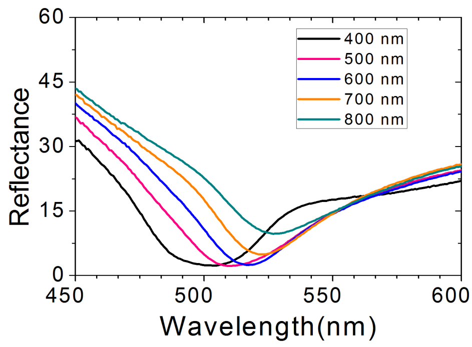


(a)

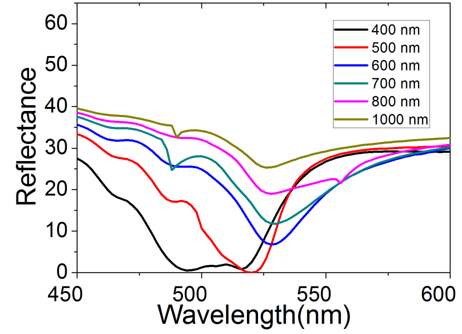


(b)

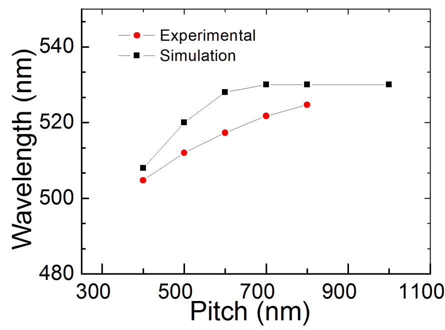


(c)

Figure 5.11: (a)Reflection measurements of silicon nanowires of 85 nm diameters and 700 nm length at different pitches given in the figure.(b) Simulated reflectance spectra of silicon nanowires with substrate at the bottom and dimensions same as used for experimental study (c) The comparison of shift in resonant modes with the change in pitch for experiment and simulation results.

the pitch is changed to 700 nm and then only degrades in luminosity in HSL space as the pitch is further increased. On the other hand, there is a decrease in luminosity for GaAs and a-Si nanowires but the hue remains the same. These images again suggest the silicon nanowires arrays are coupled while GaAs and a-Si nanowires act as individual waveguides.

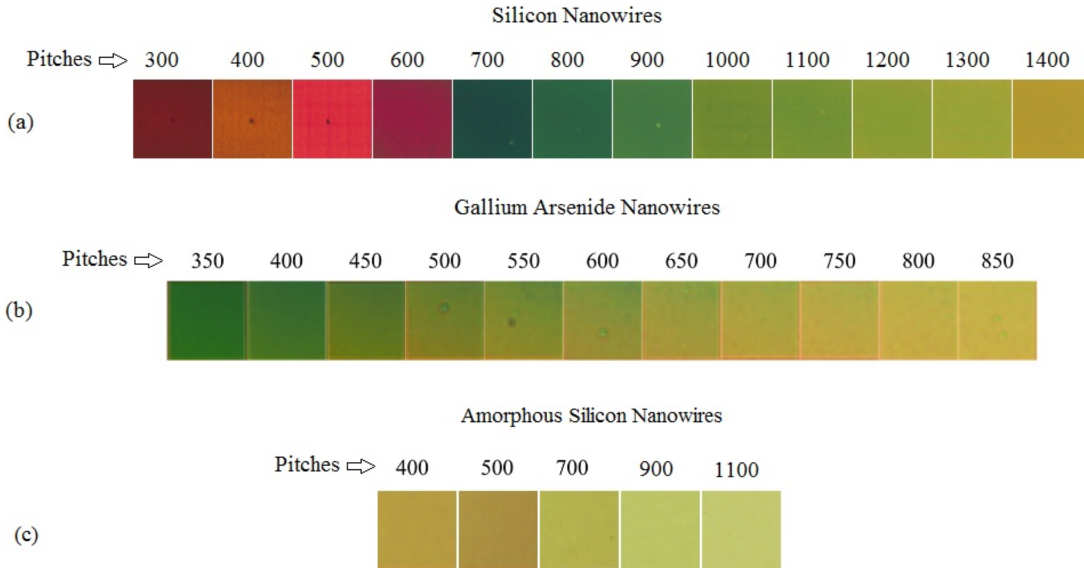


Figure 5.12: Reflected colors from (a) GaAS (b) Silicon and (c) a-Si nanowires for different pitches

## 5.4 Silicon Nanowires - The Comparison Between Ordered and Disordered Nanowires

We have observed the near field coupling effect in the Silicon nanowires in the previous section. In order to see the strength and also to see whether it is a long range order or short range order, we designed an experiment to create randomly arranged nanowire sample to show the presence of photonic crystal modes in the silicon nanowires. The idea is to break the periodic boundary conditions of the nanowires and compare their reflectance

with ordered silicon nanowires to see the difference. The use of electron beam lithography enables us the flexibility to create random as well-ordered patterns. However, the truly random pattern needs to be made manually as the Raith CAD software does not allow this capability. For creating random patterns, the individual elements of circular patterns were moved into random directions, starting from the ordered pattern. Despite being a laborious process, it ensures the randomness in the nanowire pattern remains high. On the other hand, designing ordered patterns is the inherent capability of RAITH150-two CAD software. The etching process of silicon nanowires is well established [70] and is also mentioned in Chapter 4. Figure 5.13a shows the side-view SEM image of the disordered nanowires showing the presence of truly random structures. The ordered arrays were fabricated right next to the disordered arrays, hence the length of both the samples is exactly the same. To strengthen this study, the nanowire samples of increasing pitch and same diameter were also introduced. The change in periodic boundary conditions for photonic crystal modes would also be observed when the nanowires are moved far apart in an array. The diameter chosen for this study was 85 nm and to ensure the consistency in results, the diameter distribution of the nanowires for disordered and ordered samples was done using image processing software ImageJ for the image magnification of 10,000 x . Figure 5.13b shows that the diameters of both ordered and disordered nanowire arrays lie within the same range. The nanowire count decreases with the increase in pitch as the fill fraction decreases.

Reflection measurements were chosen for this study since the modal excitations in the silicon nanowires could also be observed from the reflection properties as shown in previous studies [126]. Thus, the tedious procedure to remove substrate using wet etching can be avoided in this experiment. F- 40 Filmetrics profilometer was chosen to measure the reflections from the sample at different magnifications.

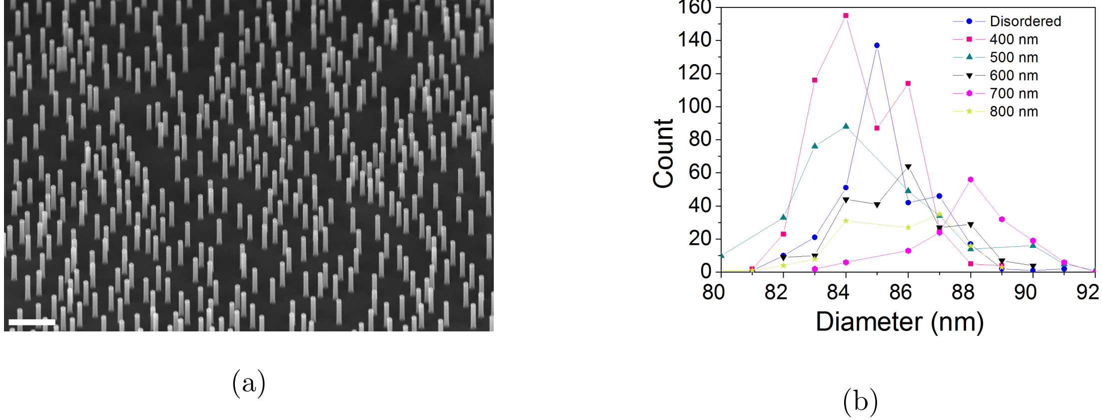


(a)

(b)

Figure 5.13: (a) Sideview (45°-tilt) SEM image of disordered silicon nanowires (b) the diameter distribution of disordered nanowires and ordered nanowires at different pitches

### 5.4.1 Reflection for Ordered vs Disordered Nanowires

The reflectance was performed on the ordered and disordered samples at 10× magnification with 20 $\mu$m spot size. The numerical aperture at this magnification is low enough to not let the polarization of $E_z$ component of the electrical field, which can change the absorption profile. Reflectance from the silicon substrate is also plotted for comparison. The reflectance measurements were performed at different spots on the both samples to ensure the consistency of the measurement, which we will discuss in next section. A sample reflectance from ordered and disordered arrays is shown in figure 5.14. The reflectance dip indicates the excitation of resonance modes within the nanowires. As expected, the resonant excitations in ordered and disordered nanowires are 30 nm apart despite having same diameters for both the arrays. This is due to the photonic crystal modes condition being different in ordered and disordered nanowires. We mark the resonant dip for ordered nanowires as P1 and for disordered nanowires as P2. There is another dip P3 at longer wavelengths which is observed only in ordered nanowires. This dip could be due to the presence of mask which excites cavity created plasmonic modes and would be highly de-

pendent on the periodicity of the nanowires. This is studied in a separate experiment. P1 is at wavelength 30 nm shorter than P2 due to the fact that the Bloch photonic modes are being excited in the ordered arrangement with the negative value of $\zeta_\circ$. Given the slight difference in the diameter distribution between ordered and disordered nanowires as shown in Figure 5.13b, one should expect a slight shift of 4 nm in the resonant wavelength. The shift, however, is 30 nm and is validated by the photonic band-gap mode theory [22]. In addition, the width of the absorption dip of the ordered silicon nanowires is slightly larger than the disordered nanowires suggesting that they are absorbing the photons more strongly than the disordered nanowires. This is also supported by the theory that $\zeta_\circ$ becomes more negative when the confinement of the optical modes increases and a blue shift is achieved.

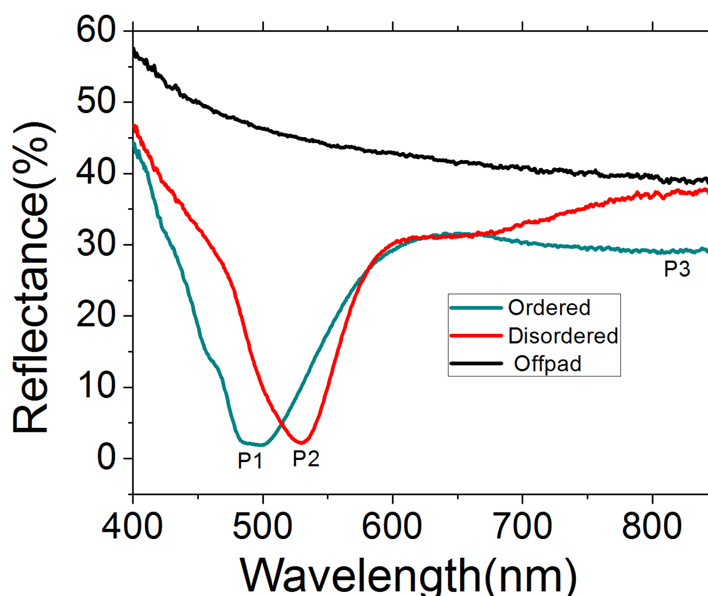


Figure 5.14: Reflection measurements of ordered (green) and disordered (red) nanowires. The reflection from bulk silicon is also plotted for comparison.

To confirm the consistency of the measurements, the reflectance at different parts of nanowires are performed at 40× magnification with 7$\mu$m spot-size. Figure 5.15 shows the color images of the nanowires. The spots where the reflection measurements are taken are labeled in the microscopic images and their corresponding reflection measurements are also shown in the figure. For ordered nanowires, the resonant modes are almost the same except for the slight variation in measurement spots closer to the edges owing to the breakdown of the long-range order at the boundaries. Measurements spots 2 and 4, which are closer to the edge compared to 1 and 3, having coinciding reflections spectra and slightly red-shifted compared to the other two. For disordered nanowires, while measuring reflection at different spots there is no significant shift in the position of the resonance dip, however, the reflectance minima change with the change in density of the nanowires. The reduction in reflection with the increase in nanowires density is intuitive as the higher fill fraction leads to higher absorption in nanowires. The short range ordered reflection measurement at spot 6 shows no variation compared to other disordered measurements confirming the theory that it is due to the change in excitation conditions of photonic crystal modes due to the change in periodic boundary conditions over the array.

In summary, the experimental verification of Bloch modes in ordered silicon nanowires of 400 nm spacings is done by showing the blue shift of resonance wavelength by $\sim$ 30 nm compared to disordered nanowires. The negative value of Rayleigh identity $\zeta_\circ$ is attributed to this shift. Also, the absorption peaks are broader for the ordered nanowires compared to the disordered ones. This study confirms with our previous analysis of near-field coupling between nanowires with varying pitches and shows that the Bloch conditions change when the periodicity is changed within the nanowires. These results can be useful in dictating nanowire designs in photodetectors, spectral filters or photovoltaics.

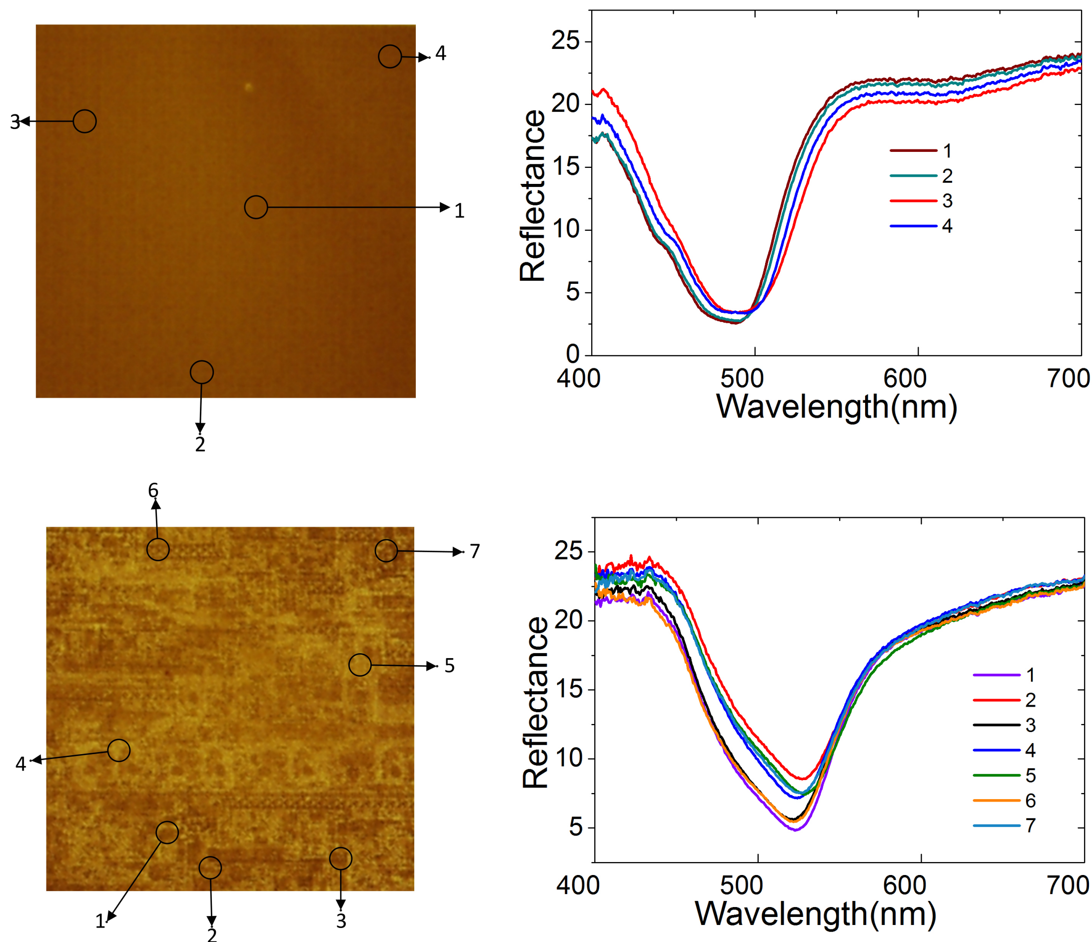

Figure 5.15: Side-view SEM image of GaN nanowires for three diameters (a) 100 nm (b) 200 nm (c) 260 nm

## 5.5 Length Analysis of Nanowires

It was discussed in chapter 3 using semi-infinite nanowires that irrespective of the material properties the nanowire behave in a similar way when it comes to the development of radial modes inside the nanowires. The nanowire′s waveguiding is highly dominated by scattering until a length of 150 nm after which the mode fully develops. We verified this property of nanowires by etching silicon nanowires to different etch depths. The reflectance was measured after every etch. The ICP-RIE etching capability was used to control the length

of nanowires. The etching was stopped every 20 seconds to approximate etch depth of 100 nm and the sample was cleaned and measured each time before the next etching step. The procedure was performed seven times and the etch length was verified using Dektak surface profilometer. The length was also verified using side-view SEM at the end of the last etch showing the final length of the nanowire around 670 nm.

The reflection measurements for the all the lengths are shown in a single plot in figure 5.16a. The diameter chosen was 85 nm and pitch 700 nm. The reflection spectra were also verified using simulation using similar conditions and parameters as the experimental values and shown in figure 5.16b. The presence of F-P resonances due to the substrate, however, affects the absorption characteristics of the mode and does not confirm well with the semi-infinite simulation studies. The nanowires support a single $HE_{11}$ mode in the visible wavelength region and the resonant wavelength is at  500 nm, and thus, easily measured. The nanowires were arranged in a square lattice with spacing between the nanowires to be 600 nm. At this spacing, the nanowires act as individual waveguides with no near-field coupling between them. The length was varied from 50 nm to 700 nm in the study. Similar behavior to semi-infinitely long nanowires (Chapter 3) is observed. For lengths smaller than 100 nm, no clear absorption peak is seen while it starts to develop for lengths longer than 100 nm and is clearly observed even for the length of 150 nm. Although, due to the presence of substrate below and double pass of light, the absorption is significantly increased. Also, due to the presence of F-P cavities in the presence of substrate the longitudinal modes dominate causing the off-resonance dips in reflectance spectra. The reflection dip stabilizes when the mode starts to dominate above 200 nm of length. These simulations (Figure 5.16 a and b) suggest that even nanowires as short as 150 nm behave as optical waveguides with the optical mode properties dominating the scattering from the nanowire interfaces and is the first study of its kind.

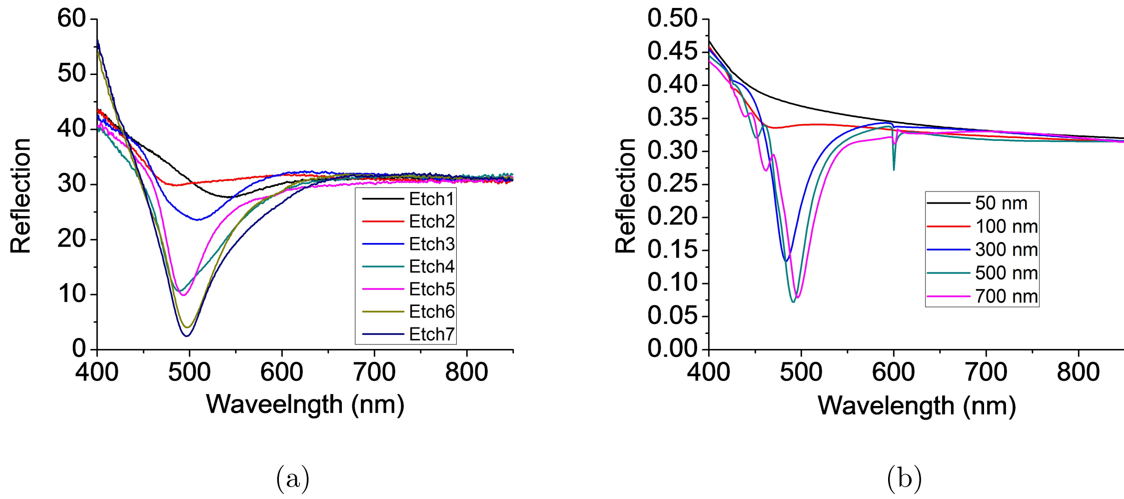


Figure 5.16: (a) Reflection of nanowire arrays at different etch depths at 700 nm pitch and 85 nm diameter (b) Simulated reflections from the nanowires with the same diameter and pitch at similar etch depths.

## 5.6 Tapering of the Nanowires

Tapering of the nanowires is an important design in the fabrication of nanowires as the ICP-RIE technique has shown capabilities to control the shapes and longitudinal profiles of the nanowires as was shown in chapter 4. Tapered structures have an advantage over cylindrical nanowires as they show enhanced absorption by exciting multiple in the continuum of radii [127] modes. They also provide better impedance matching than cylindrical nanowires by gradually reducing the refractive index, achieving higher absorption than their cylindrical counterparts. Here, the capability to fabricate tapered nanostructures is shown for GaAS and silicon nanowires and their absorption abilities are demonstrated. Figure 5.17 show the different tapered profiles on the GaAs nanowires using variations in masks. Figure 5.17(a) shows the bottle shaped tapers showing two diameters nanowires joined together. This feature was formed when the Cr mask starts to erode laterally and the anisotropic

nature of ICP starts etching the top exposed area at higher etch rates than the side walls. Figures 5.17(b)(c) and (d) show profiles when the moderately selective titanium (Ti) mask starts to erode gradually along with the anisotropic etching. The etch rate of Ti mask is slightly higher than Cr mask in $Cl_2$ chemistry, thus it may generate features shown in 5.17(a). However, it can show perfectly tapered chemistry without changing the etching recipe.

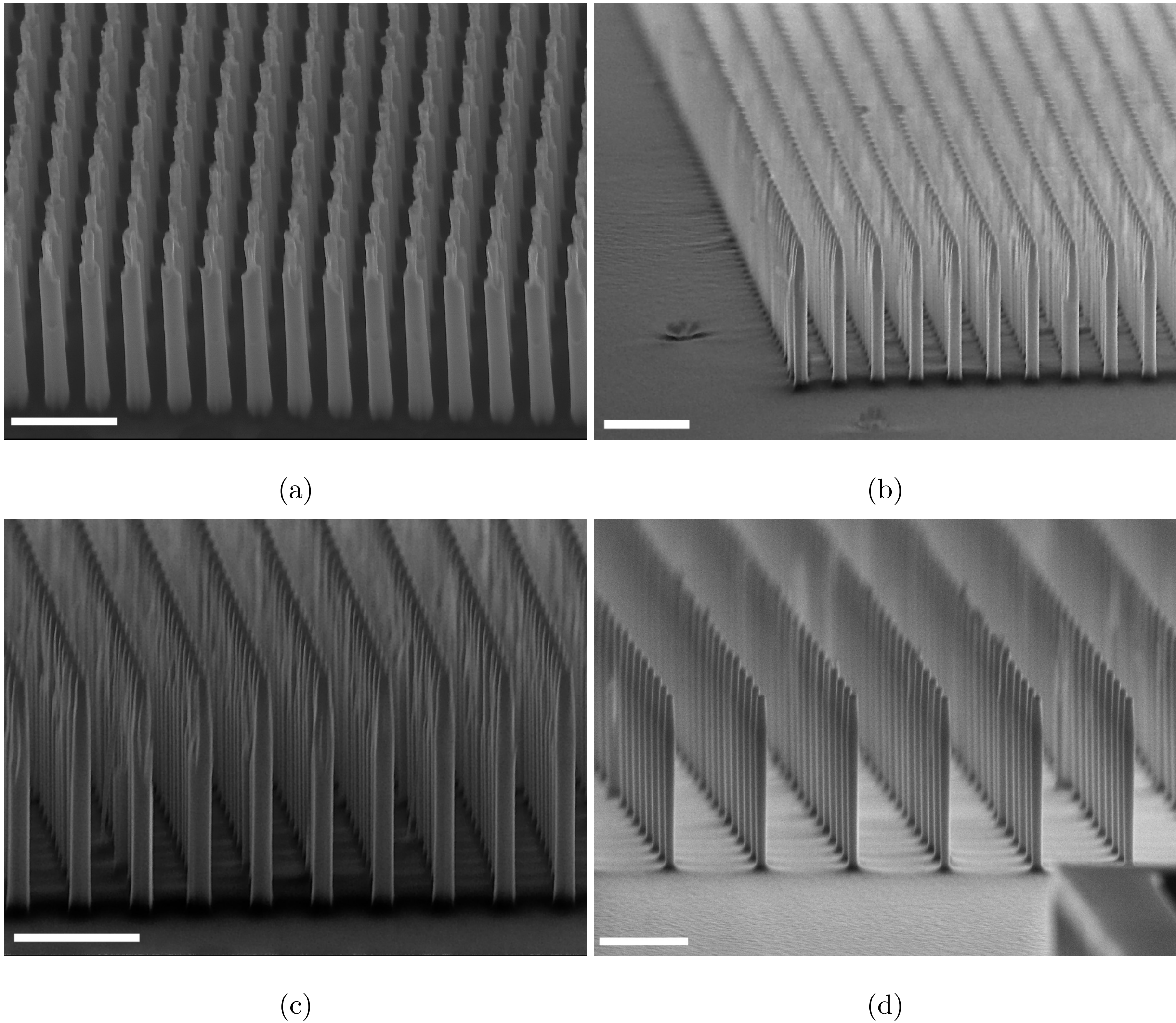

(a) (b)

(c) (d)

Figure 5.17: Tapered profiles of GaAs using different dry etching parameters and hard masks.

To demonstrate superior absorption abilities of tapered GaAs nanowire, nanowire arrays with 100 nm diameter and pitches ranging from 300 nm to 800 nm were fabricated. The reflections(R) were measured for these nanowires using F-40 Filmetrics and absorption was calculated using 1-R. Figure shows the broadband absorption for the all the pitches. Interestingly despite reducing the fill fraction drastically, the tapered nanowires structures have absorption above 80%. These structures could be the better candidates than cylindrical nanowires for photovoltaic applications.

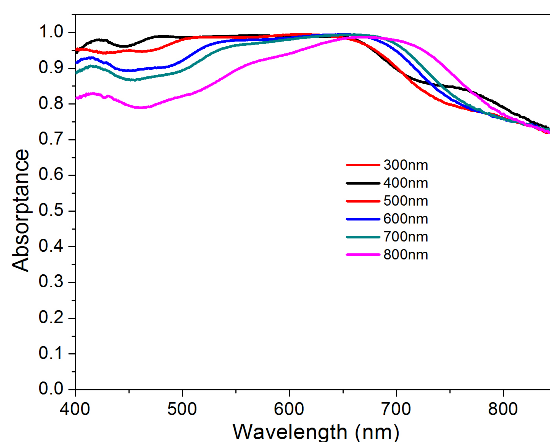


Figure 5.18: Absorption spectra of tapered GaAs Nanowires for 100 nm base diameter and different pitches.

Unlike GaAs nanowires, tapered profiles of silicon nanowires were achieved by modifying the etching recipe as the passivation layer is used to control their sidewall profiles. As mentioned in chapter 4, the passivation gas $C_4H_8$ was reduced to increase sidewall etching to achieve tapered profiles. The forward power was also increased to increase mask etching. Silicon tapering was a success yet mask still remained intact to create mushroom structures as shown in figure 5.19a. The reflection was measured for the tapered silicon nanowires and compared with cylindrical nanowires as shown in figure 5.19b. As expected, the tapered nanowires show much less reflection in comparison except for the resonant wavelength.

Cylindrical nanowire arrays provide very high absorption at resonant wavelengths while absorbing less away from it. On the other hand, the tapered nanowires provide a broadband absorption at the expense of reducing the peak absorptions at the resonance wavelength. Thus, the light was tightly confined to show higher absorption in cylindrical nanowire arrays. A peak at ∼490 nm may be due to the reflection from the top of the mask, which has a slightly smaller radius than the base diameter as shown in figure 5.19a.

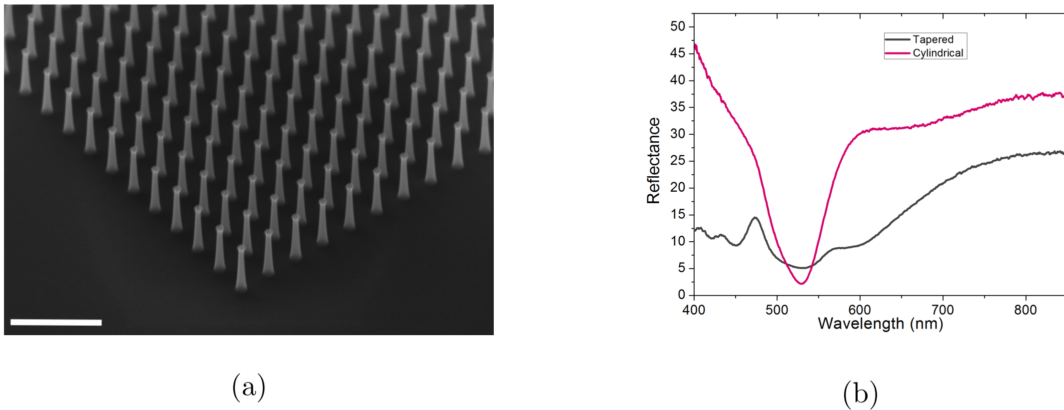


(a)

(b)

Figure 5.19: (a)SEM image of the tapered silicon nanowires. (b) Comparison of reflectance from the cylindrical and tapered nanowires.

## 5.7 Effect of Mask on Absorption of the Nanowires

The hard mask is an essential part of the process of nanowire etching. In our etching processes, aluminum has been an essential part of masking for all semiconductor nanowires because it is convenient to remove without affecting the semiconducting material. In the previous sections, we have seen some reflection features which could not be explained by modes and were attributed to the mask. Thus, it is important to understand the effect of the mask. In this section, the effect of the mask on the reflection and absorption response of silicon nanowires is studied. The reflections measurements of masked and bare

nanowires samples were done F-4- Filmetrics profilometer and the results were confirmed using simulations. Figures 5.20 show the schematic representation of nanowires with and without the mask. The metal mask has been assumed to be hemispherical in shape in previous studies [21,128]. However, in this study, the metal mask is deposited using physical vapor deposition in the written patterns inside the e-beam resist. Thus, the morphology is more close to disc shape than the hemispherical drop. Moreover, the simulations results using metallic discs match well with measured spectra as well.

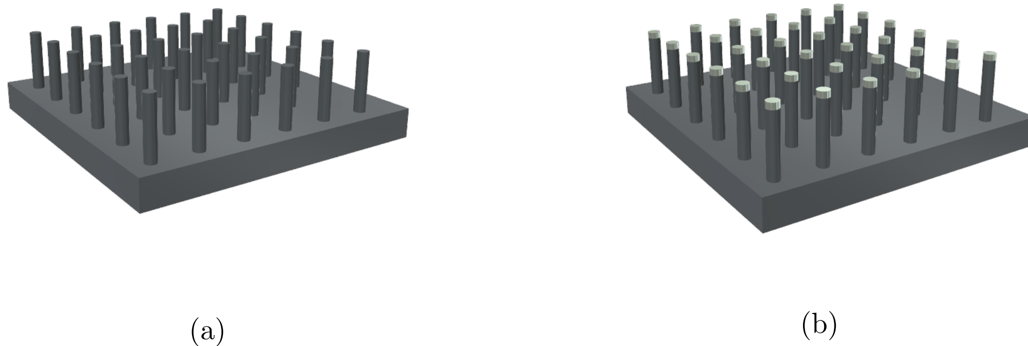

(a) (b)

Figure 5.20: Schematic 3-D representation of (a) Bare (b) Masked nanowires.

### 5.7.1 Measured Reflectance

Three diameters 60 nm , 80 nm and 100 nm were used in this study. The larger diameters were avoided because of the complex reflectance features arising from the higher order modes. The reflection measurements were done by shining visible light from the top, normal to substrate using a light source of F-40 at 10× magnification. The reflections were measured for both the masked and bare nanowires plotted in figure 5.21a(a). The reflectance from the substrate is also plotted for the reference. For longer wavelengths, the reflectance from the nanowires match with the substrate since the light does not interact

with the nanowires at these wavelengths and passes through them to reflect off the bulk silicon. While going to shorter wavelengths, the spectral features start to appear for the nanowires. For 60 nm diameter, the reflectance suddenly drops at around 440 nm, whereas for 80 nm diameter it happens at around 525 nm. 100 nm diameter shows a sudden drop in reflection at 570 nm. This drop in reflectance has been discussed before and is due to the absorption in nanowires from the excitation of $HE_{11}$ modes and rate of drop in reflectance per 1 nm change in diameter is ∼4 nm for silicon.

When the reflections are measured with the mask on the top of the nanowires, the major reflection features remain same including the position of the radial modes. In addition, there are visible reflectance dips for each diameter in the wavelength range above the resonance. These spectral features are basically present in bare nanowires too but they are enhanced due to the presence of the mask. These enhanced features could only be observed by the mask and change with the change in diameter. Thus, the radial modes and aluminum-nanowire interface need to be investigated to understand this phenomenon. In a previous study, it was shown that the nanowires behave as a weak cavity above the resonance peaks. In the presence of the mask, the reflection conditions change suppressing the reflections to a great extent due to the change in the F-P resonance conditions.

### 5.7.2 Simulated Reflectance and Absorptance

To have a better understanding of the reflectance features measured in the last section, the nanowires are simulated using same nanowire parameters and extracted n and k [73]. The simulated reflectance for bare and masked nanowires with a substrate at the bottom are shown in figure 5.21b. The simulation results match well with measured reflections for both bare and masked samples. The enhanced features due to mask are also shown in the simulations. The simulated spectra show sharper spectral features due to the ideal

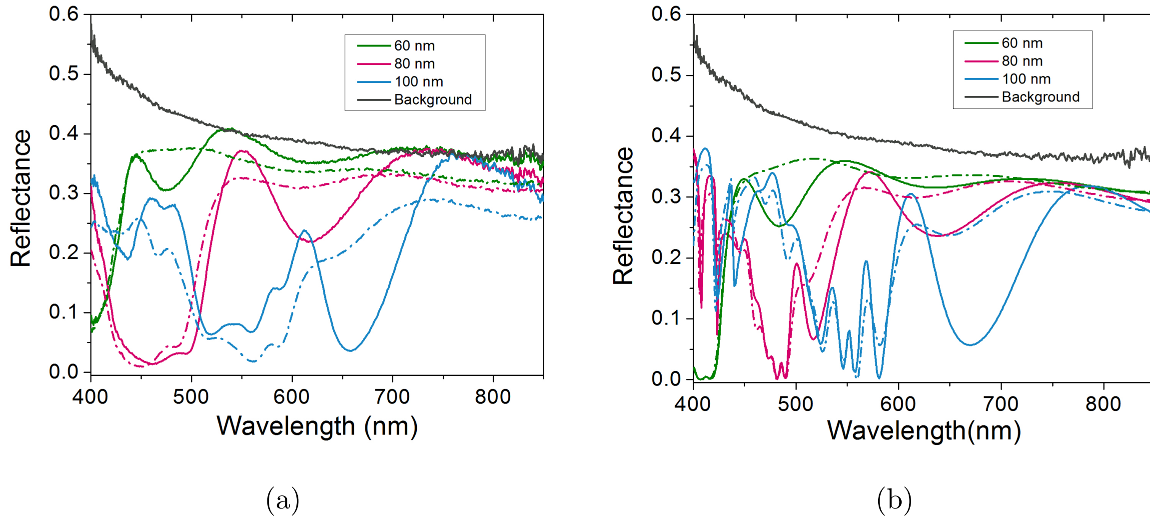


Figure 5.21: (a)SEM image of the tapered silicon nanowires. (b) Comparison of reflectance from the cylindrical and tapered nanowires.

conditions while the real samples may have a surface roughness or variation in parameters, optical constants, and spectrometer resolution. The presence of oxide layer on the aluminum mask is not avoidable experimentally. However, since the spectral features match well enough, it doesn't seem to have major effect on the absorption characteristics.
Using the same simulations, the absorptance in the nanowires is also calculated using 1-R-T. Figure 5.22 shows the simulated absorptance for the three diameters for both bare and masked configurations. Resonant modes were not much affected by the presence of the mask. For 100 nm diameter, the resonant peak was shifted by 5% downwards, which is an insignificant change. For longer wavelengths, the high absorption peaks were observed for masked nanowires for all diameters.

To confirm the role of absorption in metallic nanoparticles, a periodic array of aluminum nano-discs is simulated to calculate absorption in them. The schematic of this arrangement is shown in figure 5.22a. The absorption of the nanoparticles array is plotted with other nanowires in figure 5.22b, showing the negligible absorption compared to the masked

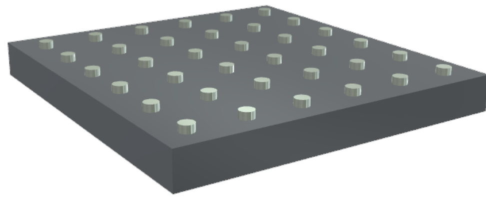

(a)

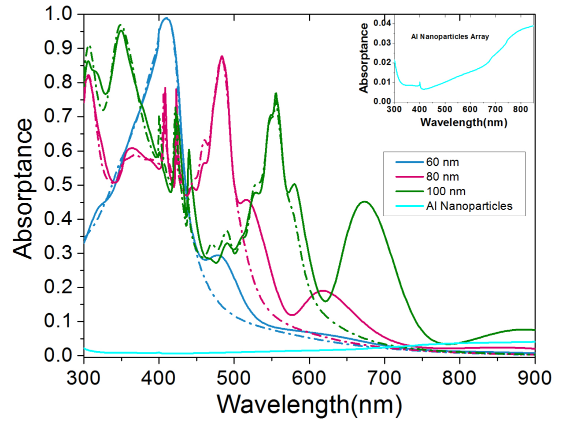


(b)

Figure 5.22: (a)SEM image of the tapered silicon nanowires. (c) Comparison of reflectance from the cylindrical and tapered nanowires.

nanowires. Thus, light is getting absorbed only because the masks are on the top of the nanowires and nanowires are playing a significant role in it. For further investing if the absorption is inside then nanowires or mask, the power monitors is placed below in the mask in the simulation for 100 nm diameter. The absorption in the mask, bare and masked nanowires are plotted together in figure 5.23. This figure shows that the majority of the absorption beyond the resonant peak, where the nanowire does not absorb, lies in the mask and the mask does not contribute to any absorption where nanowire is highly absorbing.

The electric field distribution at two dominant wavelengths 570 nm and 700 nm where nanowire and mask respectively are highly absorbing are plotted in figure 5.24 using FDTD simulations. At 570 nm, the $HE_{11}$ is excited predominantly in the nanowire explaining the high absorption peak (Figure 5.24a). The presence of mask (Figure 5.24b) does not affect the field distribution at this wavelength. On the other hand, at 700 nm wavelength, mask shows some electric field excitation in the mask while the electric field in nanowire still remains unaffected by the mask. It is this field that is responsible for the suppressed

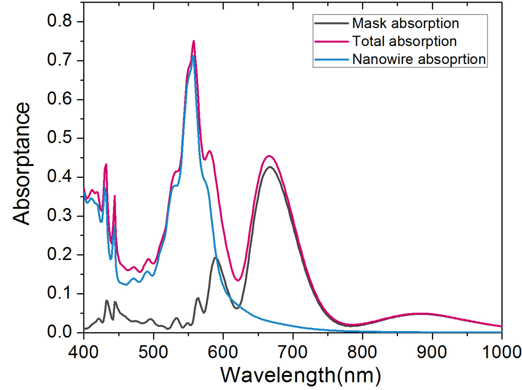


Figure 5.23: The FDTD simulation of absorption in the mask by putting power monitor just below it. The absorption spectra for bare and masked nanowires are also plotted. The diameter is 100 nm for this nanowire.

reflections at the longer wavelengths in figure 5.21. The weak electric field inside the nanowires explains the lack of absorption in it in both bare and masked configurations.

### 5.7.3 Simulations after Removing Substrate

To remove the F-P resonances, the semi-infinite nanowires are used to simulate the electric field distribution in nanowires for different wavelengths. 100 nm diameter was chosen for this analysis for comparison with the pervious section. For 570 nm, 600 nm, 650 nm and 700 nm the electric field distributions are plotted in figure 5.25. There is a field localization happening for all the wavelengths at the interface of nanowire and mask. However, Al nanoparticles on substrate did not show this localization. Thus the waveguiding properties of nanowires are responsible for this field localization.

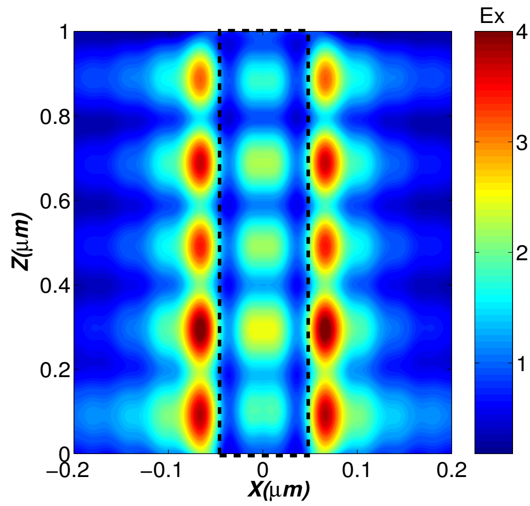


(a) $\lambda$ = 570 nm, Bare Nanowires

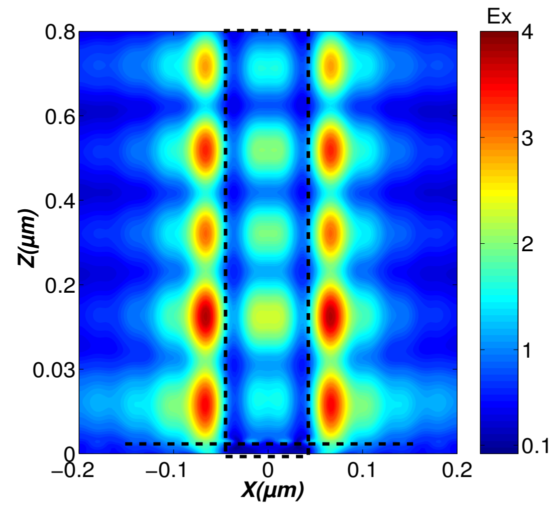


(b) $\lambda$ = 600 nm, Masked Nanowires

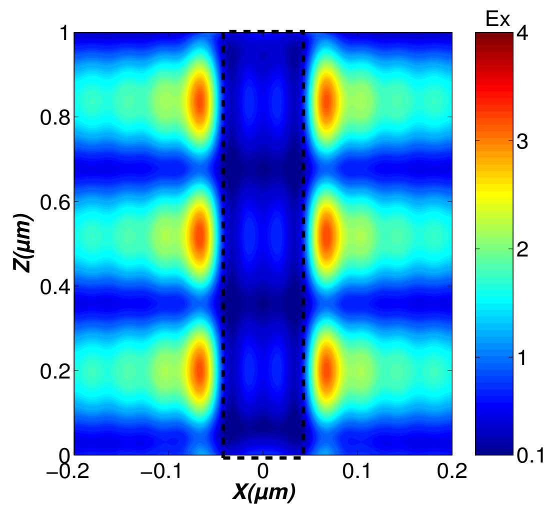


(c) $\lambda$ = 650 nm, Bare Nanowires

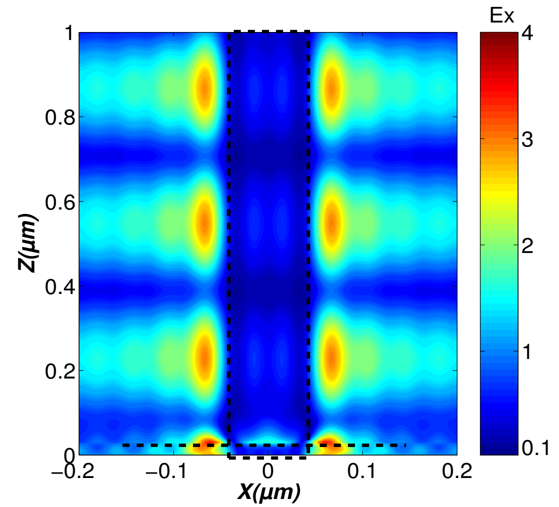


(d) $\lambda$ = 700 nm, Masked Nanowires

Figure 5.24: (a)SEM image of the tapered silicon nanowires. (c) Comparison of reflectance from the cylindrical and tapered nanowires.

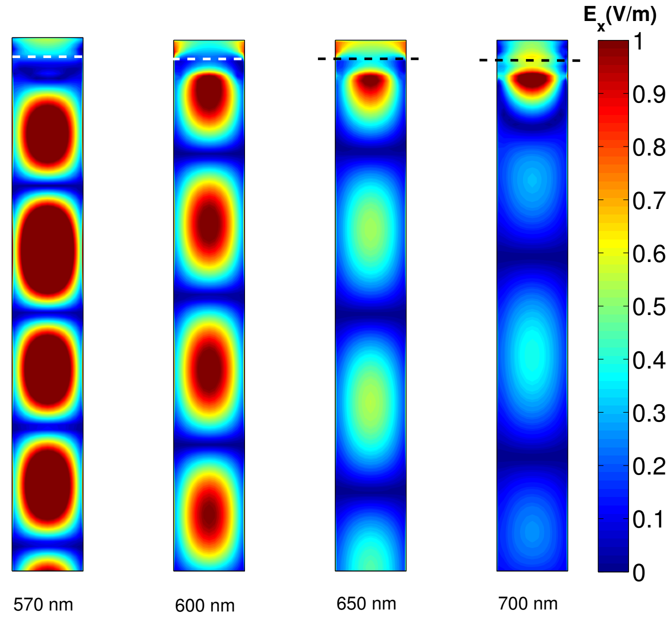


Figure 5.25: Electric field distributions in semi-infinite nanowires at 100 nm diameter for four different wavelengths.

### 5.7.4 Effect of Length

The refractive index mismatch between nanowires, air, and substrate cause the light to move back and forth inside the nanowire reflecting from the nanowire-substrate and nanowire-air interface. In the presence of mask the reflection conditions at the top interface change. It is expected that these reflection conditions will be further affected if the length of nanowire cavity changes. To see the effect of length on the mask peak, the simulations were performed for 100 nm diameter for different nanowire lengths as shown in figure 5.26. The lengths were chosen at 500-2000 nm with 500 nm difference. The longitudinal modes dominate in the region where nanowires are less absorbing. If the nanowire as a cavity has an effect on these peaks then the change in these peaks is expected as the length is changed. As the length is increased, the resonant peak at 570 nm gets stronger and broadens agreeing with the Beer-Lambert law. For the longer wavelengths where the new absorption peak is observed, the change in length changed the peak positions and intensity like F-P resonances. Thus the excitation of longitudinal modes builds up the field

localization at nanowire-mask interface for the constructive interferences. Further, the wavelengths at which the nanowires are highly absorbing, the metal does not contribute in changing the absorptions due to the suppression of F-P resonances. Thus, the aluminum mask does not need to be removed for photovoltaic or other applications as it does not interfere with the absorption properties of nanowires. Further, the mask could be used as self-aligned contacts. In addition, the absorption peaks due to mask could assist in enhanced photothermal conversion where the absorption in nanowires is low [69].

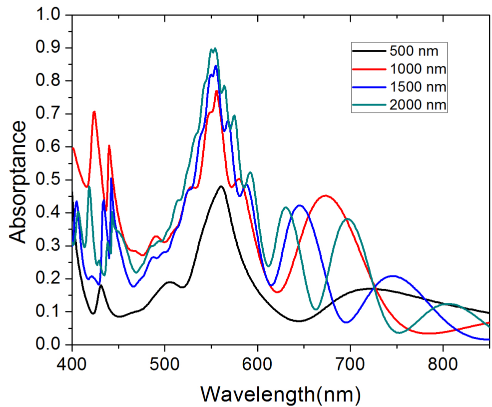


Figure 5.26: Absorption spectra of nanowires at 100 nm diameter, 400 nm pitch at different lengths.The mask thickness is 30 nm.

### 5.7.5 Mask Thickness

To see the effect of mask thickness, the simulations were performed for nanowire parameters used in previous sections by changing the mask thickness from 10 nm to 100 nm. The thickness of mask effects the intensity of absorption peaks at 700 nm. The absorption change is the most prominent when the mask thickness is changed from 10 nm to 20 nm and gradually decreases for every next 10 nm increase in thickness and almost stops to change at 50 nm.

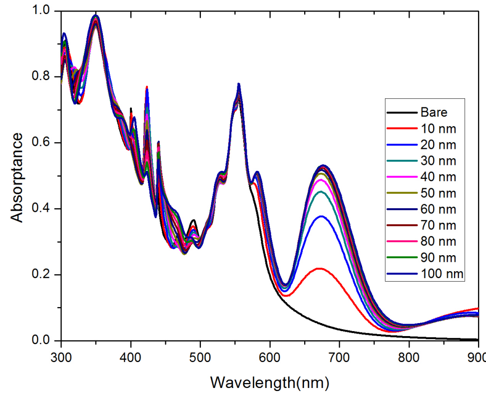


Figure 5.27: Absorption spectra of nanowires of 100 nm diameter, 400 nm pitch and 1 $\mu$m length at different mask thicknesses.

## 5.8 Design Rules for Nanowires

Having understood all the various optical phenomena happening in the nanowires, we can come up with some design rules for optimizing the structures for various applications. For spectral photodetectors, where narrowband absorption is desirable, the dimensions of the nanowires should be such that it only supports the fundamental $HE_{11}$ mode. The length needs to be short so the absorption in the wavelengths shorter than resonance peak does not increase. The optimization of length allows to change the full width half max of the absorption response. For solar cells, where broadband absorption is needed, the nanowire diameter should be designed such that the $HE_{11}$ mode is excited right at the band edge. At the wavelengths shorter than the resonant mode the absorption can be increased by increasing the length of the nanowire (Beer's Law) and also due to the excitation of higher order modes if possible. This is because above $HE_{11}$ excitation only weakly guided leaky modes are excited and absorption in the nanowires drops remarkably. Nanowires for solar cell applications need to be long (at least 1.6 $\mu$m for GaAs as an example). Thus the nanowire platform allows optimization for different optical responses. There in lies their

huge potential in optoelectronics applications.

## 5.9 Conclusion

In this chapter, the measured response of the nanowires fabricated in chapter 4 and simulated in chapter 3 is discussed. The reflection and transmission measurements were used to verify the optical response of the nanowires predicted in simulation studies in chapter 3. The effects of diameter, pitch, length, mask, disorder and shapes were explored and most of them were successfully modelled. Due to our graphical understanding, it allows us to get to the optimized designs very quickly. The absorption peak seen at longer wavelengths is due to cavity excited plasmon modes within the mask and is a new mode found in this study. In future, this can be used for designing optical filters. In summary:

- The modal excitation in GaAs and a-Si nanowires were shown using the reflection measurements and they were confirmed well with our simulations studies.
- The resonance excitation of an optical mode depends nearly linearly on the diameter, increasing as the diameter is increased.
- First the $HE_{11}$ mode is excited which shifts to longer wavelengths in a near linear fashion as the diameter is increased. The rate of shift varies from 3.2 nm/1nm change in diameter to 4.0 nm/1 nm change in diameter.
- The F-P modal excitations can be seen at longer wavelengths at large diameters where the absorption is low.
- For different semiconductor nanowires with different refractive indices, the resonance wavelength for a fixed diameter varies nearly linearly with the refractive index.

- As the diameter is increased, higher order $HE_{1m}$ get excited. They absorb less than the fundamental mode and shift at a slower rate than the fundamental mode.

- The effective absorption coefficient in the $HE_{11}$ mode is $\sim 2.5\times$ the absorption coefficient of the bulk semiconductor, even for different semiconductors.

- For semiconductors with lower absorption coefficient like silicon, near field coupling leading to excitation of Bloch modes exists. The coupling is anti-symmetric and leads to further enhancement of absorption and a blue shift in the resonance wavelength. The coupling exists till a lattice spacing of ~700 nm and is of long range order; not just nearest neighbour coupling. We do not see evidence of this coupling in direct bandgap high absorption semiconductors like gallium arsenide or amorphous silicon.

- The length analysis performed in chapter 3 was verified in this chapter to show the nanowire behavior after 150 nm length in silicon nanowires.

- The tapered nanowire showed broadband absorption due to adiabatic coupling for tapered GaAs and silicon.

- The effect of the mask on the absorption characteristics on Silicon nanowires tested showing that the cavity enhanced plasmonic modes in metallic mask get excited and show absorption feature where nanowires don't absorb well. The effect was also shown in a-Si nanowires for large diameters.

# Chapter 6

# Absorption Optimization for Applications

Understanding the properties of nanowires for all the different materials in the previous chapters leads us to enhance and engineer their properties for photonics and optoelectronics applications. We have understood that how the leaky waveguide modes, photonic crystal modes, and F-P modes manifest the absorption characteristics of silicon and III-V semiconductor nanowire arrays. The researchers have used some of these characteristics of nanowires to propose the devices that we discussed in the first chapter. However, there is still a void in all the application areas involving nanowires. Most of the proposed devices are based on the samples grown on the substrate, which has a major drawback as the most of light gets absorbed in the substrate or scattered due to the disordered arrangement or surface roughness of the etched substrate affecting the absorption and conversion efficiencies. The process of bottom contacting is still not perfected and requires new methods to be able to harness the photogenerated carriers. These are the reasons that nanowires have not been able to compete with the achievable efficiencies of planar solar cells, photodetectors or other commercial optoelectronic devices. Kelzenberg *et al* [129] peeled off

the silicon nanowires to show the high broadband absorption up to near infrared and high external quantum efficiency to propose them as a potential candidate for next generation solar cells. Park*et al* [54] has done the same to propose them as the filter free sensors. However, the peeling off nanowires is not a very user-friendly technique and may not make its way to the industrial applications. We, in this study, propose two different approaches for studying and manipulating the substrate-free properties of the nanowires. Firstly, we will discuss the removal of the substrate from the multijunction GaAs nanowires and show their excellent absorption properties and in the second experiment, we will demonstrate a platform where the thin film and nanowires integration on the glass substrate could lead to excellent absorption properties compared to their thin film and nanowires counterparts.

## 6.1 Substrate Free GaAs Nanowires for Photodetectors

We have already discussed the excellent absorption properties of GaAs nanowires on a substrate showing their potential in solar cells and photodetector applications. It is, however, mandatory to remove the substrate from below the nanowires to test their true optical properties and to use them for potential applications. Indium Gallium Phosphide(InGaP) is a wide bandgap material used in heterojunctions solar cells and does not get etched with the $Cl_2$ etch chemistries. Sandwiching a thin layer in InGaP between two GaAs thin films using MBE makes a perfect design for the substrate free GaAs nanowires: One side being etched using wet chemical etching to remove the GaAs and the other being etched to make nanowires. Use of an etch stop layer which works for both wet and dry etching is unique to our knowledge.

### 6.1.1 MBE growth of GaAS/InGaP wafer

Our collaborators at McMaster University deposited the GaAs/InGaP layer on a GaAs wafer that was 350 $\mu$m thick p-doped with Zinc ($5\times10^{18}$ cm$^{-3}$), which was intended for a photovoltaic device using these nanowires. There was a 50 nm thick p-GaAS buffer layer deposited on the starting substrate having $3\times10^{18}$Be cm$^{-3}$ doping. Later on, a 70 nm thick lattice matched p-InGaP layer ($1\times10^{18}$ cm$^{-3}$ Be doping was deposited as an etch stop layer. Beyond it, a 1.5 $\mu$m thick p-GaAS layer($1\times10^{17}$Be cm$^{-3}$ doping), a 100 nm n-GaAs layer as an emitter ($3\times10^{18}$ cm$^{-3}$ Si doping) and lastly a 30 nm $n^+$-GaAs layer as a contact ($1\times10^{19}$ cm$^{-3}$ Si doping) was deposited. The layers on the part of the InGaP thin film were intended for the nanowire fabrication.

### 6.1.2 Nanowires and Device Fabrication

We have already discussed the fabrication of GaAs nanowires in Chapter 3. In this setup, the same recipe was used to create the nanowire arrays shown in figure 6.1. As mentioned in the previous section, the etch stop InGaP layer is inserted 1.6 $\mu$m below the GaAs layers, where the etch rate is reduced by 10 times while performing the dry etch. It helps in precisely controlling the length of the nanowires and surface below the nanowires remains roughness free. The SEM images of the nanowires are already shown in chapter 3, showing smooth, vertical nanowires. The nanowires with diameters 90 nm, 130 nm, 160 nm and 200 nm at three different pitches: 270 nm, 350 nm, and 460 nm were chosen as these are optimal sweet spots for high absorption.

For nanowires to operate as a device, it is essential that we test their optical properties by encapsulating them in all the needed coatings for making contacts. The nanowires gaps were filled with cyclotene to planarize the top surface, which was then baked in $N_2$ environment for 30 minutes at 250°. The top part of cyclotene was etched using RIE system

with $CF_4$ and $O_2$ chemistry. The Al/Cr nanowire mask was removed using Microposit MF319. Each array of nanowires was contacted using transparent conducting oxide (25 nm Tn and 500 nm of ITO) having low contact resistance. At the periphery of ITO pad, a 15 $\mu$m wide Ni/Ge/Au(50/100/250 nm) square ring was deposited. These processes were done by our collaborators in McMasters.

### 6.1.3 Wet Etching of GaAs Substrate

A glass was bonded to the nanowire side o the substrate using 2 $\mu$m thick EPO-TEK 301-2 epoxy and was cured in an oven at 80° for 3 hours. An etch window was opened on the back side of the substrate using optical lithography with S1818 photoresist, which was aligned to the nanowire pads on the other side. $H_2SO_4$:$H_2O_2$:$H_2O$(1:1:10) solution was used to etch GaAs through the etch window at room temperature. The wet chemical etch stops when it reaches InGaP thin film as the etchant is selective to GaAs only. The schematic of the resultant setup is shown in figure 6.1b

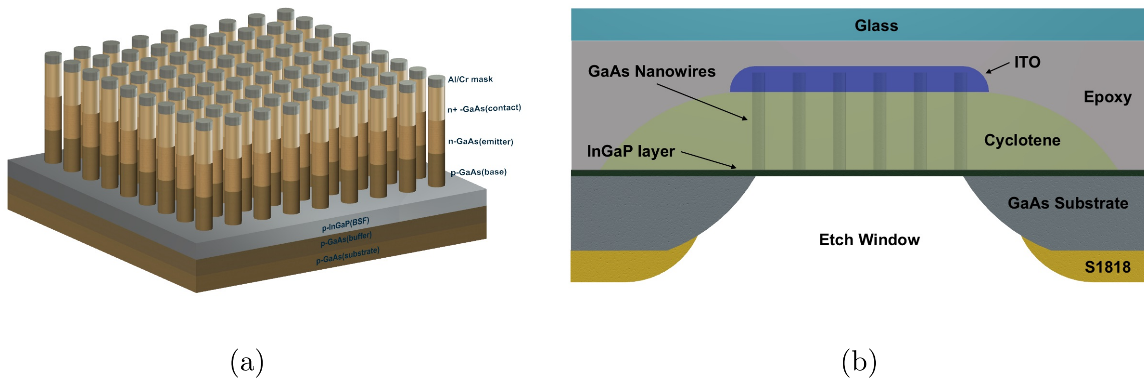


(a) (b)

Figure 6.1: (a) The schematic of GaAS nanowires etched on the top of GaAS/InGaP substrate (b) The schematic of nanowires after making the top contacts and removing the GaAs substrate.

### 6.1.4 Absorption Calculations

The R and T measurements were done as mentioned in chapter 4. The spectral range was 400 nm to 900 nm, the light source was the Ocean Optics LS-1 tungsten halogen lamp, the focused spot diameter was 70 $\mu$m and spectra were collected using Ocean Optics Jaz spectrometer. From R and T values measured from the optical setup, 1-R-T was used to calculate the absorption in the nanowires. Figure 6.2 show the resulting absorption spectra different diameters and pitches. RCWA simulations were performed to by using including cyclotene, ITO, glass, epoxy and InGaP thin film. The measured results match well with the simulations, except in the longer wavelength range where the light gets scattered instead of reflecting back due to the surface roughness. The broadband absorption spectra for all the diameters and pitches matches well with the simulation spectra where the absorption edge increases with increase in the nanowire diameter. The behavior expected as we predicted in the previous chapters.

To quantify these absorptions, solar weighed absorption efficiencies of the nanowires were calculated as:

$$\eta = \frac{\int I(\lambda)A(\lambda)d\lambda}{\int I(\lambda)d\lambda} \tag{6.1}$$

where $I(\lambda)$ is the AM1.5G solar spectrum. The solar weighed absorption efficiencies for all the samples are shown in the table 6.1. The efficiencies could reach up to 94% for 200 nm diameters at 460 nm pitch while covering only a fraction of the bulk. As shown in table 6.1, the efficiencies increase nearly monotonically with the increase in the diameter for all the pitches. However, this linear trend cannot be sustained as the fill fraction of the

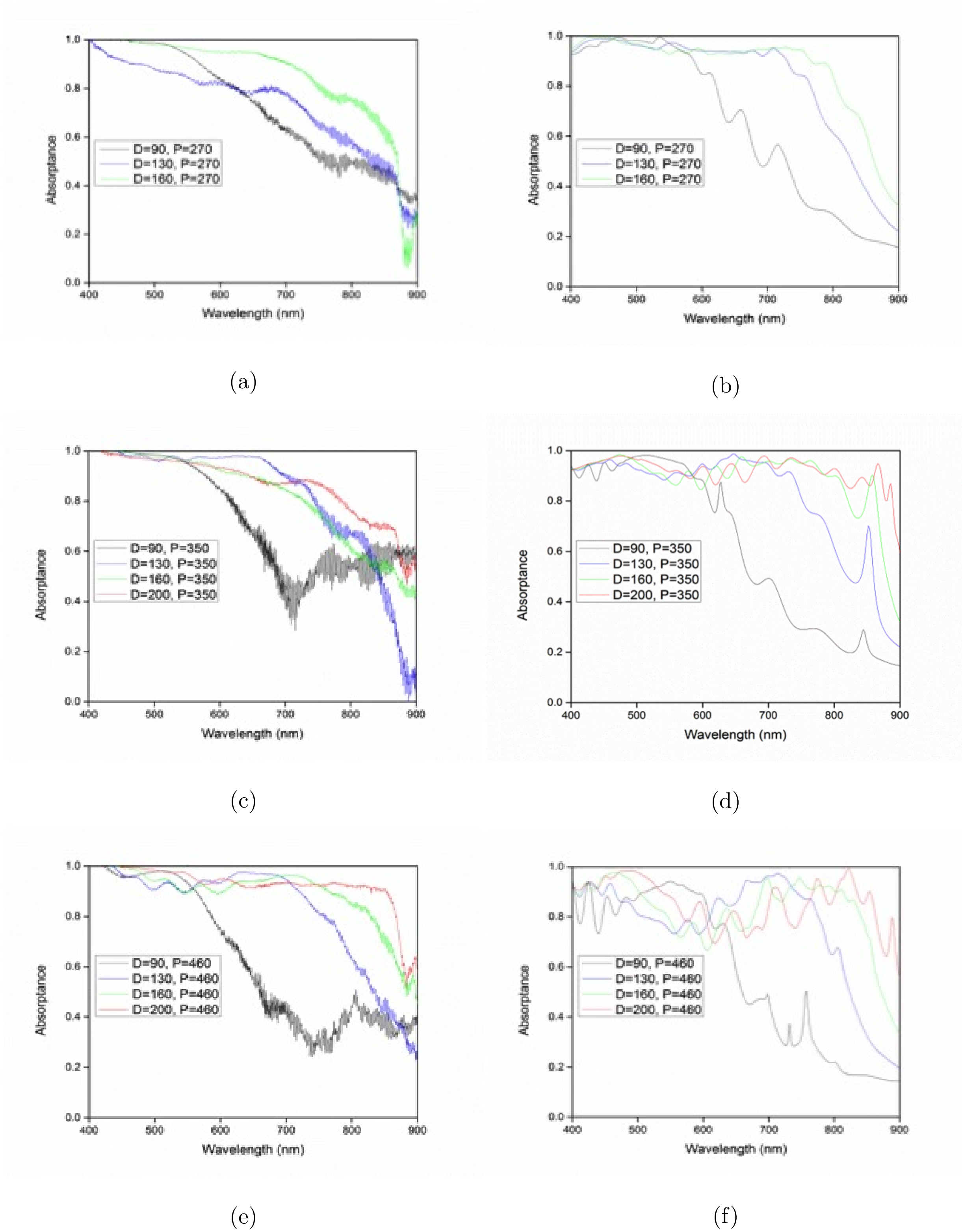


Figure 6.2: (a) Reflection of nanowire arrays at different etch depths at 700 nm pitch and 85 nm diameter (b) Simulated reflections from the nanowires with the same diameter and pitch at similar etch depths.

nanowires approaches the bulk and the efficiencies will eventually start to reduce at some point. It will be discussed in detail in the next section for a-Si nanowires where a full study was done. Additionally, there is negligible scattering in these materials as opposed to the randomly arranged nanoparticle or disordered densely packed grown nanowires, in which the diffuse reflections and scattering dominate over waveguiding. This high absorption in nanowires makes them ideal for photodetectors and solar cell applications, especially in the presence of wide band-gap InGaP layers and precisely controlled doping.

From table 6.1 we also see that the nanowire array with diameter of 200 nm provides the highest efficiency. In chapter 5 we had argued that to achieve the highest efficiency the diameter of the nanowires should be such that the excitation of the $HE_{11}$ mode is at the band edge. For the nanowires surrounded by air, this diameter was 175 nm. However, these nanowires are surrounded by cyclotene which has a refractive index of 1.6 (higher than air). If we calculate the normalized frequency parameter V for the two cases it turns out to be nearly same.

| | **D=90 nm** | **D=130 nm** | **D=160 nm** | **D=200 nm** |
|---|---|---|---|---|
| **P=270 nm** | 72.3% | 74.5% | 87.9% | |
| **P=350 nm** | 71.3% | 85.5% | 83.0% | 87.9% |
| **P=460 nm** | 61.5% | 84.4% | 90.7% | 93.9% |

Table 6.1: Solar weighed absorption efficiencies for GaAs nanowire arrays

## 6.2 Nanowires Integration with Thin Films for Enhanced Absorption and Colorful Solar Cells

From our understanding of waveguiding properties of nanowires in chapter 3 and 5, it has now become easier to introduce the complex designs to nanowires arrangement to tailor their optical properties. We have understood that nanowires on glass are dominated by leaky waveguide modes and F-P resonances depending on the diameters and length of the nanowires. It is also understood that in the wavelength regions where the complex part of the refractive index is high, the waveguide coupling becomes negligible while it plays a dominant role in absorption region where absorption is small. The capability of highly controllable ICP etching, a-Si deposition on multiple surfaces brings us to the point where we can measure the absorption properties of nanowires to be controlled by integration of thin films with nanowires. Here we propose a platform involving a-Si thin films and nanowires as shown in figure 6.3. The structure consists of a-Si:H nanowires arranged in a square array with a pitch of 400 nm and residual thin film below the nanowires. The lateral size of the nano- wire arrays is 100 $\mu$m $\times$100 $\mu$m. A 535 nm thick layer of a-Si:H is deposited on glass and nanowires are etched into the layer using top-down fabrication. This configuration allows many different options to optimize the geometrical parameters giving one the freedom to tailor the optical properties. These geometrical parameters include the diameter, length, and pitch of nanowires, the thickness of the original a-Si:H layer and the thickness of the residual thin film layer. The coupling of thin films and nanowire F-P modes introduces coupled cavity modes to trap the light that is otherwise lost in the transmission or scattering. To test this design, the a-Si nanowires were etched to the different depths and leaving residual thin films to play their role in the F-P coupling. We tested this design for four different diameters 100, 150, 200 and 250 nm shown in figure 6.4. Although we have already discussed nanowires on glass samples but for the continuation

to the integration with thin films, we will discuss them again briefly.

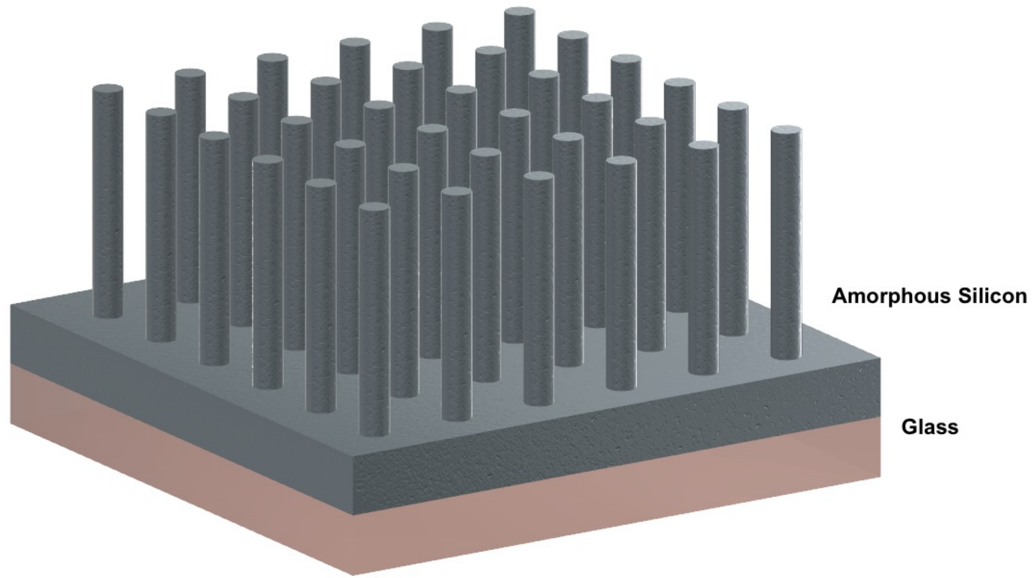


Figure 6.3: Schematic of the a-Si nanowire/thin film platform on glass.

### 6.2.1 Sample A - Nanowires on Glass Substrate

Having glass as a substrate, this platform permits to measure the optical response of a-Si:H nanowires alone. This configuration is discussed in detail in chapter 5, showing absorption and transmission features in nanowires on glass for the given diameters. As discussed earlier, the strongly absorbing $HE_{11}$ modes excite for 100 nm diameter nanowires at 600 nm wavelength as shown in figure 5.6a giving transmission filter response at this wavelength. This filter response can be tailored for other wavelengths by changing the diameter of the nanowires until multiple modes start to excite at larger diameters. For diameters150-250 nm, because of the excitation of multiple modes, the absorption becomes broadband. Thus, for solar cell applications, it is beneficial to go to larger diameters. Further, as discussed in chapter 3, the modes redshift in wavelength nearly linearly with diameter

allowing simple design rules for optimizing the absorption and transmission characteristics of the nanowires. Larger diameters also provide stronger F-P modes at wavelengths longer than the resonance peaks.

### 6.2.2 Sample B - 500 nm Long Nanowires with 35 nm Thick Thin Film

The low reflections at the air-glass interface (<10%) work well for realizing filter response. However, to increase the absorption inside the nanowires the light needs to reflect back from the bottom interface of the nanowires. Hence, introducing a thin film of a-Si:H below the nanowires could assist the nanowires to absorb the off-resonance wavelengths. To understand this behavior, a sample was created with 500 nm long nanowires and 35 nm thick thin film. At the thickness of 35 nm, the thin film does not have strong F-P resonances making it easier to understand the presence of any new peaks. As shown in Figure 6.5b, the overall reflection is increased while the transmission is decreased across the measured wavelengths. For wavelengths lower than the resonant peaks, the reflections have a peak value at approximately 30% at $\sim$ 520 nm. The local maximum in the reflection also corresponds to a local maximum in the transmission. Thus, these maxima should not arrive from longitudinal modes [130]. For longer wavelengths, both the reflection and the transmission increase. However, a new minimum in reflection is observed at a wavelength of 660 nm. At this wavelength, there is a small peak in the transmission suggesting that these could be resulting from resonant excitation of the longitudinal modes inside the nanowires [130]. Beyond the resonance peak, the increased reflections result from the nanowire/thin film interface. When the nanowires are not absorbing well, more of the light sees these interfaces and hence, the reflections are increased due impedance mismatch [34]. At 600 nm, the reflection and the transmission are low because of the high absorption

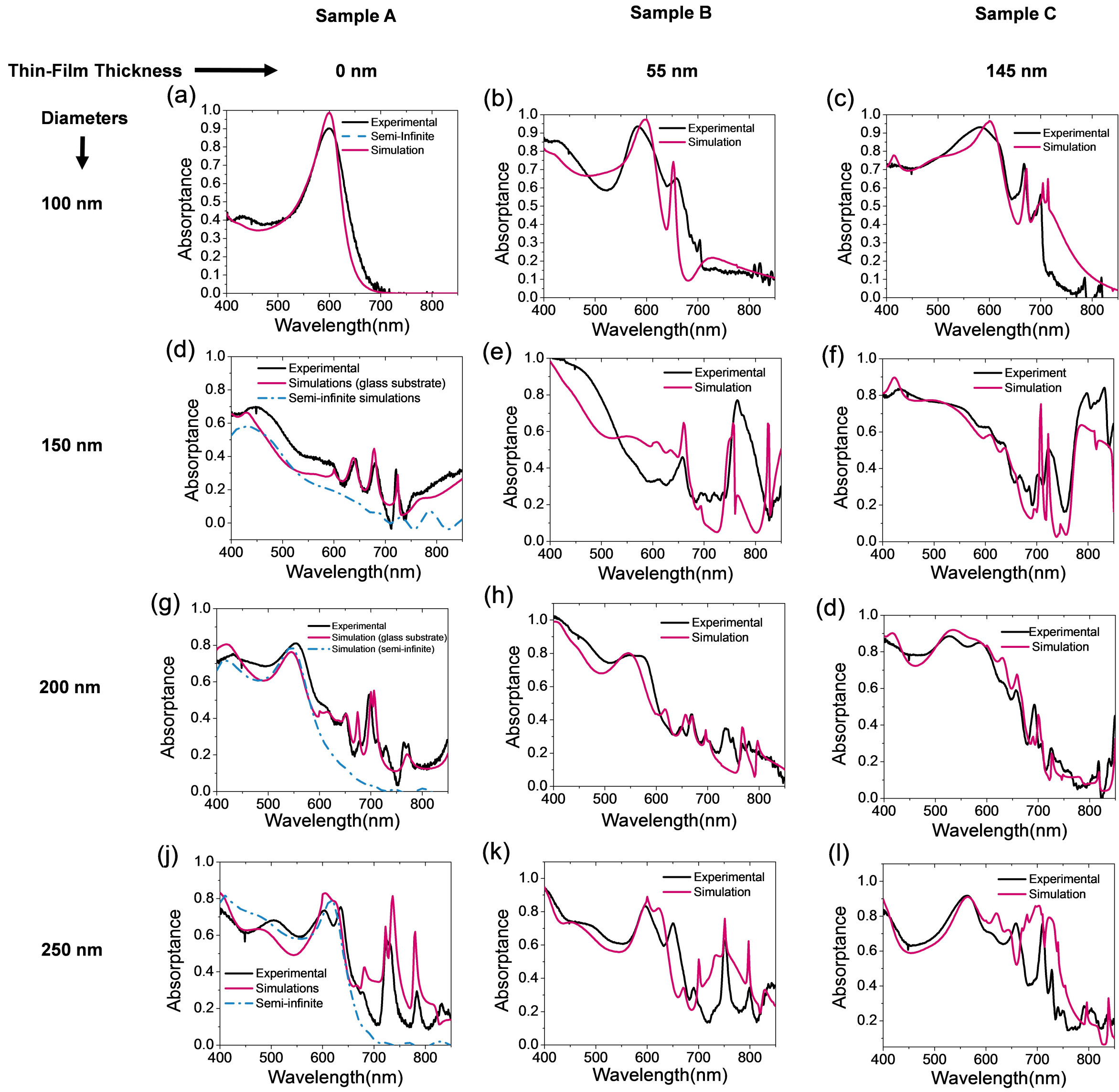


Figure 6.4: Absorption spectra of a-Si nanowires with different diameters and thin film thicknesses.

within the nanowires itself, making the effect of the thin film minimal. To understand the origin of the above-mentioned features, we look at the absorption spectrum in figure 6.4a. and the measured absorption from the initial 535 nm thick thin film and the residual 35 nm and 135 nm thick thin films in figure 6.5d. The 35 nm thin film absorbs light well at 400 nm but the absorption drops sharply as the wavelength is increased. No F-P response is observed as expected in the residual thin film due to it being very thin. The resonant peak at 600 nm still exists as in Sample A and the absorption is larger than either the starting thin film or the residual thin film below. However, the absorption at the resonant peak is slightly lower than the Sample A. This could be due to the reduction in length of the nanowires. Also, a new peak is observed at the wavelength of $\sim$ 660 nm, which is longer than the resonant peak. This peak is clearly manifested as a dip in the reflection spectra showing that the light is being trapped in the structure bouncing back and forth between the nanowires and the thin film coupled cavity. Multiple passes of light allow for increased absorption and since the phase has to be constructive over a round-trip, a new resonance peak is observed. Increased reflections at the nanowire/thin film interface allow for these multiples passes. Local minima in reflections and a local maximum in transmission confirm that this new peak is due to longitudinal modes. This peak also corresponds to that from the starting thin film of thickness 535 nm. This longitudinal mode is not observed in Sample A because of the very low reflections from the nanowire glass interface. Higher absorption as compared to the starting thin film is also observed at a shorter wavelength between 400 nm - 480 nm. Light not absorbed by the nanowires will penetrate into the 35 nm residual thin film. In fact, at shorter wavelengths, the absorption profile follows that of the 35 nm thin film and a new peak seems to become apparent due to the summation of the absorption profiles of both thin film and nanowires. In summary, for wavelength below resonant wavelengths, the absorption profile follows the sum of the absorption profile for the nanowires and the thin film. At resonance wavelength, absorption is dominated by

the profile of the nanowires. At wavelengths longer than the resonance wavelength, the new absorption peak is observed due to excitation of longitudinal modes trapping light in the nanowire/thin film cavity. Overall, the sample has completely changed the absorption profile as compared to just the nanowires or the thin film, increasing absorption in specific wavelength bands even though the thin film is only 35 nm thick. However, broadband absorption over the visible wavelength regions is not yet observed.

Similarly, for higher diameters, the incorporation of the thin film allows further enhancement in the absorption due to multiple effects. First, the reflection at the nanowire/thin film increases allowing a large part of the light, which is not absorbed in the nanowires to bounce back into the nanowires. Sample B with 55 nm thick thin film has this fundamental excitation. If one compares the absorption for different diameters between Sample A and Sample B, the absorption increases over the band but the absorption profile remains similar. The increase in absorption is due to the enhanced reflections at the nanowire/thin film interface. The thin film itself does not absorb appreciably at 500 nm wavelengths.

### 6.2.3 Sample C - 400 nm Long Nanowires with 135 nm Thick Thin Film

To account for the effect of F-P resonances in the thin film, another sample was created with the residual thin film thickness of 135 nm and the length of the nanowires at 400 nm. The reflection, transmission characteristics of Sample C are shown in figure 6.5. Again the reflection is high for wavelengths shorter or longer than the resonant absorption peak. However, the low reflection spectral feature is broader than those observed for the previous samples. Strong F-P effects are also observed in the transmission for wavelengths longer than 650 nm and two minima in transmission response appear at wavelengths of 660 nm and 700 nm. The absorption characteristics of Sample A are shown in figure 6.4. As can be seen,

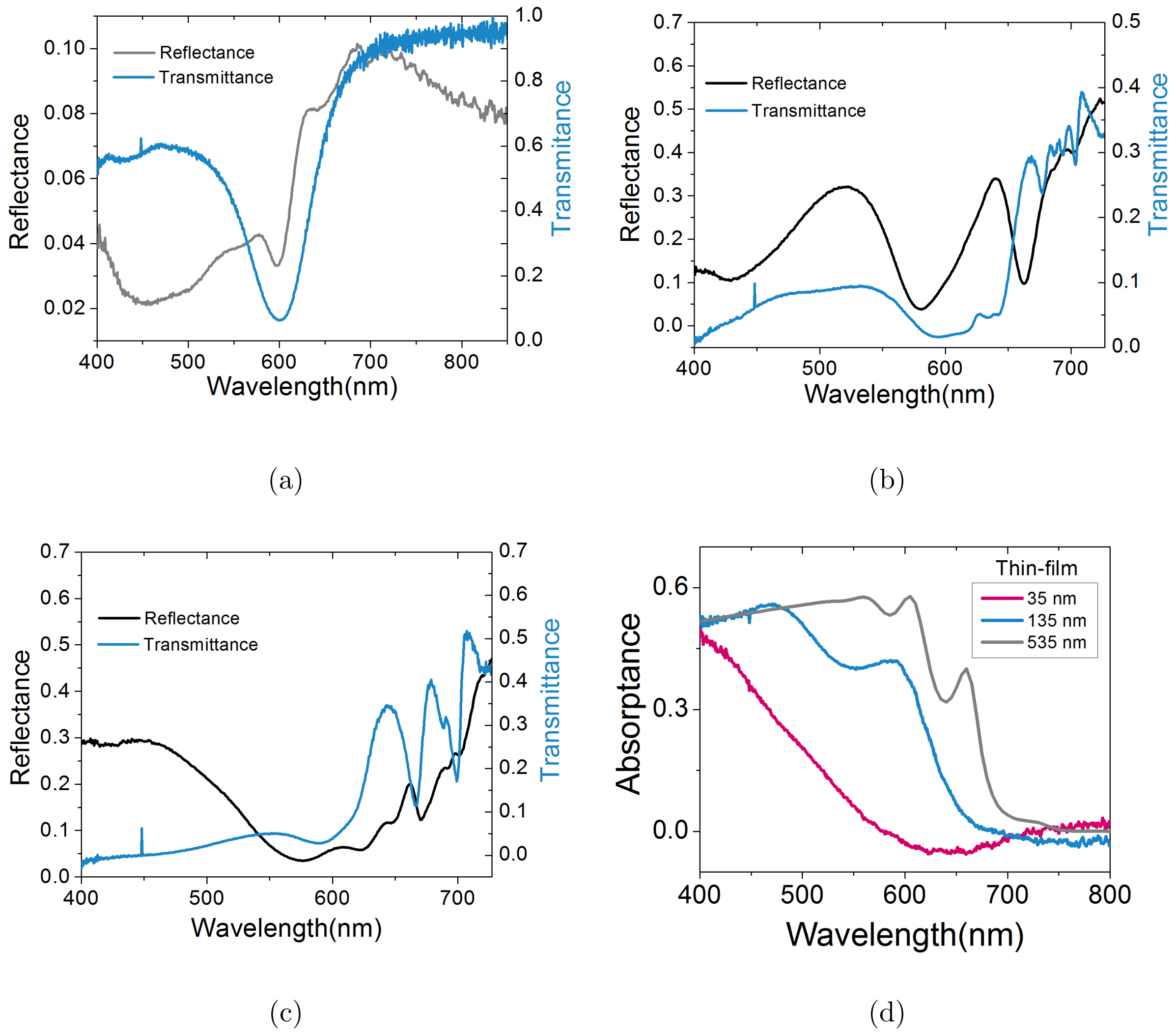


Figure 6.5: The reflection and transmission spectra of a-Si nanowires having 100 nm diameter with three different thin film thicknesses (a) 0 nm (b) 55 nm (c) 145 nm (d) Absorption spectra of thin films for different thicknesses.

the absorption is appreciably higher than the starting thin film or the nanowires alone over the complete wavelength range. The absorption value is also higher than either Sample A or Sample B. Two new absorption peaks are observed at wavelengths of 660 nm and 700 nm. These peaks were predicted in the previous theoretical study [131]. These peaks result from the coupled cavities of the nanowires with the residual thin film for an effective cavity 535 nm thick and can be explained as longitudinal photonic bandgap [131]. At these peaks, the round trip phase delay in the nanowire cavity is in constructive interference with the round trip phase within the thin film resulting in longitudinal coupling between the nanowires and the thin film. Due to these new modes, the sample is absorbing light more efficiently than either the nanowire sample or the starting thin film sample at longer wavelengths. For wavelengths shorter than the resonance wavelength, a broadband absorption is observed, again following the profile of the thin film. Light not absorbed by the nanowires, get a chance to be absorbed in the thin film. Similarly for larger diameters, as the thin film thickness is increased, they start to have more dominant F-P resonances. The absorption around 700 nm becomes larger. The samples studied to demonstrate the versatility of the proposed platform. One could create transmission filters using just nanowires on the glass substrate. Furthermore, changing the length of the nanowires can alter the peak width. On the other hand, enhanced absorption can be achieved due to the combination of the nanowire and thin film absorption and existence of longitudinal photonic band gap modes. Additionally, the enhancements may be further possible by optimizing the diameter and arrangement of the photonic lattice.

### 6.2.4 Structural Colors

The change in diameter, thin film thickness, and nanowire length affects how different wavelengths behave while interacting with this platform. Since we are dealing with diam-

eters affecting the light interactions below the band gap of a-Si (∼727 nm), it is expected that we see a change in reflected and transmitted colors in these configurations. The colors were viewed under the microscope at 5× magnifications. The light source and objective were kept on the top of the sample for imaging reflected colors whereas the objective was placed behind the samples and the light source was on the opposite side of the sample for capturing transmission colors. The observed images in transmission and reflection are shown in figure 6.6. Colors from the starting thin film and also the residual thin film are also shown in the figure. As can be seen, different and vibrant colors are observed for different diameters and thin film thickness. For sample A with 145 nm thickness, the transmitted colors for all diameters are in the red range. The transmitted color of the thin film is also red showing the thin film is dominating the transmitted colors. This can be predicted from the absorption seen, as shorter wavelengths are highly absorbed. However, in the reflected domain, vivid colors of different hues are imaged and colors in all hues from blues to reds are observed. In the reflection mode, reflection from the nanowires dominates the structural color generation and the results are similar to what is observed for semiconductor nanowires on semiconductor substrates. When the thin film thickness is decreased to 55 nm, vivid hues are now observed both in reflection and transmission. Similarly, nanowires on just the glass substrates create vivid hues depending on their diameters. By changing the diameter and length of the nanowires, a wide variety of colors can be achieved both in transmission and reflection.

### 6.2.5 Solar Weighed Absorptance

Finally, we evaluate how the absorption efficiency changes as the different geometrical parameters are changed. The absorption efficiencies were quantified in the measured wavelength range by weighting the measured absorption profile by AM1.5G solar spectrum.

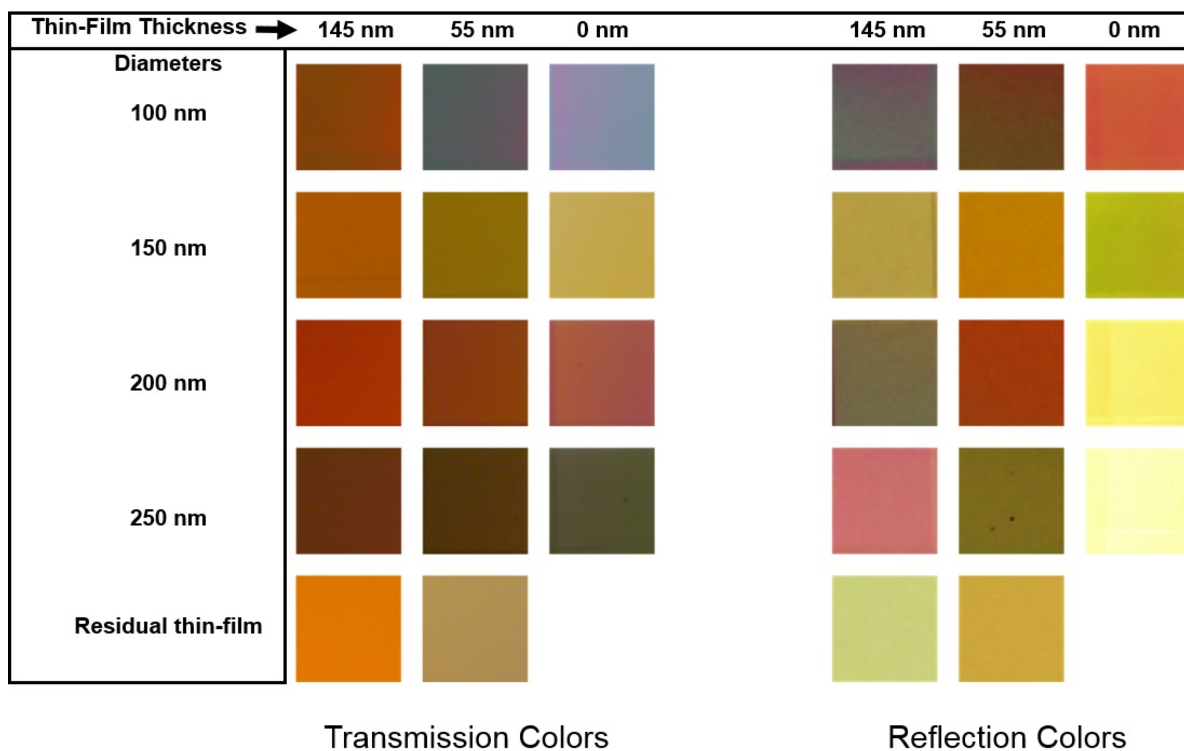


Figure 6.6: Reflection and Transmission colors of the platform having nanowire arrays with diameters and thin film thicknesses.

This quantification is important for comparison with other designs and materials for application in solar cells. The absorption efficiency was calculated using the equation 6.1.4 and the results are plotted in Figure 6.7. The absorption beyond 727 nm is not included in the absorption efficiency calculations as it is inside the aluminum mask. In general, the efficiency in the thin film/nanowire configuration is higher as compared to nanowires on the glass and thin film on glass samples. Also, the presence of thicker thin film gives higher absorption efficiency compared to relatively thinner thin film. For nanowire on glass configuration, the efficiency increases with increase in diameter except while moving from 100 nm to 150 nm diameters where the efficiency is slightly reduced. This is because the $HE_{11}$ mode for the 150 nm diameters has moved above the band gap while the $HE_{12}$ mode is still excited at lower wavelength bands. While moving from 0 nm to 55 nm thin film, there is a big jump in absorption efficiency for 100 nm and 150 nm nanowires increasing the efficiency from ∼40% each to ∼65% and ∼51% respectively. The reason for it is the sudden increase in the absorption in the wavelength range of 400 nm - 500 nm due to the presence of thin film whereas this is not observed at 200 nm and 250 nm diameters, as they already are highly absorbing in this area. For 145 nm thick thin film, the efficiency of 150 nm diameter shows the highest jump from ∼51% to ∼60% (i.e. 16% increase in efficiency), which is due to the broadband absorption in 400 nm to 600 nm range of wavelengths because of the presence of the thin films. The larger diameters of 200 nm and 250 nm show a 13-15% improvement in their absorption efficiencies. Importantly, we are able to maintain enhanced absorption efficiencies over a wide range of dimensions while achieving different structural colors. Thus, the proposed platform allows for a large design space to achieve high efficiency while generating different colors. The experimental data shows higher absorption efficiency for the nanowires with the largest diameter of 250 nm. The results show that there should be an optimal diameter for which we achieve the highest absorption as the value should not just keep on increasing. It was difficult for us to fabricate diameters

larger than 250 nm as the nanowires became closer to each other creating problems during the lift-off process. In order to understand the optimal diameter for absorption efficiency, we extended the diameter range by performing FDTD simulations for diameters ranging from 100 - 375 nm with 25 nm step size. The simulated results are also plotted in figure 6.7 (dashed lines) and match well in values and trends with the experimental data. The simulations suggest that as the diameter is increased above 250 nm, the absorption efficiency starts to decrease. Coincidentally the diameter for maximum efficiency is 250 nm, the largest diameter experimentally studied. As the diameter is increased, the reflections at the nanowire-air interface increase resulting in less light penetration into the nanowires. Further, the absorption peaks of modes start to red-shift and some move above the band gap. While higher order modes are excited, they have weaker absorption per unit length as compared to the lower order modes. This trend has been previously seen in III-V nanowires [20, 21] where the highest absorption efficiency was achieved in those nanowires when the first order mode is right at the band edge and higher order modes are excited at the lower wavelengths. In our proposed structures; the highest efficiency is achieved at larger diameters where the first order mode has moved out of the band edge. This is different than the III-V nanowires and this happens because of the excitation of the longitudinally coupled cavity modes which increase the absorption in the longer wavelengths. In this study, we have used e-beam lithography for the fabrication because of its suitability in experimental design. E-beam lithography is a good technique as different diameters can be fabricated very easily on the same sample allowing us to achieve excellent control on the experimental parameters. Thus, the design parameters can be experimentally studied and optimized. It is due to this control that we are able to get excellent agreement between the simulated and experimental results. However, e-beam lithography is expensive and thus, cannot be used for solar cell manufacturing. The diameters which provide high absorption are quite large, in the range of 200 nm - 250 nm and can be fabricated with

other large area lithography methods like UV lithography; nano-imprint lithography and even projection lithography. Thus, it is possible to achieve the proposed structures with low-cost fabrication methods.

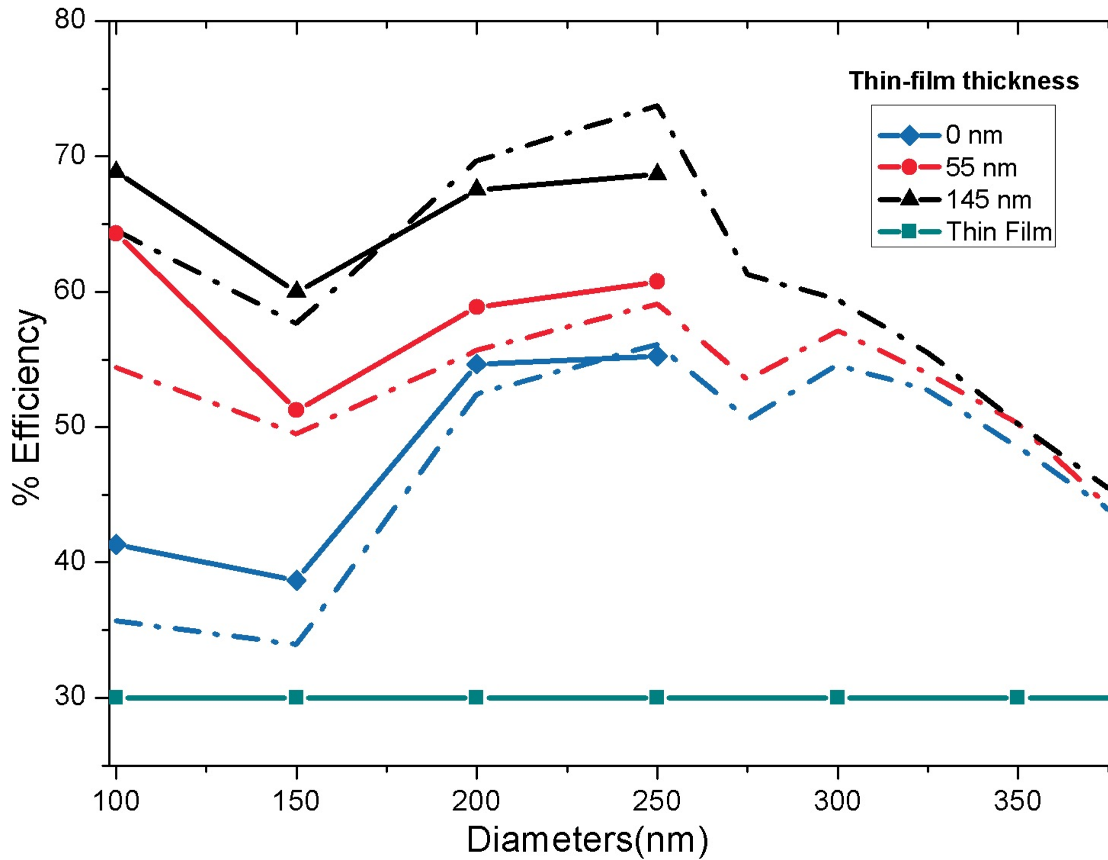


Figure 6.7: Solar weighed absorptance for the platform having nanowire arrays with different diameters and thin film thicknesses (solid lines). The simulated calculations are also plotted (dashed lines).

## 6.3 Conclusion

In this chapter, we proposed two devices based on direct absorption measurements in GaAs and Silicon nanowires. We demonstrated it with GaAs nanowires by etching away the substrate below and a-Si nanowires by fabricating them on a transparent substrate. These measurements are the another step in the direction of workable applications of nanowires. The GaAs nanowires showed the high absorption even after the removal of the substrate. The maximum absorption efficiency achieved for these nanowires is ∼94%. Thus, the GaAs nanowires ensure a promising platform for the photovoltaics and photodetector applications. We also demonstrated the ability to tailor the optical absorption in the a-Si platform by integrating nanowires with thin films. For nanowires on transparent glass configuration, a filter response in transmission was achieved at the resonant wavelength. We were also able to enhance the optical absorption by increasing the residual thin film thickness below the nanowires. The solar weighed absorptance was increased from 30% for starting thin film to ∼70% for 250 nm diameter nanowires integrated with a thin film. This drastic change is attributed to coupled-cavity modes in addition to resonant waveguide modes responsible for the absorption. Importantly, these structures thickness lies in the range of diffusion length of charge carriers in a-Si enabling our structures to harness photogenerated carriers both radially and longitudinally. Lastly, a wide range of transmission and reflection colors were demonstrated with a-Si nanowires. Thus, these platforms lay the foundation for the advanced applications for the futures such as multijunction photodetectors, solar cells, colorful solar cells etc.

# Chapter 7

# Summary and Future Work

## 7.1 Summary

The purpose of this research was to introduce high quality, ordered semiconducting nanowires arrays using IC compatible process and to investigate their optical properties to open up a new realm of highly efficient devices. A clear understanding of the optical behavior of vertical semiconductor nanowires is essential to tailor their properties for desired applications. In this work, a significant progress has been made in understanding the optical properties of vertical semiconductor nanowires for different materials using theoretical and experimental studies. A mathematical treatment was given by using finite difference simulations to investigate the waveguiding properties of nanowires showing the strong dependence of light confinement on the diameter and lattice spacings of the nanowires.

In the theoretical studies, the dependence on refractive index parameters n and k was investigated to understand the interaction of light with the nanowires. It was seen that the hybrid $HE_{1m}$ modes were excited to instigate photon confinement and absorption in the nanowires and the Bloch modes were responsible for the waveguide coupling, and

they were dependent on the real (n) and imaginary (k) part of the refractive index of the material. Further, it was shown that the nanowires needed to be at least 150 nm to guide the light irrespective of their material properties as it was proved for both Silicon and GaAs nanowires. Also, square cross-section nanowires show exact same absorption characteristics across the visible region for the same area as cylindrical nanowires despite the distinct mode shapes in each of them. The study was extended to the experimental section by fabricating high-quality nanowires with materials like GaAs, silicon, a-Si and GaN using reactive ion etching and e-beam lithography. These fabrication techniques showed significant improvement in various parameters like shapes, sidewalls, length control etc. compared to traditional nanowire growth techniques. Several hard masks and etch chemistries were tested to improve the quality of the nanowires.

The optical studies conducted using the simulations were verified by measuring reflections on fabricated nanowires. The nanowires show the expected behavior as predicted in theoretical studies. The excitation of $HE_{1m}$ modes matched well with the sudden reflection dips at the predicted wavelengths. Also, the excitations of F-P modes were also confirmed from the periodic spectral features at the wavelength where the nanowires are low absorbing. The reflection measurements were then used to confirm the presence of Bloch modes in the closely spaced periodic nanowires by comparing them to the disordered nanowires and largely spaced nanowires. The diameter dependent resonance modes and the Bloch mode coupling between the nanowires were also verified by the change in reflected colors of the nanowires. The effect of length, tapering and mask on the nanowires were also measured and verified. Finally, direct absorption measurements were conducted on GaAs by removing the substrate from the bottom. The nanowires showed solar weighed absorption efficiencies as high as 94% even after removing the substrate. Also, a new platform was proposed for the a-Si nanowires showing that the nanowires, when integrated with thin films, show enhancement in solar weighed absorption efficiency by up to ~250%. Fur-

thermore, a wide range of colors in reflection and transmission were observed for different diameters and thin-film thicknesses for this platform.

Based on this work, the potential studies in the immediate future are as follows:

1. Improving the etching profile of the GaN nanowires using other etching chemistries and hard masks.

2. Investigating the optical properties of Silicon, a-Si and GaAs nanowires for various cross sections like the square, triangle, and tapers.

3. Designing the working photodetectors applications based on GaAs and a-Si nanowires.

4. Designing and fabricating the solar cells based on GaAs nanowires and nanowire/thin film platform based on a-Si nanowires by making contacts at top and bottom of the nanowires.

5. Studying the optical properties of GaN nanowires and nanocones.

# References

[1] Shockley, W., Sparks, M. & Teal, G. p-n Junction transistors. *Physical Review* **83**, 151 (1951).

[2] Maiman, T. H. Optical and microwave-optical experiments in ruby. *Physical Review Letters* **4**, 564–566 (1960).

[3] Zheludev, N. The life and times of the LED - a 100-year history. *Nat Photon* **1**, 189–192 (2007).

[4] Decoster, D. & Harari, J. (eds.) *Optoelectronic Sensors* (ISTE and Wiley, 2002), first edn.

[5] Waldrop, M. M. The chips are down for Moore's law. *Nature News* **530**, 144 (2016).

[6] Schaller, R. R. Moore's law: past, present and future. *Spectrum, IEEE* **34**, 52–59 (1997). arXiv:1011.1669v3.

[7] Frolov, S. M., Plissard, S. R., Nadj-perge, S., Kouwenhoven, L. P. & Bakkers, E. P. A. M. Quantum computing based on semiconductor nanowires. *MRS Bulletin* **38**, 809–815 (2013).

[8] Zhang, G. J. & Ning, Y. Silicon nanowire biosensor and its applications in disease diagnostics: A review. *Analytica Chimica Acta* **749**, 1–15 (2012).

[9] Khorasaninejad, M. *et al.* Metalenses at visible wavelengths: Diffraction-limited focusing and subwavelength resolution imaging. *Science* **352**, 1190–1194 (2016).

[10] Khraiche, M. L. *et al.* Ultra-high photosensitivity vertical nanowire arrays for retinal prosthesis (2014).

[11] Liu, H. I., Biegelsen, D. K., Ponce, F. A., Johnson, N. M. & Pease, R. F. W. Self-limiting oxidation for fabricating sub-5 nm silicon nanowires. *Applied Physics Letters* **64**, 1383–1385 (1994).

[12] Street, R. *Technology and Applications of Amorphous Silicon* (Springer-Verlag Berlin Heidelberg GmbH, 2000).

[13] Jie, J., Zhang, W., Bello, I., Lee, C. S. & Lee, S. T. One-dimensional II-VI nanostructures: Synthesis, properties and optoelectronic applications. *Nano Today* **5**, 313–336 (2010).

[14] Joyce, H. J. *et al.* III-V semiconductor nanowires for optoelectronic device applications. *Progress in Quantum Electronics* **35**, 23–75 (2011).

[15] King, R. R. *et al.* 40% efficient metamorphic GaInPGaInAsGe multijunction solar cells. *Applied Physics Letters* **90**, 98–100 (2007).

[16] Najar, A. *et al.* Effective antireflection properties of porous silicon nanowires for photovoltaic applications. *Saudi International Electronics, Communications and Photonics Conference* 1–4 (2013).

[17] Srivastava, S. K. *et al.* Excellent antireflection properties of vertical silicon nanowire arrays. *Solar Energy Materials and Solar Cells* **94**, 1506–1511 (2010).

[18] Tsakalakos, L. Strong broadband optical absorption in silicon nanowire films. *Journal of Nanophotonics* **1**, 013552 (2007).

[19] Khorasaninejad, M., Patchett, S., Sun, J., O, N. & Saini, S. S. Diameter dependence of polarization resolved reflectance from vertical silicon nanowire arrays: Evidence of tunable absorption. *Journal of Applied Physics* **114**, 024304 (2013).

[20] Dhindsa, N. *et al.* Highly ordered vertical GaAs nanowire arrays with dry etching and their optical properties. *Nanotechnology* **25**, 305303 (2014).

[21] Wu, P. M., Anttu, N., Xu, H. Q., Samuelson, L. & Pistol, M.-e. Colorful InAs Nanowire Arrays : From Strong to Weak Absorption. *Nano letters* **12**, 1990–1995 (2012).

[22] Fountaine, K. T., Whitney, W. S. & Atwater, H. a. Resonant absorption in semiconductor nanowires and nanowire arrays: Relating leaky waveguide modes to Bloch photonic crystal modes. *Journal of Applied Physics* **116**, 153106 (2014).

[23] Seo, K. *et al.* Multicolored vertical silicon nanowires. *Nano letters* **11**, 1851–6 (2011).

[24] Snitzer, E. Cylindrical Dielectric Waveguide Modes. *Journal of the Optical Society of America* **51**, 491 (1961).

[25] Hardy, a. & Streifer, W. Coupled mode theory of parallel waveguides. *Journal of Lightwave Technology* **3** (1985).

[26] Khorasaninejad, M., Abedzadeh, N., Walia, J., Patchett, S. & Saini, S. S. Color matrix refractive index sensors using coupled vertical silicon nanowire arrays. *Nano letters* **12**, 4228–34 (2012).

[27] Bernhard, C. G. Structural and functional adaptation in a visual system. *Endeavour* **26**, 79–84 (1967).

[28] CLAPHAM, P. B. & HUTLEY, M. C. Reduction of Lens Reflexion by the [ldquo]Moth Eye[rdquo] Principle. *Nature* **244**, 281–282 (1973).

[29] Gittleman, J. I., Sichel, E. K., Lehmann, H. W. & Widmer, R. Textured silicon: A selective absorber for solar thermal conversion. *Applied Physics Letters* **35**, 742–744 (1979).

[30] Craighead, H. G., Howard, R. E. & Tennant, D. M. Textured thin-film Si solar selective absorbers using reactive ion etching. *Applied Physics Letters* **37**, 653–655 (1980).

[31] Sivakov, V. *et al.* Silicon nanowire-based solar cells on glass: Synthesis, optical properties, and cell parameters. *Nano Letters* **9**, 1549–1554 (2009).

[32] Convertino, A., Cuscunà, M. & Martelli, F. Optical reflectivity from highly disordered Si nanowire films. *Nanotechnology* **21**, 355701 (2010).

[33] Diedenhofen, S. L. *et al.* Broad-band and Omnidirectional Antireflection Coatings Based on Semiconductor Nanorods. *Advanced Materials* **21**, 973–978 (2009).

[34] Zhu, J. *et al.* Optical absorption enhancement in amorphous silicon nanowire and nanocone arrays. *Nano letters* **9**, 279–82 (2009).

[35] Garnett, E. & Yang, P. Light trapping in silicon nanowire solar cells. *Nano letters* **10**, 1082–7 (2010).

[36] Zhang, A. *et al.* Silicon nanowire detectors showing phototransistive gain. *Applied Physics Letters* **93**, 121110 (2008).

[37] Cao, L., Park, J.-S., Fan, P., Clemens, B. & Brongersma, M. L. Resonant germanium nanoantenna photodetectors. *Nano Letters* **10**, 1229–1233 (2010).

[38] Haraguchi, K., Katsuyama, T., Hiruma, K. & Ogawa, K. GaAs p-n junction formed in quantum wire crystals. *Applied Physics Letters* **60**, 745–747 (1992).

[39] Kayes, B. M., Atwater, H. a. & Lewis, N. S. Comparison of the device physics principles of planar and radial p-n junction nanorod solar cells. *Journal of Applied Physics* **97**, 114302 (2005).

[40] Tsakalakos, L. *et al.* Silicon nanowire solar cells. *Applied Physics Letters* **91**, 233117 (2007).

[41] Garnett, E. C. & Yang, P. Silicon Nanowire Radial p - n Junction Solar Cells. *American Chemical Society* **130**, 9224–9225 (2008).

[42] Tian, B. *et al.* Coaxial silicon nanowires as solar cells and nanoelectronic power sources. *Nature* **449**, 885–9 (2007).

[43] Li, J. *et al.* Si nanopillar array optimization on Si thin films for solar energy harvesting. *Applied Physics Letters* **95**, 95–98 (2009).

[44] Law, M., Greene, L. E., Johnson, J. C., Saykally, R. & Yang, P. Nanowire dye-sensitized solar cells. *Nature materials* **4**, 455–459 (2005).

[45] Goto, H. *et al.* Growth of core-shell inP nanowires for photovoltaic application by selective-area metal organic vapor phase epitaxy. *Applied Physics Express* **2**, 3–6 (2009).

[46] Mehta, B. R. & Kruis, F. E. A graded diameter and oriented nanorod-thin film structure for solar cell application: A device proposal. *Solar Energy Materials and Solar Cells* **85**, 107–113 (2005).

[47] LaPierre, R. R. Numerical model of current-voltage characteristics and efficiency of GaAs nanowire solar cells. *Journal of Applied Physics* **109**, 034311 (2011).

[48] Hu, Y., LaPierre, R. R., Li, M., Chen, K. & He, J.-J. Optical characteristics of GaAs nanowire solar cells. *Journal of Applied Physics* **112**, 104311 (2012).

[49] Gutsche, C. *et al.* n-GaAs/InGaP/p-GaAs Core-Multishell Nanowire Diodes for Efficient Light-to-Current Conversion. *Advanced Functional Materials* **22**, 929–936 (2012).

[50] Yao, M. *et al.* GaAs nanowire array solar cells with axial p-i-n junctions. *Nano letters* **14**, 3293–303 (2014).

[51] Wallentin, J. *et al.* InP nanowire array solar cells achieving 13.8% efficiency by exceeding the ray optics limit. *Science (New York, N.Y.)* **339**, 1057–60 (2013).

[52] Tang, Y. B. *et al.* Vertically aligned p-type single-crystalline GaN nanorod arrays on n-type Si for heterojunction photovoltaic cells. *Nano letters* **8**, 4191–5 (2008).

[53] Cho, E.-H. *et al.* Two-dimensional photonic crystal color filter development. *Optics express* **17**, 8621–8629 (2009).

[54] Park, H. *et al.* Filter-Free Image Sensor Pixels Comprising Silicon Nanowires with Selective Color Absorption. *Nano Lett* **14**, 1804–1809 (2014).

[55] Park, H. & Crozier, K. B. Vertically stacked photodetector devices containing silicon nanowires with engineered absorption spectra. *ACS Photonics* **2**, 544–549 (2015).

[56] Dai, X. *et al.* GaAs/AlGaAs nanowire photodetector. *Nano Letters* **14**, 2688–2693 (2014).

[57] Kind, H., Yan, H., Messer, B., Law, M. & Yang, P. Nanowire ultraviolet photodetectors and optical switches. *Advanced Materials* **14**, 158–160 (2002).

[58] Saxena, D. *et al.* Optically pumped room-temperature GaAs nanowire lasers. *Nature Photonics* **7**, 963–968 (2013).

[59] Hua, B., Motohisa, J., Kobayashi, Y., Hara, S. & Fukui, T. Single GaAs / GaAsP Coaxial Core - Shell Nanowire Lasers 2009. *Nano letters* **9**, 112–116 (2009).

[60] Gradeeak, S., Qian, F., Li, Y., Park, H.-G. & Lieber, C. M. GaN nanowire lasers with low lasing thresholds. *Applied Physics Letters* **87**, 173111 (2005).

[61] Wright, J. B. *et al.* Multi-colour nanowire photonic crystal laser pixels. *Scientific reports* **3**, 2982 (2013).

[62] Greytak, A. B., Barrelet, C. J., Li, Y. & Lieber, C. M. Semiconductor nanowire laser and nanowire waveguide electro-optic modulators. *Applied Physics Letters* **87**, 1–3 (2005).

[63] Johnson, J. C. *et al.* Single nanowire lasers. *Journal of Physical Chemistry B* **105**, 11387–11390 (2001).

[64] Duan, X., Huang, Y., Agarwal, R. & Lieber, C. M. Single-nanowire electrically driven lasers. *Nature* **421**, 241–245 (2003).

[65] Patolsky, F. *et al.* Electrical detection of single viruses. *Proceedings of the National Academy of Sciences of the United States of America* **101**, 14017–22 (2004).

[66] Kotov, N. a. *et al.* Nanomaterials for Neural Interfaces. *Advanced Materials* **21**, 3970–4004 (2009).

[67] Gao, Z. Q. *et al.* Silicon nanowire arrays for label-free detection of DNA. *Analytical Chemistry* **79**, 3291–3297 (2007).

[68] Zheng, G., Patolsky, F., Cui, Y., Wang, W. U. & Lieber, C. M. Multiplexed electrical detection of cancer markers with nanowire sensor arrays. *Nature Biotechnology* **23**, 1294–1301 (2005).

[69] Walia, J., Dhindsa, N., Khorasaninejad, M. & Saini, S. S. Color Generation and Refractive Index Sensing Using Diffraction from 2D Silicon Nanowire Arrays. *Small (Weinheim an der Bergstrasse, Germany)* **10**, 144–151 (2014).

[70] Khorasaninejad, M. *et al.* Bunching characteristics of silicon nanowire arrays. *Journal of Applied Physics* **111**, 044328 (2012).

[71] Snyder, A. & Love, J. Optical Waveguide Theory (1983).

[72] Sturmberg, B. C. P. *et al.* Modal analysis of enhanced absorption in silicon nanowire arrays. *Optics express* **19**, A1067–A1081 (2011).

[73] Aspnes, D. E. & Studna, A. A. Dielectric functions and optical parameters of Si, Ge, GaP, GaAs, GaSb, InP, InAs, and InSb from 1.5 to 6.0 eV. *Physical Review B* **27**, 985–1009 (1983).

[74] Muskens, O. L., Rivas, J. G., Algra, R. E., Bakkers, E. P. A. M. & Lagendijk, A. Design of Light Scattering in Nanowire Materials for Photovoltaic Applications. *Nano Lett* **8**, 2638–2642 (2008).

[75] Khorasaninejad, M., Walia, J. & Saini, S. S. Enhanced first-order Raman scattering from arrays of vertical silicon nanowires. *Nanotechnology* **23**, 275706 (2012).

[76] Wu, Y. *et al.* Broadband absorption enhancement in elliptical silicon nanowire arrays for photovoltaic applications. *Optics express* **22 Suppl 5**, A1292–302 (2014).

[77] Park, H. & Crozier, K. B. Elliptical silicon nanowire photodetectors for polarization-resolved imaging. *Opt. Express* **23**, 7209–7216 (2015).

[78] Schonbrun, E., Seo, K. & Crozier, K. B. Reconfigurable Imaging Systems Using Elliptical Nanowires.(supp). *Nano Lett* **11**, 4299–4303 (2011).

[79] Wagner, R. S. & Ellis, W. C. Vapor-liquid-solid mechanism of single crystal growth. *Applied Physics Letters* **4**, 89–90 (1964).

[80] Givargizov, E. Fundamental aspects of VLS growth. *Journal of Crystal Growth* **31**, 20–30 (1975).

[81] Schmidt, V., Wittemann, J. V., Senz, S. & Gösele, U. Silicon Nanowires: A Review on Aspects of their Growth and their Electrical Properties. *Advanced Materials* **21**, 2681–2702 (2009).

[82] Lensch-Falk, J. L., Hemesath, E. R., Perea, D. E. & Lauhon, L. J. Alternative catalysts for VSS growth of silicon and germanium nanowires. *Journal of Materials Chemistry* **19**, 849 (2009).

[83] Schmidt, V., Wittemann, J. V. & Gösele, U. Growth, thermodynamics, and electrical properties of silicon nanowires. *Chemical Reviews* **110**, 361–388 (2010).

[84] Choi, H.-j. *VLS Growth of Semiconductor Nanowires*. NanoScience and Technology (Springer Berlin Heidelberg, Berlin, Heidelberg, 2012).

[85] Tchernycheva, M., Harmand, J. C., Patriarche, G., Travers, L. & Cirlin, G. E. Temperature conditions for GaAs nanowire formation by Au-assisted molecular beam epitaxy. *Nanotechnology* **17**, 4025–30 (2006).

[86] Wu, Z. H., Mei, X. Y., Kim, D., Blumin, M. & Ruda, H. E. Growth of Au-catalyzed ordered GaAs nanowire arrays by molecular-beam epitaxy. *Applied Physics Letters* **81**, 5177 (2002).

[87] Czaban, J. A., Thompson, D. A. & Lapierre, R. R. GaAs Core - Shell Nanowires for Photovoltaic Applications 2009. *Nano letters* **9**, 148–154 (2009).

[88] Plante, M. & LaPierre, R. Au-assisted growth of GaAs nanowires by gas source molecular beam epitaxy: Tapering, sidewall faceting and crystal structure. *Journal of Crystal Growth* **310**, 356–363 (2008).

[89] Ohlsson, B. J. *et al.* Size-, shape-, and position-controlled GaAs nano-whiskers. *Applied Physics Letters* **79**, 3335 (2001).

[90] Wong, Y. Y., Yahaya, M. M., Salleh, M. & Majlis, B. Y. Controlled growth of silicon nanowires synthesized via solid-liquid-solid mechanism. In *Science and Technology of Advanced Materials*, vol. 6, 330–334 (2005).

[91] Heitsch, A. T., Fanfair, D. D., Tuan, H.-Y. & Korgel, B. a. Solution-liquid-solid (SLS) growth of silicon nanowires. *Journal of the American Chemical Society* **130**, 5436–7 (2008).

[92] Morales, A. M. & Lieber, C. M. A Laser Ablation Method for the Synthesis of Crystalline Semiconductor Nanowires. *Science* **279**, 208–211 (1998).

[93] Ikejiri, K., Ishizaka, F., Tomioka, K. & Fukui, T. GaAs nanowire growth on polycrystalline silicon thin films using selective-area MOVPE. *Nanotechnology* **24**, 115304 (2013).

[94] Persson, A., Ohlsson, B., Jeppesen, S. & Samuelson, L. Growth mechanisms for GaAs nanowires grown in CBE. *Journal of Crystal Growth* **272**, 167–174 (2004).

[95] Chen, C. C. *et al.* Catalytic growth and characterization of gallium nitride nanowires. *Journal of the American Chemical Society* **123**, 2791–2798 (2001).

[96] Duan, X. & Lieber, C. M. Laser-assisted catalytic growth of single crystal GaN nanowires. *Journal of the American Chemical Society* **122**, 188–189 (2000).

[97] Han, W. Q., Fan, S. S., Li, Q. Q. & Hu, Y. D. Synthesis of gallium nitride nanorods through a carbon nanotube-confined reaction. *Science* **277**, 1287–1289 (1997).

[98] Peng, K. *et al.* Fabrication of Single-Crystalline Silicon Nanowires by Scratching a Silicon Surface with Catalytic Metal Particles. *Advanced Functional Materials* **16**, 387–394 (2006).

[99] Fang, H., Wu, Y., Zhao, J. & Zhu, J. Silver catalysis in the fabrication of silicon nanowire arrays. *Nanotechnology* **17**, 3768–3774 (2006).

[100] Constantine, C. Etching of GaAs/AlGaAs rib waveguide structures using BCl3/Cl2/N2/Ar electron cyclotron resonance. *Journal of Vacuum Science & Technology B: Microelectronics and Nanometer Structures* **13**, 2025 (1995).

[101] Huang, Z., Fang, H. & Zhu, J. Fabrication of Silicon Nanowire Arrays with Controlled Diameter, Length, and Density. *Advanced Materials* **19**, 744–748 (2007).

[102] Chen, K., He, J.-J., Li, M.-Y. & Lapierre, R. Fabrication of GaAs Nanowires by Colloidal Lithography and Dry Etching. *Chinese Physics Letters* **29**, 036105 (2012).

[103] Qiu, W. & Wang, J. Highly controllable ICP etching of GaAs based materials for grating fabrication. *Journal of Semiconductors* **33**, 026001 (2012).

[104] Mårtensson, T. *et al.* Nanowire Arrays Defined by Nanoimprint Lithography. *Nano Letters* **4**, 699–702 (2004).

[105] Henry, M. D., Walavalkar, S., Homyk, a. & Scherer, a. Alumina etch masks for fabrication of high-aspect-ratio silicon micropillars and nanopillars. *Nanotechnology* **20**, 255305 (2009).

[106] Pevzner, A. *et al.* Knocking down highly-ordered large-scale nanowire arrays. *Nano letters* **10**, 1202–8 (2010).

[107] Henry, M. D. *ICP etching of silicon for micro and nanoscale devices*. Phd thesis, California Institute of Technology (2010).

[108] Bimberg, D. *et al.* InGaAs-GaAs Quantum-Dot Lasers. *IEEE Journal of Selected Topics in Quantum Electronics* **3**, 196–205 (1997).

[109] Thompson, G. Gallium arsenide lasers (1973). URL https://www.google.com/patents/US3780358.

[110] Thompson, G. H. B. Gallium arsenide injection lasers (1975). URL https://www.google.com/patents/US3911376.

[111] Volatier, M., Duchesne, D., Morandotti, R., Arès, R. & Aimez, V. Extremely high aspect ratio GaAs and GaAs/AlGaAs nanowaveguides fabricated using chlorine ICP etching with N2-promoted passivation. *Nanotechnology* **21**, 134014 (2010).

[112] Jalabert, L. *et al.* High aspect ratio GaAs nanowires made by ICP-RIE etching using Cl2/N2 chemistry. *Microelectronic Engineering* **85**, 1173–1178 (2008).

[113] Combri, S. *et al.* Optimization of an inductively coupled plasma etching process of GaInP\GaAs based material for photonic band gap applications. *Journal of Vacuum Science & Technology B: Microelectronics and Nanometer Structures* **23**, 1521 (2005).

[114] Braive, R. *et al.* Inductively coupled plasma etching of GaAs suspended photonic crystal cavities. *Journal of Vacuum Science & Technology B: Microelectronics and Nanometer Structures* **27**, 1909 (2009).

[115] Shul, R. J. High-density plasma etching of compound semiconductors. *Journal of Vacuum Science & Technology A: Vacuum, Surfaces, and Films* **15**, 633 (1997).

[116] Wang, B., Stevens, E. & Leu, P. W. Strong broadband absorption in GaAs nanocone and nanowire arrays for solar cells. *Optics Express* **22**, A386 (2014).

[117] Hwang, S., Shim, J. & Yoo, K. Effect of Waveguide Structure for Suppression of Ripples in the Far-Field Pattern of a 405-nm InGaN-GaN Laser Diode. *Journal of the Korean Physical Society* **51**, 488 (2007).

[118] Wang, Y. D. *et al.* High optical quality GaN nanopillar arrays. *Applied Physics Letters* **86**, 071917 (2005).

[119] Reddy, N. P., Naureen, S. & Mokkapati, S. Enhanced luminescence from GaN nanopillar arrays fabricated using a top-down process. *Nanotechnology* **27**, 65304 (2015).

[120] Chon, J. W. M., Gan, X. & Gu, M. Splitting of the focal spot of a high numerical-aperture objective in free space. *Applied Physics Letters* **81**, 1576–1578 (2002).

[121] Park, H., Seo, K. & Crozier, K. B. Adding colors to polydimethylsiloxane by embedding vertical silicon nanowires. *Applied Physics Letters* **101**, 193107 (2012).

[122] Park, H. & Crozier, K. B. Multispectral imaging with vertical silicon nanowires. *Scientific reports* **3**, 2460 (2013).

[123] Anttu, N. & Xu, H. Q. Efficient light management in vertical nanowire arrays for photovoltaics. *Optics express* **21**, 27589–27605 (2013).

[124] Dhindsa, N. & Saini, S. S. Localized absorption in aluminum mask in visible spectrum due to longitudinal modes in vertical silicon nanowire arrays. *Journal of Applied Physics* **117**, 224302 (2015).

[125] Dhindsa, N. *et al.* Adjustable optical response of amorphous silicon nanowires integrated with thin films. *Nanotechnology* **27**, 145703 (2016).

[126] Anttu, N. *et al.* Reflection measurements to reveal the absorption in nanowire arrays. *Optics letters* **38**, 1449–51 (2013).

[127] Fountaine, K. T., Kendall, C. G. & Atwater, H. a. Near-unity broadband absorption designs for semiconducting nanowire arrays via localized radial mode excitation. *Optics express* **22**, A930–A940 (2014).

[128] Lin, C. & Povinelli, M. L. The effect of plasmonic particles on solar absorption in vertically aligned silicon nanowire arrays. *Applied Physics Letters* **97**, 071110 (2010).

[129] Kelzenberg, M. *et al.* Enhanced absorption and carrier collection in Si wire arrays for photovoltaic applications. *Nature Materials* **9**, 1–13 (2009).

[130] Mokkapati, S. & Catchpole, K. R. Nanophotonic light trapping in solar cells. *Journal of Applied Physics* **112**, 101101 (2012).

[131] Tanaka, Y., Kawamoto, Y., Fujita, M. & Noda, S. Enhancement of broadband optical absorption in photovoltaic devices by band-edge effect of photonic crystals. *Optics express* **21**, 447–450 (2013).

[132] Green, M. A. Thin-film solar cells: review of materials, technologies and commercial status. *Journal of Materials Science: Materials in Electronics* **18**, 15–19 (2007).

[133] Hu, L. & Chen, G. Analysis of optical absorption in silicon nanowire arrays for photovoltaic applications. *Nano letters* **7**, 3249–52 (2007).

[134] Anttu, N. & Xu, H. Q. Coupling of light into nanowire arrays and subsequent absorption. *Journal of nanoscience and nanotechnology* **10**, 7183–7187 (2010).

[135] Dorn, R., Quabis, S. & Leuchs, G. The focus of light - linear polarization breaks the rotational symmetry of the focal spot. *arXiv* **0340**, 1–12 (2003).

[136] Walia, J. *et al.* Enhanced Photothermal Conversion in Vertically Oriented Gallium Arsenide Nanowire Arrays. *Nano Letters* **14**, 5820–5826 (2014).

# Appendices

# Appendix A

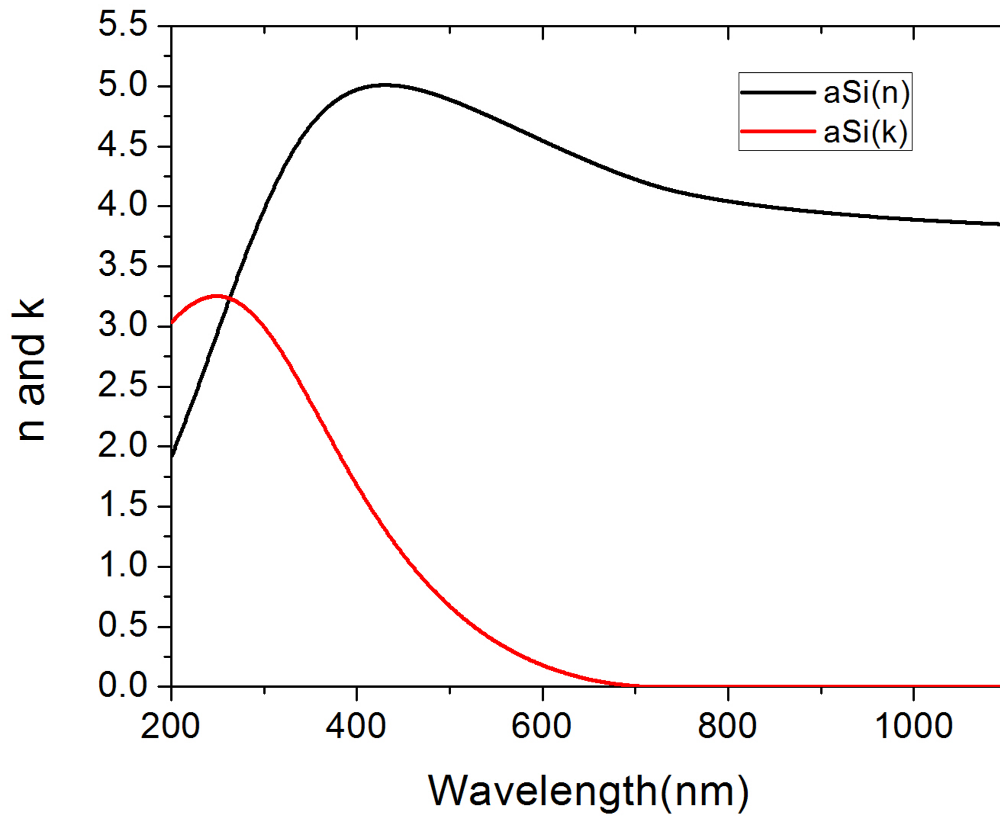


Figure A.1: Extracted n and k of a-Si from a thin film of known thickness.